Università degli studi di Pavia
Dottorato di ricerca in Fisica – Ciclo XXXIV

Bloch surface waves for integrated optics: a complete architecture

Tommaso Perani

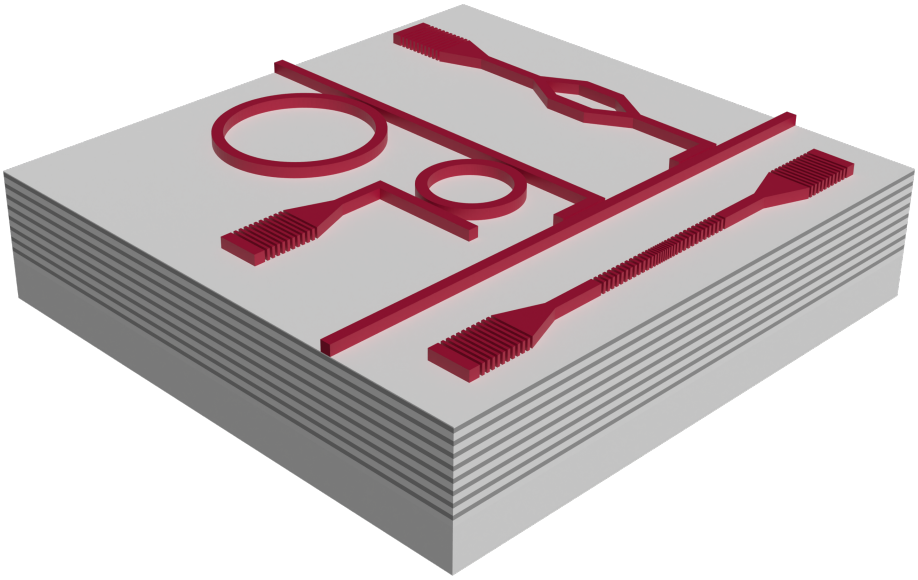

Tesi per il conseguimento del titolo

Bloch surface waves for integrated optics: a complete architecture

Tommaso Perani

A dissertation submitted to the Graduate School in Physics
in partial fulfillment of the requirements for the degree of

Doctor of Philosophy in Physics

Supervised by Prof. Marco Liscidini

University of Pavia
Department of Physics

Tommaso Perani
Bloch surface waves for integrated optics: a complete architecture

Pavia, Italy (2022)

Hunc igitur terrorem animi tenebrasque necessest
non radii solis neque lucida tela diei
discutiant, sed naturae species ratioque.

(Titus Lucretius Carus, *De rerum natura*)

Abstract

Over the past few decades, the generation, manipulation, and detection of light at the nanoscale, including all the aspects concerning the physical foundations and the deriving technologies, have undergone substantial development. The relevance of photonics today is such that the knowledge of its basics and applications is essential in numerous fields of physics and engineering. One of the most challenging efforts of photonics is the design and fabrication of photonic integrated circuits, in which different optical components are combined on a single chip to form a multifunctional device. As the miniaturization of semiconductor devices has made it possible to achieve unpredictable advances in electronics, so the shift from bulk to integrated photonics paves the way to the development of flexible, accessible, and scalable light-based devices, for a number of applications ranging from optoelectronics to biochemical sensing to quantum information processing.

To date, silicon-based structures have attracted special attention as a preferred platform for integrated optics, owing to their high performance in the near-infrared spectrum and well-established foundry technology. Though other material platforms have been developed (III-V semiconductors, lithium niobate, silicon nitride, high-refractive-index glasses, polymers, etc.), a promising alternative to gain on-chip light control is the use of surface electromagnetic waves (SEWs) propagating along the interface between two different media. In particular, the ability of achieving strong optical confinement at the structure surface allows one to enhance various linear, and especially nonlinear, optical processes.

The most popular SEWs are certainly surface plasmon polaritons (SPPs), which originate from the collective oscillations of conduction electrons coupled with photons propagating at a metal/dielectric interface. These waves are transverse magnetic (TM) in nature and show a well-defined dispersion relation limited by the material permittivities. The electromagnetic field intensity is highest at the interface and decays exponentially into the adjacent materials, thus providing sub-wavelength confinement in the proximity of the interface. Due to this extreme localization of the electromagnetic field, SPPs have long been promoted as candidates for integrated optics, and their current applications include waveguides, modulators, nanolasers, and other circuit elements. Yet, their behavior at optical frequencies is largely dominated

by the absorption loss inherent in all metals, which results in propagation lengths typically on the order of microns or tens of microns.

To overcome this limitation, multilayer dielectric stacks have emerged as one potential solution. Periodic multilayers are known to exhibit forbidden frequency windows, named photonic bandgaps (PBGs), for which light propagation is inhibited. Therefore, they act as perfect mirrors with unity reflectivity within the PBG. By breaking the multilayer periodicity with a truncation layer of proper thickness, one may introduce defect modes inside the PBG known as Bloch surface waves (BSWs). These modes propagate at the interface between the truncated periodic multilayer and the external homogeneous dielectric. Their dispersion relation is located within the multilayer PBG and below the lightline of the external medium. As a consequence, the field envelope inside the multilayer and the field amplitude in the external medium decay exponentially, which origins a surface wave.

BSWs have been known since the late 1970s. However, a renewed interest has been driven by the development of fabrication techniques that allows one to obtain periodic multilayers with tens of periods quite inexpensively. Although more complicated than plasmonic systems, BSW-based devices do not suffer from the absorption loss that affects metallic structures. In addition, as compared to SPPs, the dispersion relation of BSWs does not depend only on the choice of the constituent materials, but it can be tuned at almost any frequency by properly tailoring the multilayer geometry. This makes BSWs particularly attractive for applications in the visible spectrum. Finally, both transverse electric (TE) and transverse magnetic (TM) BSWs can be excited.

To date, many circuit elements operating with BSWs have been studied, these including waveguides, resonators, gratings, lenses, and interferometers. However, the development of BSW-based integrated optics has been hampered by relatively high propagation loss (of the order of dB/mm or higher) that cannot be explained in terms of surface scattering or material absorption. Second, 3D confinement has been realized mainly in large-mode-volume ring resonators or other whispering-gallery-mode systems. Less attention has been paid to other solutions, e.g., based on photonic crystals (PhCs), which are known to support resonant modes characterized by small mode volumes, even smaller than a cubic wavelength of light. Finally, even less research has been conducted on BSW excitation methods compatible with the concept of integrated optics.

This dissertation rests on these unanswered questions to present novel concepts for on-chip integration of a multilayer platform supporting BSWs at visible wavelengths. In Chapter 1, after providing a general introduction to the optical confinement strategies in dielectric structures, we present the essential building blocks of an integrated optical platform. In Chapter 2, we focus on the nature of guided BSWs in PhC ridges and their strategic advantage in integrated optics. Namely, we track down the origin

of the disappointing performance of PhC ridge waveguides in terms of propagation loss, and suggest a general design principle that allows us to obtain intrinsic loss as low as 5 dB/km for a polymeric PhC ridge operating in the visible spectrum. In Chapter 3, we demonstrate a PhC nanobeam cavity realized on the same platform, thus combining the small mode volumes and footprint size of a PhC cavity with the surface field enhancement typical of BSWs. In Chapter 4, we tackle the difficult task of exciting BSWs, with major detail to diffraction grating schemes and their optimization. Finally, in Chapter 5, we draw our conclusion and present some future perspectives, in particular on inverse design strategies and potential application for integrated nonlinear optics based on polymers. Appendix A contains an in-depth treatment of some specific topics.

Contents

List of Figures

List of Tables

CHAPTER 1

Building blocks of integrated optics

1.1. Light confinement in dielectric structures

The possibility of manipulating light is of great importance in all areas of research concerning the light-matter interaction, from fundamental physics to engineering applications. In dielectric structures, the control of light propagation can be obtained by exploiting the phenomenon of *total internal reflection* (TIR) at the interface between two media with different refractive indices. If light is incident from an optically dense medium (refractive index n_2) to an optically rare medium (refractive index $n_1 < n_2$) at an angle equal or greater than the critical angle $\vartheta_c = \arcsin(n_1/n_2)$, the incident wave is totally reflected, in the sense that all the energy in the incident wave goes into the reflected wave. The transmitted wave propagates only parallel to the interface with the field amplitude decaying exponentially in the direction normal to the interface (evanescent wave). The reader is referred to Appendix A for a general review of some basic properties of the electromagnetic radiation, or to any standard electromagnetism textbook for a more detailed account [1].

TIR is the basis for efficiently guiding light. The most simple configuration one can study is the *symmetric slab waveguide* shown in Fig. 1.1. It consists of a thin slab of a high-refractive-index dielectric medium (the *core*, with index n_2) sandwiched between two semi-infinite low-refractive-index layers (the *cladding*, with index $n_1 < n_2$). When the angle of incidence $\vartheta < \vartheta_c = \arcsin(n_1/n_2)$, no total reflection occurs at the interfaces, with the electromagnetic energy free to flow out of the core into the

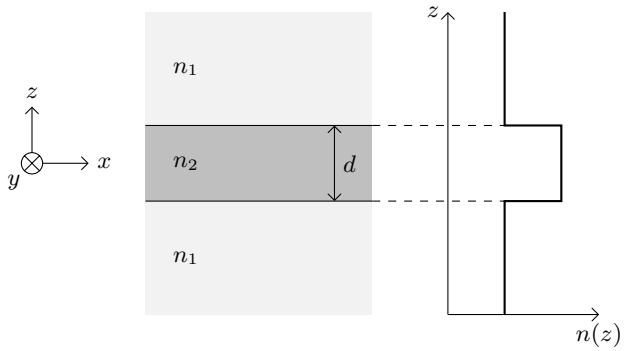

FIGURE 1.1. Schematic of a symmetric slab waveguide.

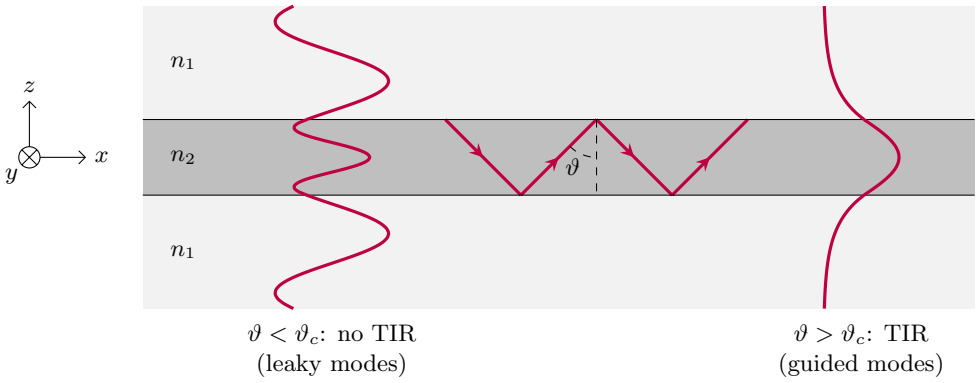

FIGURE 1.2. Schematic illustration of the mechanism of TIR in a slab waveguide, resulting in leaky modes when $\vartheta < \vartheta_c$ (left side) and guided modes when $\vartheta > \vartheta_c$ (right side).

cladding. This results in a continuum of *leaky modes* that transversely oscillate to infinity on both sides of the waveguide. When $\vartheta \geq \vartheta_c$, instead, the wave inside the core is totally reflected at both interfaces. If ϑ is such that the wave interferes constructively, the wave can sustain itself as it propagates along the waveguide. This leads to a discrete set of *guided modes*, corresponding to the angles of incidence that fulfill the constructive interference condition (Fig. 1.2). The number of allowed guided modes depends on the light wavelength and polarization, the material refractive indices, and the core thickness. A rigorous treatment that considers also the more general case of an asymmetric slab waveguide is given in Appendix A.4.

Slab waveguides confine light in only one transverse direction, and therefore have little utilization in integrated optics, for most practical applications take advantage of the optical confinement attainable in 2D waveguides. These latter are the optical analog of electrical wires, in that they enable connectivity between all components of a photonic device. Light can be confined in both transverse directions, e.g., by exploiting TIR also laterally, in a number of different solutions (Fig. 1.3) [2]. The paradigmatic example is the *ridge waveguide*. It is formed by loading a low-refractive-index substrate with a rectangular strip of a high-refractive-index material that serves as waveguiding core. A ridge waveguide provides strong lateral confinement, provided the ridge material has high enough refractive index as compared to the external medium. The modes supported by a ridge waveguide cannot be calculated analytically; though, one can exploit numerical approaches such as finite-element or finite-difference methods (see Appendix A.9). An alternative approach is to use the effective index method (EIM) to find an approximate solution by separating the 2D problem in two 1D problems along each transverse direction (see Appendix A.6).

One can also use TIR to achieve full 3D light confinement, e.g., by bending a waveguide in a closed loop to form a *microring resonator*. When an integer number of effective wavelengths fits in one roundtrip length, constructive interference occurs. On

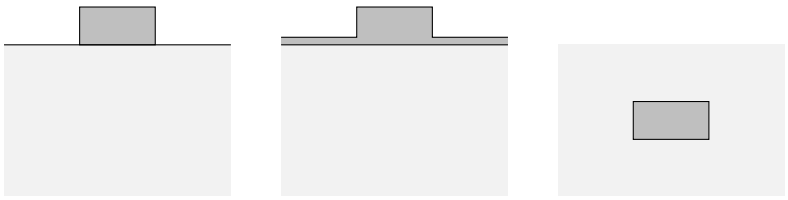

FIGURE 1.3. Schematics of some common 2D channel waveguides. A darker color represents a higher refractive index.

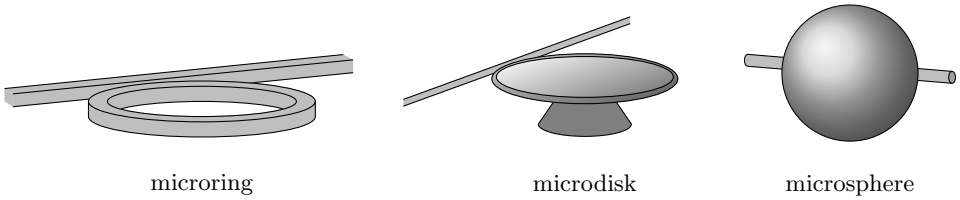

FIGURE 1.4. Whispering gallery mode resonators.

resonance, the resulting traveling wave builds up in intensity and it is sustained inside the structure for many optical cycles. The ability of a resonator to store energy over significant time makes it indispensable in all applications that require strong light-matter interaction. Similarly, in microdisks, microtoroids, and microspheres, light can circulate close to the structure boundaries in what are referred to as *whispering gallery modes* (Fig. 1.4) [3]. These modes develop because of TIR and therefore exist as long as the refractive index contrast between the microstructure and the ambient medium is sufficiently high.

Besides TIR, light propagation can be controlled by exploiting *interference* in media with periodically modulated refractive index, e.g., *distributed Bragg reflectors* (DBRs). DBRs are stacks of dielectric layers with different refractive indices alternating in space with period Λ, as sketched in Fig. 1.5(a). As an electromagnetic wave propagates in the structure, it experiences multiple reflection from the periodically arranged interfaces. For certain frequencies, the optical path difference between two consecutive reflected waves, plus the phase shift acquired at each interface, causes them to interfere constructively (Bragg's condition). Thus, the partial reflected waves add perfectly in phase and build up into a strong reflected wave that inhibits the propagation of the incident one within these frequency intervals (*stopband*). In the stopband, the reflectivity of the structure ideally reaches unity for an infinite number of periods (Fig. 1.5(b)) [4]. DBRs are widely used in modern optoelectronics as mirrors or spectral filters, also owing to the development of thin-film deposition techniques, which makes it possible to grow dielectric stacks with tens

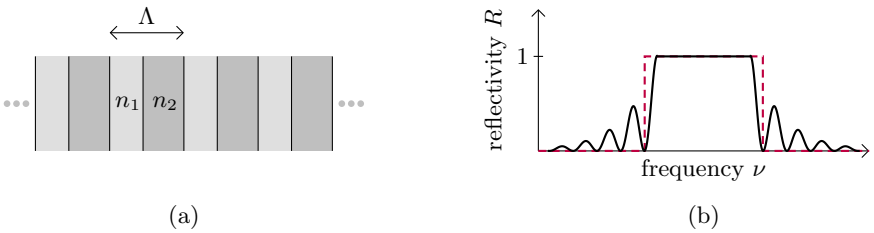

FIGURE 1.5. (a) Schematic of a DBR consisting of two materials with different refractive indices ($n_1 < n_2$) alternating with period Λ. (b) Reflectivity spectra for an infinite-size (dashed) and a finite-size (solid) DBR.

of layers quite inexpensively. Remarkably, though, the observation of the reflection stopband in periodically layered media dates back to Lord Rayleigh in 1887 [5].

DBRs with an infinite number of periods are the 1D example of a more general class of structured materials known as *photonic crystals* (PhC). PhCs are media with a periodic modulation of the dielectric function in one, two or three dimensions. In close formal analogy with electrons in natural crystals, electromagnetic waves propagating in PhCs experience a periodic potential due to the periodic spatial variation of the refractive index, just as electrons in crystals experience a periodic Coulomb potential due to the periodic arrangement of ions in the crystal lattice. It gives rise to allowed *photonic energy bands* and forbidden *photonic bandgaps* (PBGs) for the electromagnetic states, just as energy bands separated by bandgaps develop in electronic crystals. This is illustrated in Fig. 1.6 for the simple case of a 1D PhC. Hence,

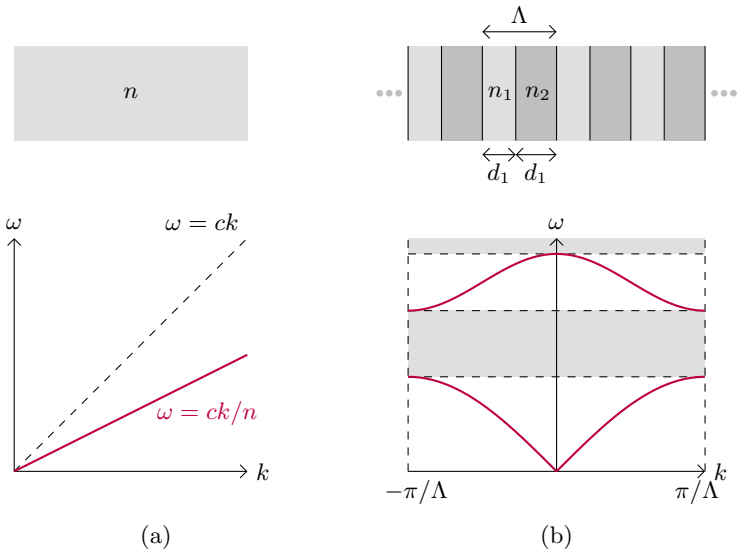

FIGURE 1.6. Dispersion relations $\omega(k)$ for electromagnetic waves (a) in a homogeneous medium of refractive index n and (b) in a 1D PhC consisting of two materials with different refractive indices ($n_1 < n_2$) alternating with period Λ. The periodicity of the photonic lattice folds the dispersion curves in the first Brillouin zone $(-\pi/\Lambda, \pi/\Lambda)$. The shaded areas correspond to the forbidden PBGs.

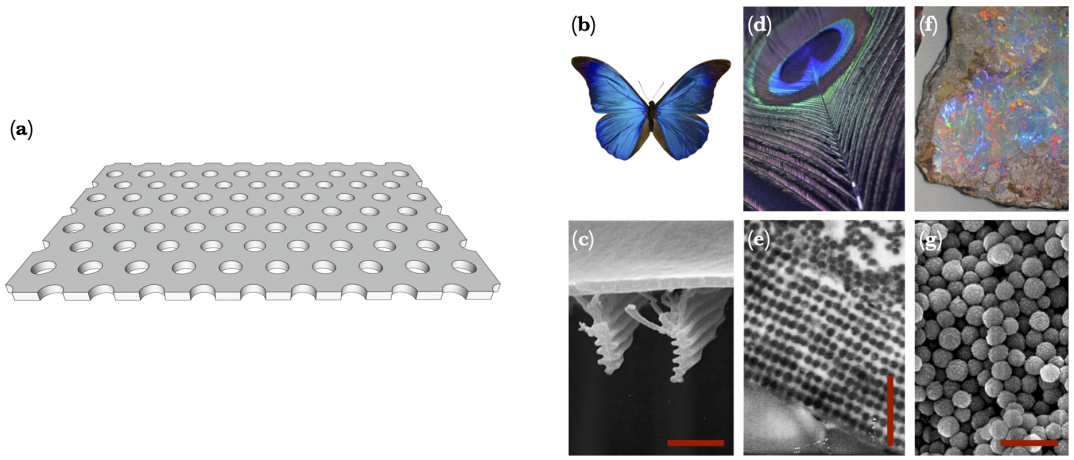

FIGURE 1.7. (a) Schematic of a 2D PhC slab consisting of a suspended dielectric membrane patterned with hexagonal lattice of air holes. Naturally occurring PhCs: (b) blue-iridescent Morpho butterfly and (c) SEM image of the 1D wing structure (reprinted from [9]); (d) multicolored peacock feather and (e) TEM image of the 2D structure of the blue area (reprinted from [9]); (f) natural opal gemstone and (g) SEM image of the 3D silica sphere structure (reprinted from [10]). The scale bar in (c), (e) and (f) is 1 µm. Images (b), (d) and (f) by Wikimedia Commons.

PhCs are able to inhibit the propagation of light in certain frequency windows and provide quite unique ability to manipulate light, somewhat like semiconductors allow one to control the electron current (see Appendix A.7).

Since the pivotal papers issued in 1987 by Yablonovitch [6] and John [7], who first suggested the possibility of controlling spontaneous emission using periodic structures, PhCs have attracted considerable attention, and a wide variety of periodic structures with different dimensionality has been accessed with conventional nanofabrication techniques. Research has primarily focused on 2D systems. In practical devices, 2D PhCs typically come embedded within the guiding core of a slab waveguide, in the form of a so-called *PhC slab*, as shown in Fig. 1.7(a), where a self-standing membrane is etched with cylindrical air holes arranged in a hexagonal lattice. PhC slabs allow for strong optical confinement owing to the combination of a PBG effect (in-plane) and TIR (out-of-plane). A detailed account can be found in [8]. On a side note, PhCs also occur in the natural world, e.g., opals, natural gemstones consisting of periodically packed sub-micrometric spheres of amorphous silica (Fig. 1.7(f),(g)). Other examples are found in numerous biological systems, from bird feathers to butterfly wings, whose distinctive iridescence is the signature of PBG effects due to their regularly arranged internal structures (Fig. 1.7(b)–(e)).

As stated above, the most important feature of PhCs is the existence of a PBG, for which light cannot propagate through the crystal. However, if one introduces a defect to the periodic structure, new modes can be supported within the PBG. A defect can be created by shifting, missing, or resizing one or more lattice elements.

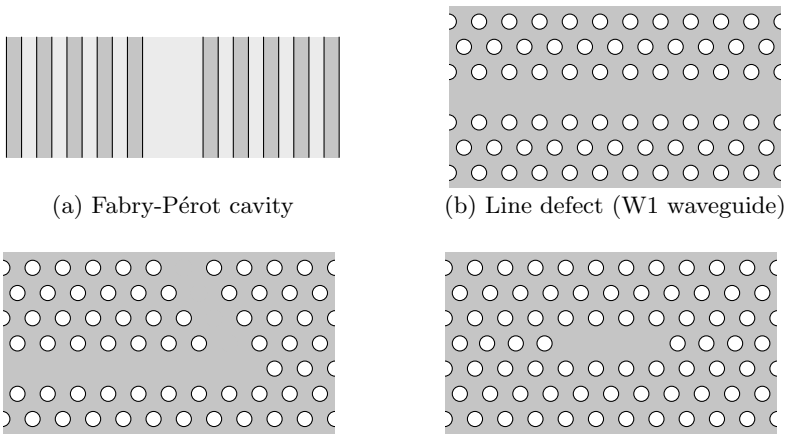

(a) Fabry-Pérot cavity (b) Line defect (W1 waveguide)

(c) Sharply-bent line defect (d) Point defect (L3 cavity)

FIGURE 1.8. Schematics of different defects in PhC systems.

The paradigmatic example is introducing a defect layer in a 1D PhC, thus forming a so-called Fabry-Pérot (FP) microcavity (Fig. 1.8(a)). In 2D PhC slabs, line defects lead to the realization of optical waveguides (Fig. 1.8(b)), even with sharp bends (Fig. 1.8(c)), while point defects give rise to cavities that are able to localize light in all dimensions (Fig. 1.8(d)). A detailed review is given in [11].

1.2. Bloch surface waves

The photonic band structure of a 1D PhC is conveniently calculated by means of the transfer matrix method (TMM), which is summarized in Appendices A.3 and A.8. Let us consider the case of a two-layer unit cell consisting of two dielectric layers of refractive indices n_1 and n_2 ($n_1 < n_2$), and thicknesses d_1 and d_2, as shown in Fig. 1.6(b). The period of the structure is $\Lambda = d_1 + d_2$. In the notation of Appendix A.3, the unit-cell transfer matrix can be calculated in terms of ordered multiplication of interface and propagation matrices in the form $\mathbf{M}_\Lambda = \mathbf{\Phi}_2\mathbf{I}_{1,2}\mathbf{\Phi}_1\mathbf{I}_{2,1}$. The photonic band structure can be found by means of the compatibility equation (A.47). Straightforward calculations yield

$$\cos(q\Lambda) = \cos(w_1 d_1)\cos(w_2 d_2) - \frac{1}{2}\left(p + \frac{1}{p}\right)\sin(w_1 d_1)\sin(w_2 d_2), \tag{1.1}$$

where q is the Bloch wavevector, $w_i = \sqrt{k_i^2 - \beta^2}$ is the wavevector component along the stacking direction in the layer i, with $k_i = n_i\omega/c$ and β the propagation constant, and p depends on the polarization as

$$p = \frac{w_2}{w_1} \quad \text{(TE modes)}, \qquad p = \frac{w_2}{w_1}\frac{n_1^2}{n_2^2} \quad \text{(TM modes)}. \tag{1.2}$$

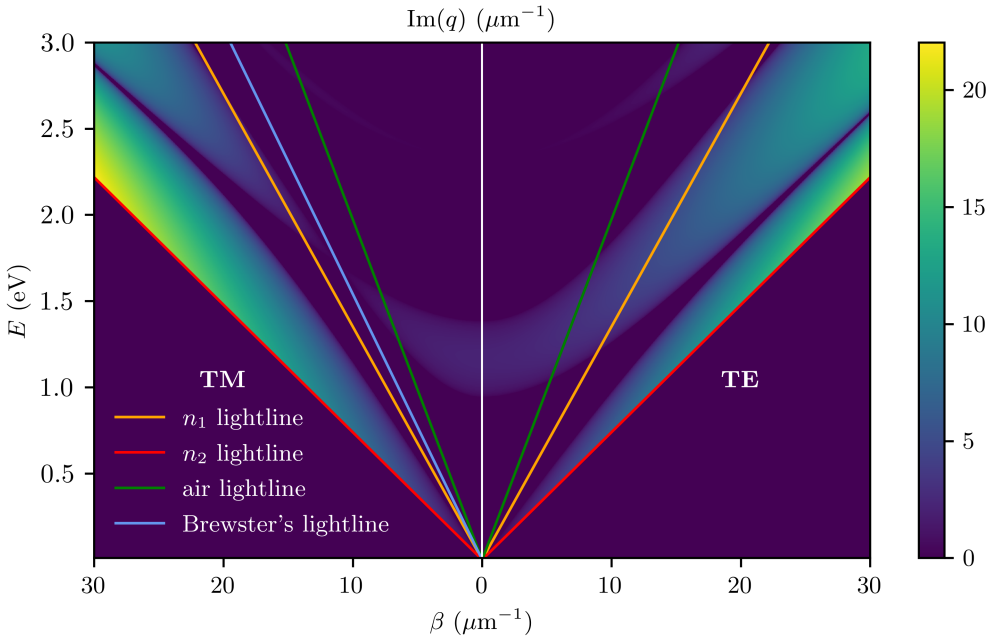

FIGURE 1.9. Photonic gapmap of a typical 1D PhC crystal for TE (right axis) and TM (left axis) polarization. The multilayer is assumed of refractive indices $n_1 = 1.46$ and $n_2 = 2.67$, and thicknesses $d_1 = 182\,\text{nm}$ and $d_2 = 100\,\text{nm}$. The solid lines are the low-refractive-index lightline (orange), high-refractive-index lightline (red), air lightline (green), and Brewster's lightline (lightblue). Notice that this gapmap makes sense only when the chromatic dispersion of the materials can be neglected.

Eq. (1.1) gives the dispersion relation between ω, β, and q (for a given polarization) in the form of an implicit equation. The allowed modes occur when the absolute value of the RHS is lower than unity, for which q is real and thus corresponds to propagating fields. By contrast, when the absolute value of the RHS exceeds unity, q is complex with a non-null imaginary part and the field is evanescent, the larger the imaginary part of q, the faster its decay within the crystal. These regions are the forbidden PBGs. The band edges (BEs) are those where the absolute value of the RHS equals unity. Solving Eq. (1.1) numerically, one can easily provide a *gapmap* for both TE and TM polarization. Fig. 1.9 shows the magnitude of $\text{Im}(q)$ as a function of β and ω for a representative periodic multilayer. Areas where $\text{Im}(q) = 0$ correspond to propagating states, whereas areas where $\text{Im}(q) > 0$ are PBGs where only evanescent states exist. Remarkably, TM PBGs close when approaching the Brewster's lightline $\omega = c\beta/(n_1 \sin \vartheta_p)$, with $\vartheta_p = \arctan(n_2/n_1)$, since TM modes propagate without any reflection across the interfaces at Brewster's angle ϑ_p [12].

Fig. 1.10 illustrates the band structure of the same periodic multilayer of Fig. 1.9 for the special case $\beta = 0$ (normal incidence). The periodicity of the photonic lattice folds the dispersion curves in the first Brillouin zone $(-\pi/\Lambda, \pi/\Lambda)$. Since the photonic

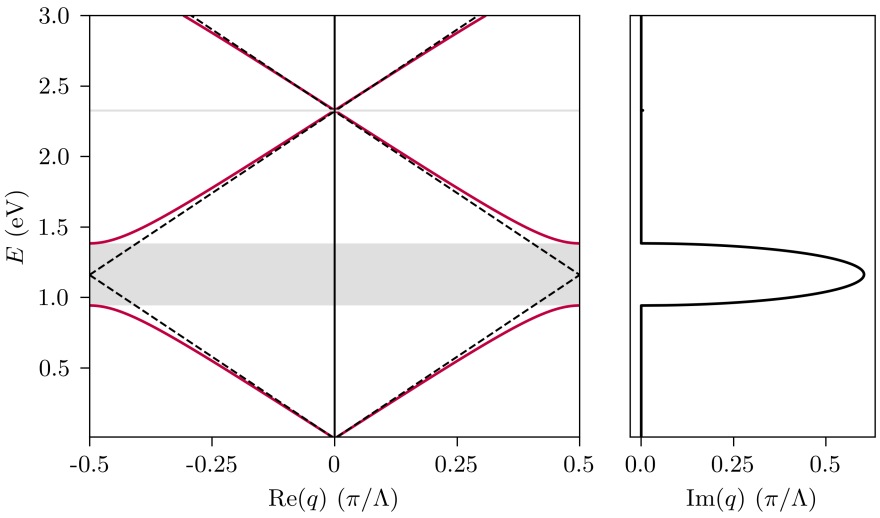

FIGURE 1.10. Projected band structure of the 1D PhC of Fig. 1.9 for light propagating in the direction normal to the multilayer ($\beta = 0$). Left panel: allowed bands and forbidden gaps (shaded areas) folded in the first Brillouin zone. Notice that the second-order gap is extremely narrow. The dashed lines indicate the (folded) average-refractive-index lightline. Right panel: imaginary part of the Bloch wavevector q within the PBGs.

modes that occupy the high-refractive-index (low-refractive-index) material tend to minimize (maximize) their energy, the bands below and above each PBG are generally referred to as the dielectric band and air band, respectively, in analogy to the valance band and conduction band in semiconductors. Notably, near the BEs, the dispersion becomes flat, the group velocity is close to zero, and the density of states (DOS) becomes ideally infinite. Such regime of "slow light" is of great interest for achieving stronger light-matter interaction or enhancing nonlinear processes [13, 14].

The normal-incidence PBG is maximed for a quarter-wave multilayer, i.e., when the layer thicknesses d_1, d_2 satisfy the condition $k_1 d_1 = k_2 d_2 = \pi/2$. In this specific case, it can be shown that the first-order midgap frequency is [4]

$$\omega_{\text{mid}} = \frac{n_1 + n_2}{4 n_1 n_2} \frac{2\pi c}{\Lambda}. \tag{1.3}$$

If the refractive index contrast is small, i.e., $\Delta n = |n_1 - n_2| \ll n$, with $n = (n_1 + n_2)/2$ being the average refractive index, the midgap frequency in (1.3) is approximately $\omega_{\text{mid}} = \pi c/(n\Lambda)$, and Eq. (1.1) can be solved analytically in the proximity of ω_{mid}. The gap width results

$$\Delta\omega = \frac{4}{\pi}\omega_{\text{mid}} \frac{|n_1 - n_2|}{n_1 + n_2} \simeq \frac{2}{\pi}\omega_{\text{mid}} \frac{\Delta n}{n}, \tag{1.4}$$

and the complex Bloch wavevector at the center of the PBG is

$$q = \frac{\pi}{\Lambda} + \mathrm{i}\frac{\Delta n}{n\Lambda}. \tag{1.5}$$

By introducing a defect into the periodic structure, translational invariance is broken and modes can be supported within the PBG. In particular, when an infinite periodic multilayer is truncated at the appropriate thickness, localized surface modes can appear at the interface between the truncated multilayer and the external homogeneous medium. These modes are known as *Bloch surface waves* (BSWs). An example is presented in Fig. 1.11 starting from the same multilayer of Figs. 1.9 and 1.10 The first high-refractive-index layer is truncated to a thickness σd_2, with $\sigma = 0.11$. The dispersion relation is located within the multilayer PBG and below the lightline of the external dielectric medium (here, air). Not only does the mode have an evanescent tail in the external medium, but also its field envelope decays exponentially inside the multilayer, the maximum intensity being close to the truncation interface.

BSWs are characterized by a strong field confinement at the truncation surface, with surface field enhancements up to 45% larger than those achievable in dielectric slabs [15]. Their dispersion relation can be tuned within the PBG by carefully choosing the multilayer composition (thicknesses and permittivities) and termination condition. A procedure to minimize the decay length of the electric field into the multilayer by adjusting the truncation factor σ is presented in Appendix A.8. Furthermore, the deposition of an additional dielectric layer on top of the structure can provide further control of the dispersion and optical properties of the surface mode, such as the field decay length or the energy density localization at a generic point [16]. In Fig. 1.12 we show the effect of an additional layer on top of the bare structure of Fig. 1.11 on the BSW dispersion relation and intensity profile.

A phenomenological comparison can be made between BSWs and another type of surface electromagnetic wave, *surface plasmon polaritons* (SPPs), which propagate along the planar interface between a metal and a dielectric medium through collective oscillations of electron plasma in the metal [17]. As for BSWs, the electromagnetic field of SPPs is confined in the close proximity of the metal/dielectric interface, with evanescent decay in the normal direction (Fig. 1.13). SPPs can also be confined in 2D waveguides, e.g., by depositing a thin metal strip on top of a dielectric slab (metal-on-isulator SPPs) or, vice versa, by patterning a dielectric ridge on top of a metal film (dielectric-loaded SPPs), which can be readily done by using lithographic resists. SPPs are nowadays a well-established photonic platform for a large number of applications, from optical sensing to integrated circuitry [18]. However, compared to BSWs, SSPs have some inherent shortcomings [19]. First, the SPP dispersion is determined only by the properties of the constituent materials, which limits their choice to a small number of suitable metals. On the contrary, BSW dispersion can be tuned at almost any wavelength (from UV to mid-IR) by properly selecting the geometrical and physical parameters of the structure (thicknesses and permittivities). Second, the

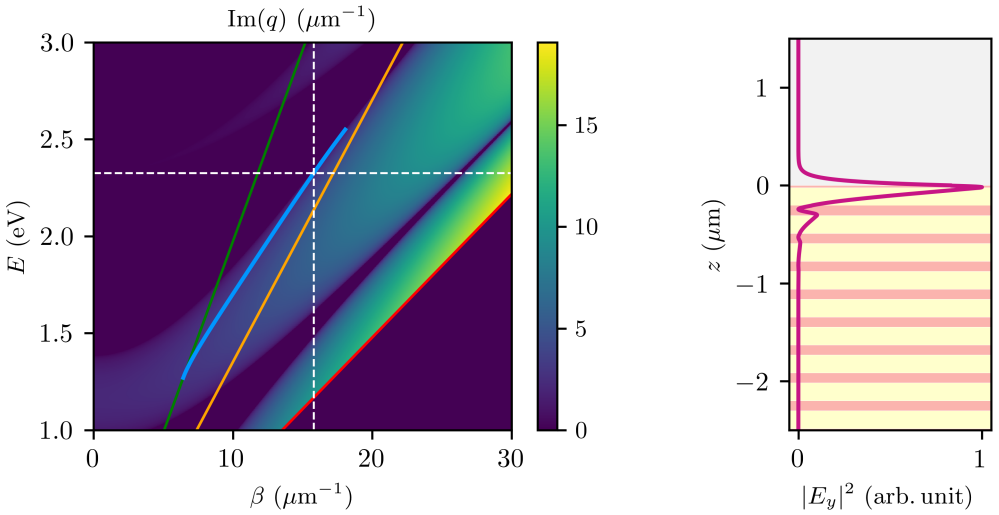

FIGURE 1.11. Left: BSW dispersion relation (TE polarized) (solid lightblue). The multilayer consists of alternating layers of refractive indices $n_1 = 1.46$ and $n_2 = 2.67$, and thicknesses $d_1 = 182\,\text{nm}$ and $d_2 = 100\,\text{nm}$, respectively, and is truncated on the high-refractive-index layer with truncation thickness $d_{\text{trunc}} = 11\,\text{nm}$. The external medium is air. In the simulation, a number $N = 15$ of multilayer periods is taken. The PBG (regions with nonnull $\text{Im}(q)$) and the lightlines for air (solid green), low-refractive-index material (solid orange), and high-refractive-index material (solid red) are also shown. Right: mode intensity profile calculated at $\lambda_0 = 532\,\text{nm}$ (2.33 eV). The calculated effective index is $n_{\text{eff}} = 1.3416$ (dashed white lines in the left panel).

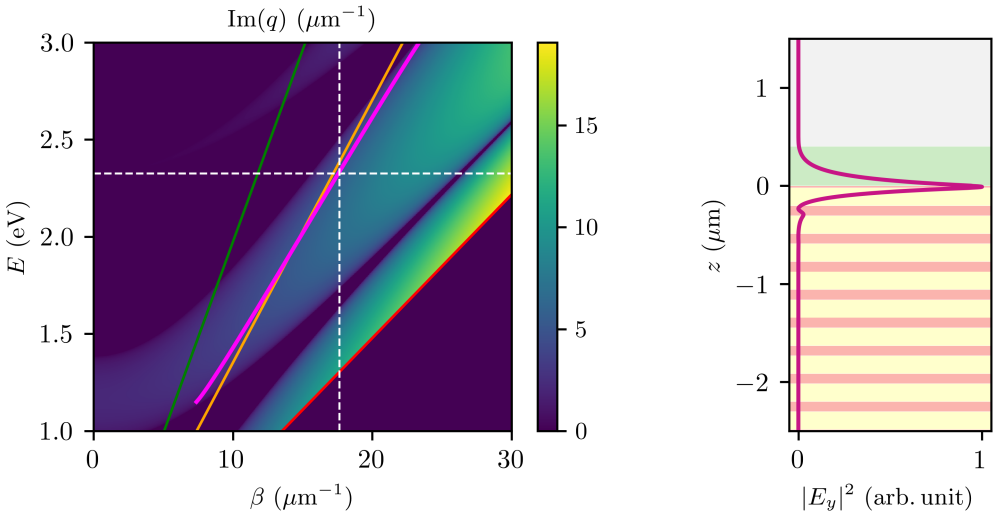

FIGURE 1.12. Left: BSW dispersion relation sustained by a dielectric-loaded multilayer (TE polarized) (solid pink). The structure is the same of Fig. 1.11 with an additional dielectric layer of refractive index $n_3 = 1.49$ and thickness $d_3 = 400\,\text{nm}$. Notice that the photonic gap map is the same as the one in Figs. 1.9 and 1.11 because it is a bulk property of the PhC and depends on the multilayer composition only. Right: mode intensity profile calculated at $\lambda_0 = 532\,\text{nm}$ (2.33 eV). The calculated effective index is $n_{\text{eff}} = 1.4918$ (dashed white lines in the left panel).

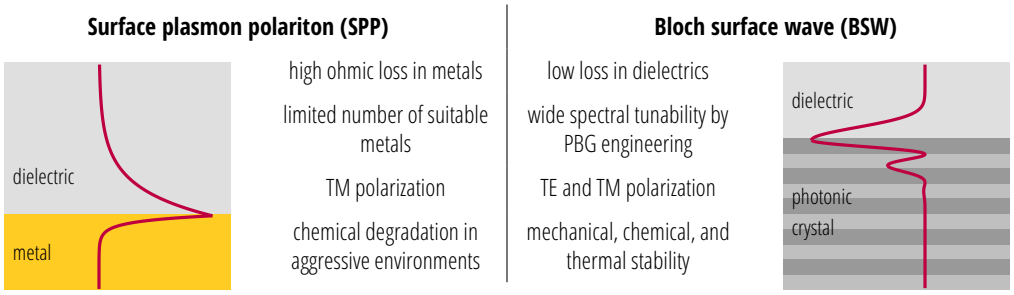

FIGURE 1.13. Advantages of BSWs with respect to SPPs.

large ohmic loss that affect metals at optical frequencies results in low propagation lengths of SPPs, typically tens or thousands of microns, but even up to millimeters in long-range SPPs (though at the cost of weaker field localization, making them less practicable in highly integrated optical circuits). BSWs can theoretically propagate over much longer distance owing to the use of dielectric materials. Third, SPPs are TM polarized in nature, while BSWs can be excited in both TE and TM polarization. Finally, with an appropriate choice of the constituent materials, multilayers provide mechanical stability and chemical robustness, offering the possibility of working in more aggressive environments.

BSWs have been known since the late 1970s [20–22], although the first experimental observations were conducted by Robertson et al. in the 1990s [23–25]. A renewed interest has been driven by the development of fabrication techniques that allow one to obtain high-quality multilayers with tens of periods quite inexpensively. A number of different dielectric materials can be used to fabricate multilayers that sustain BSWs, these including titania (TiO_2)/silica (SiO_2), tantalum pentoxide (Ta_2O_5)/silica, silicon nitride (Si_3N_4)/silica, porous Si (p-Si), and amorphous silicon-based alloys such as hydrogenated silicon nitride (a-SiN:H), silicon carbide (a-SiC:H), and silicon oxide (a-SiO:H). This allows one to operate in a wide spectral range, particularly at visible wavelengths, for which there is paucity of transparent materials having a strong refractive index contrast.

Numerous works have focused on chemical and biological sensing applications of BSWs because of their strong field enhancement at the structure surface and high sensitivity to the refractive index changes of the surrounding medium [26, 27]. In life science applications, BSW-based sensors using different sensing schemes (fluorescence-based and label-free) and measurement techniques (wavelength, angle, intensity and phase interrogation) have been reported. In fluorescence-based sensing, fluorescent labels such as organic dyes and quantum dots are used to detect the presence of the target analytes. In this respect, the strong electromagnetic field intensity of BSWs at the truncation layer can be exploited to obtain enhanced and/or directional emission

of fluorophores placed at the structure surface. As an example, Ballarini et al. demonstrated the BSW-driven amplification of the fluorescence signal from dye-labeled proteins on a polymer-loaded multilayer [28]. Toma et al. further improved the excitation rate and collection efficiency of fluorescence light by employing a two-segment multilayer [29]. On the other hand, label-free schemes allow for direct detection of the target analytes, for instance, by monitoring the spectral shift of the optical resonance in response to the analyte-induced refractive index variation. It offers a relatively simple and cost-effective alternative to fluorescence-based sensors. In terms of sensitivity (i.e., the ratio $\Delta\lambda/\Delta n$, where $\Delta\lambda$ is the resonance spectral shift on account of the local refractive index variation Δn), BSWs are inherently sensitive to small changes in the refractive index of the external dielectric environment. In recent years, various label-free sensors based on BSWs have been developed for the detection of different analytes and using different measurement techniques. Just to name a few, Paeder et al. demonstrated the application of an angular-sensitive sensor to the detection of protein aggregation [30]. Farmer et al. investigated antibody/antigen reactions and DNA binding by monitoring the shift in the BSW resonance wavelength [31]. Similarly, Rivolo et al. showed label-free detection of antibody/anti-antibody binding [32]. Rodriguez et al. reported size-selective sensing of large and small molecules using BSWs and Bloch sub-surface wave (BSSWs) in a p-Si multilayer [33]. Sinibaldi et al. [34] and Li et al. [35] demonstrated that the rapid phase variation of the BSW sensor caused by the environment refractive index changes can enhance the device sensitivity, while Kong et al. showed that intensity interrogation can lead to sensitivities comparable or higher than those of plasmonic sensors [36]. Notably, Sinibaldi et al. reported a sensing platform capable of working simultaneously in a label-free and fluorescence mode on the same readout system [37] and its use for clinical detection of cancer biomarkers [38]. On a final note, we mention that alternative schemes based on enhanced diffraction [39–41] and surface enhanced Raman scattering [42, 43] have been proposed.

Beside optical sensing, BSWs have great potential for integrated optics applications. Descrovi et al. demonstrated that, starting from a truncated multilayer supporting a 1D BSW, it is possible to control such excitation in the plane of the structure by simply loading the bare multilayer with a dielectric ridge [44]. This has paved the way for the realization of various planar optical components based on 2D BSWs. Wu et al. investigated the propagation of BSWs in ultrathin polymeric curved waveguides [45]. Yu et al. showed focusing of BSWs on top of the multilayer through a planar lens [46]. This concept was used by Angelini et al. to inject BSWs into ultrathin polymeric ridges [47]. Later, Dubey et al. reported the first experimental realization of a BSW-based microdisk resonator [48], while Rodriguez et al. fabricated

the first BSW-based microring resonator [49]. Kovalevich et al. proposed a 2D grating coupler with polarization-switching capability [50]. More recently, following their study on multimode interference of BSWs, Safronov et al. demonstrated the operation of a Mach–Zehnder interferometer using polymeric ridges [51]. Remarkably, many of these structures are obtained from low-refractive-index materials such as polymers, which can be readily structured by standard lithography techniques [52]. Such ease of manipulation makes BSWs highly promising for the development of an etchless, all-dielectric integrated platform.

1.3. Passive components for integrated optics

The ultimate goal of integrated optics is the realization of robust, small-footprint optical devices that allow one to generate, route, process, and detect light on a single chip. Silicon-on-insulator (SOI) has doubtlessly become the leading platform for a low-cost, large-scale integration owing to its high refractive index contrast ($n_{\mathrm{Si}} \simeq 3.45$ and $n_{\mathrm{SiO_2}} \simeq 1.44$ at 1550 nm) and compatibility with mature complementary metal-oxide semiconductor (CMOS) technology. Other material platforms can also be adopted, such as silicon nitride (SiN), lithium niobate (LN), gallium arsenide (GaAs), indium phosphide (InP), high-index doped silica glass, laser-written silica glass, and polymers (acrylic plastics, epoxy resins, etc.). Each platform has its own advantages and disadvantages, making them more suitable for the realization of certain components than others. It is beyond the scope of this work to discuss these properties in detail. A wide variety of tutorial reviews exist on the topic for the interested reader [53–58].

The principal building blocks of an integrated optical device are (i) *active components*: lasers, modulators, switches, photodetectors, and (ii) *passive components*: waveguides, microresonators, couplers, splitters, filters, demultiplexers. For the purpose of this dissertation, we shall focus on passive components.

Waveguides. Waveguides are essential elements in integrated optics, as they allow one to control the flow of light in the device. As seen in previous sections, one can exploit conventional TIR-based waveguides, in which light is confined within a high-refractive-index, small-cross-section core, or line-defect waveguides in PhC slabs, in which light is guided along the defect by PBG confinement on the two sides and by TIR in the out-of-plane direction. Alternative approaches based on surface electromagnetic waves (SPPs, BSWs, etc.) are also possible.

In general, a *guided mode* is an electromagnetic wave that propagates along a particular waveguide structure with distinct phase velocity, group velocity, transverse field profile, and polarization. For a 2D waveguide operating at frequency ω, the

Material platform	Range	Configuration	Propagation loss (dB/cm)	Ref
Silicon (Si)	NIR	Submicrometric SOI wire waveguide	0.1 (1310 nm)	[59]
Gallium arsenide (GaAs)	NIR	GaAs/AlGaAs rib waveguide	1.6 (1550 nm)	[60]
		GaAs-based single-line defect PhC slab waveguide	0.76 (1550 nm)	[61]
Indium phosphide (InP)	NIR	InP waveguides based on local Zn-diffusion	0.4 (1550 nm)	[62]
Fused silica	Vis–NIR	Laser-written waveguide in fused silica	0.06 (777 nm)	[63]
		High-index doped silica glass (Hydex) waveguide	0.06 (1550 nm)	[64]
Lithium niobate (LN)	Vis–NIR	LN-on-insulator waveguide	0.06 (630 nm)	[65]
		LN-on-insulator waveguide	0.02 (1550 nm)	[66]
Silicon nitride (SiN)	Vis–NIR	Single-mode PECVD SiN wire waveguide	2.25 (532 nm)	[67]
		High-aspect-ratio SiN waveguide	0.09 (1550 nm)	[68]
Polymer	Vis–NIR	PMMA-based waveguide using femtosecond laser	0.3 (637 nm)	[69]
		Acrylate-based waveguide	0.8 (1550 nm)	[70]
Polymer-based LRSPPs	NIR	Polymer-based long-range surface plasmon polariton (LRSPP) waveguide	0.8 (1550 nm)	[71]

TABLE 1.1. Comparison of selected waveguides in different material platforms.

electric field of a guided mode is of the form

$$\mathbf{E}(\mathbf{r},t) = \mathbf{E}(y,z)\mathrm{e}^{\mathrm{i}\beta x - \mathrm{i}\omega t} \tag{1.6}$$

where $\mathbf{E}(y,z)$ is the field profile in a plane transverse to the propagation direction and β is the propagation constant. The value of β defines the *effective mode index* $n_{\mathrm{eff}} = \beta c/\omega$, meaning that the mode propagates along the waveguide with a phase velocity $v_p = c/n_{\mathrm{eff}}$. In contrast to planar waveguides, which support only TE or TM modes, 2D waveguides support hybrid modes owing to the light confinement being in both transverse directions. In *channel waveguides*, modes usually have either the dominant electric (TE-like) or magnetic (TM-like) field component in the direction parallel to the planar layers. For most applications, it is preferable to operate in a single-mode regime for each polarization.

The power of a guided mode is attenuated as it propagates along the waveguide:

$$P(L) = P(0)\mathrm{e}^{-\alpha L}, \tag{1.7}$$

where $P(0)$ is the input power, $P(L)$ is the output power over a propagation distance L in the waveguide, and α is the *power attenuation coefficient* (expressed in m^{-1}). This is caused by several loss mechanisms, e.g., material absorption, scattering from surface roughness, etc. The total loss (per unit length) can be accounted for by adding

an imaginary part to the propagation constant β:

$$\alpha\,(\mathrm{m}^{-1}) = -\frac{1}{L\,(\mathrm{m})}\ln\frac{P(L)}{P(0)} = 2\,\mathrm{Im}(\beta), \tag{1.8}$$

with $\mathrm{Im}(\beta) > 0$, which results in the exponential power decay of Eq. (1.7). Conventionally, α is also given in dB/m:

$$\alpha\,(\mathrm{dB/m}) = -\frac{1}{L\,(\mathrm{m})}10\log_{10}\frac{P(L)}{P(0)}. \tag{1.9}$$

Comparing (1.9) with (1.8), one obtains the conversion formula

$$\alpha(\mathrm{dB/m}) = 4.34\,\alpha(\mathrm{m}^{-1}). \tag{1.10}$$

The reported attenuation in integrated waveguides are typically around 0.1–3 dB/cm (see Table 1.1), compared with less than 1 dB/km attenuation attainable in bulk silica glass fibers [72].

Another important figure of merit is the *effective mode area*:

$$A_{\mathrm{eff}} = \frac{\left(\int |\mathbf{E}(y,z)|^2\,\mathrm{d}y\,\mathrm{d}z\right)^2}{\int |\mathbf{E}(y,z)|^4\,\mathrm{d}y\,\mathrm{d}z}, \tag{1.11}$$

which is a measure of the effective extension of the mode in the plane transverse to the propagation direction. Small effective areas are the signature of strong guiding and become significant when dealing with nonlinear effects, whose efficiency critically depends on the local distribution of the field intensity. In the latter case, the previous definition of effective area works properly for optical fibers, in which the mode power is predominantly within the guiding core. In general, the integration in the denominator of Eq. (1.11) should be carried over the cross section of the core hosting the nonlinear material [73]:

$$A_{\mathrm{eff,nl}} = \frac{\left(\int |\mathbf{E}(y,z)|^2\,\mathrm{d}y\,\mathrm{d}z\right)^2}{\displaystyle\int_{\mathrm{nl\,core}} |\mathbf{E}(y,z)|^4\,\mathrm{d}y\,\mathrm{d}z}. \tag{1.12}$$

Microresonators. Microresonators have a broad range of application in integrated optics owing to their ability to store light in a small volume and for a long period of time. They are characterized by two key parameters, the *quality factor* Q and the *mode volume* V. The Q factor quantifies the enhancement of the electromagnetic field intensity in the resonator due to temporal confinement, while the mode volume V determines the enhancement due to spatial confinement, the overall enhancement being proportional to the ratio Q/V.

The Q factor is defined as the ratio of the resonance frequency ω_{res} and the energy decay rate γ of the resonator. Assuming that the energy stored in the resonator decays with time constant $\tau = 1/\gamma$, it can be written as

$$Q = \omega_{\text{res}} \left(\frac{\text{energy stored in the resonator}}{\text{average power dissipation}} \right) = \frac{\omega_{\text{res}}}{\gamma} = \omega_{\text{res}} \tau. \tag{1.13}$$

It can also be understood as the number of oscillation cycles required for the stored energy to be damped by a factor 1/e. In general, multiple mechanisms can lead to energy loss in a resonator, each of which can be accounted for by an individual quality factor Q_i. The total quality factor Q is given by

$$\frac{1}{Q} = \sum_i \frac{1}{Q_i}. \tag{1.14}$$

From Eq. (1.14) it is apparent that the total Q is limited by the smallest individual Q_i, i.e., by the largest loss mechanism. In literature, it is customary to express the Q factor as $Q^{-1} = Q_{\text{int}}^{-1} + Q_{\text{ext}}^{-1}$, in which Q_{int} accounts for radiation loss, material absorption, scattering from fabrication imperfections and impurities, etc. (intrinsic Q factor), and Q_{ext} accounts for loss due to in and outcoupling (extrinsic Q factor). The total Q factor is usually referred to as the loaded Q factor.

The mode volume V can be defined as follows:

$$V = \frac{\int \varepsilon(\mathbf{r}) |\mathbf{E}(\mathbf{r})|^2 \, \mathrm{d}\mathbf{r}}{\max[\varepsilon(\mathbf{r}) |\mathbf{E}(\mathbf{r})|^2]}. \tag{1.15}$$

Despite its name, the mode volume can differ significantly from the spatial extension of the mode or the actual size of the resonator. As a rule of thumb, Q scales with V. It can be qualitatively understood by considering that the larger the resonator, the longer the time spent by light in it. Hence, achieving a high Q/V ratio to maximize the field enhancement is a difficult task, but careful designs can lead to satisfactory tradeoffs [74].

Whispering-gallery-mode (WGM) resonators have achieved some of the highest Q factors. In particular, *microrings* have gained increasing interest due to their potential for high-density integration in a multitude of different material platforms [83]. Their application include filtering and demultiplexing [84], modulation [85], sensing [86], nonlinear interaction enhancement [87], quantum information processing [88], just to name a few. A common configuration is the all-pass filter sketched in Fig. 1.14, in which the optical energy can transfer to the ring from an adjacent bus waveguide through evanescent coupling. The gap distance between the ring and bus determines the strength κ of the coupling. In order to achieve resonance, an integer number of

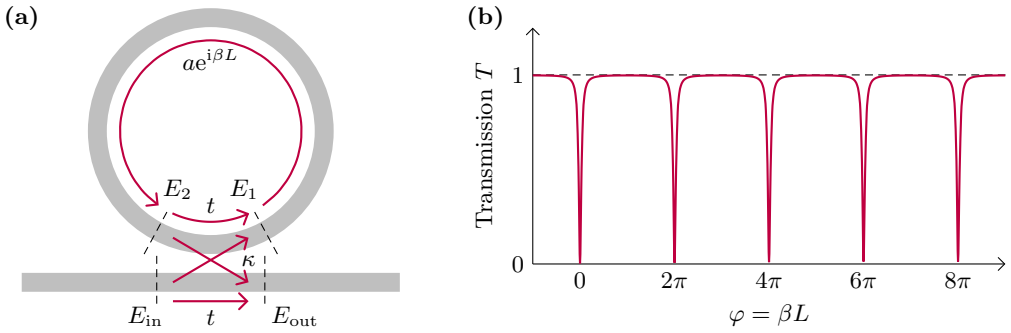

FIGURE 1.14. (a) Scheme of an all-pass microring resonator. Light is coupled to the ring from a bus waveguide. The coupling region is described as a point coupler of cross-coupling coefficient κ and self-coupling coefficient t, with $\kappa^2 + t^2 = 1$. The coefficient $a = e^{-(\alpha/2)L}$ represent the loss after one roundtrip, with α the power attenuation coefficient; β is the propagation constant of the circulating mode and L the roundtrip length. (b) Transmission spectrum $T = |E_{out}/E_{in}|^2$ of the all-pass microring as a function of the phase shift $\varphi = \beta L$ under critical coupling ($a = t$). The resonances are equally spaced.

Material platform	Range	Configuration	R (um)	FSR (pm)	Q	Ref
Indium phosphide (InP)	NIR	InP ring resonator	13,000	17.8	0.97M	[75]
Silicon (Si)	NIR	SOI microring resonator	2,450	45.7	22M	[76]
	NIR	Submicrometer-SOI racetrack resonator	29+260	900	1.3M	[77]
Silica-based	NIR	Silica-based racetrack resonator	1,600	137	1.83M	[78]
Lithium niobate (LN)	Vis-NIR	LN-on-insulator microring resonator	100	–	11M	[66]
		LN-on-insulator microring resonator	80	–	10M	[65]
Silicon nitride (SiN)	NIR	On-chip SiN microring resonator	115	–	37M	[79]
	NIR	Planar integrated all-waveguide SiN resonator	11,787	17.4	422M	[80]
Polymer	Vis	SU-8 microring resonator fabricated by nanoimprint lithography	60	2000	0.8M	[81]
Polymer-based LRSPPs	NIR	Polymer hybrid plasmonic ring resonator	25	–	270	[82]

TABLE 1.2. Comparison of selected microring resonators in different material platforms.

effective wavelengths must fit in one roundtrip length L:

$$\lambda = \frac{n_{\text{eff},m} L}{m}, \tag{1.16}$$

where m is the resonance order and $n_{\text{eff},m}$ is the effective index of the mode propagating in the ring. The transmission spectrum of the bus waveguide exhibits equally spaced dips at the ring resonances, which drop to zero under critical coupling, i.e., when the coupled power is equal to the power loss in the ring ($\kappa^2 = 1 - \exp(-\alpha L) \simeq$

αL, with α the power attenuation coefficient), as illustrated in Fig. 1.14(b). The free spectral range (FSR), i.e., the wavelength separation between neighboring resonances, is given by

$$\mathrm{FSR}_\lambda = \frac{\lambda^2}{n_g L}, \tag{1.17}$$

where n_g is the group index of the propagating modes. The intrinsic and extrinsic Q factors can be expressed as

$$Q_{\mathrm{int}} = \frac{2\pi n_g L}{\lambda(\alpha L)} \qquad \text{and} \qquad Q_{\mathrm{ext}} = \frac{2\pi n_g L}{\lambda \kappa^2}, \tag{1.18}$$

respectively, with the loaded Q factor being given by $Q^{-1} = Q_{\mathrm{int}}^{-1} + Q_{\mathrm{ext}}^{-1}$. Typical values are in the range 10^4–10^5, though recent research efforts resulted in ultra-high values exceeding 10^8 in millimeter-scale microrings. Some selected examples in different host materials are reported in Table 1.2.

Mode volumes in high-Q microrings can be quite large due to the large bend radii, which makes them not suitably sized for dense integration and limits their use in those application requiring high optical field strengths, e.g., spontaneous emission or strong coupling. Therefore, nanocavities based on PhCs, capable of achieving mode volumes as small as the diffraction limit $(\lambda/n)^3$, have been explored as an attractive alternative. The best performing PhC nanocavities are realized in PhC slabs, especially in self-standing Si membranes, by omitting a single hole (H1 cavity) or three holes (L3 cavity) in a hexagonal lattice. By tuning position and radius of the holes in the immediate vicinity of the cavity, Q factors exceeding 10^7 are predicted numerically [89], with experimental values up to 10^6 due to fabrication limitations [90]. Higher Q factors can be achieved in heterostructure cavities formed by connecting PhC line-defect waveguides with slightly different structural parameters, such as the longitudinal lattice constant, waveguide width, or slab refractive index [91–93]. However, such structures are quite challenging to fabricate, and usually require a sufficiently large refractive index contrast of the constituent materials.

A different approach is that of photonic crystal nanobeam cavities (PhCNCs), which exploit the presence of a PBG along a waveguide segment in which light is confined transversely by TIR (Fig. 1.15(a)). Although wavelength-scale mode volumes can be achieved quite straightforwardly, high Q factors are more challenging to obtain [106]. The rule of thumb to increase Q is that the mode field should not terminate abruptly at the cavity edges, as this would lead to significant in-plane diffraction (Fig. 1.15(b)). Quite the contrary, its spatial variation should be as smooth as possible at the cavity edges, thus enabling more gradual reflection by the Bragg mirrors [107, 108]. In practice, this "gentle confinement" requires tapering the Bragg mirrors into the cavity region, e.g., by gradually resizing or shifting neighboring holes towards

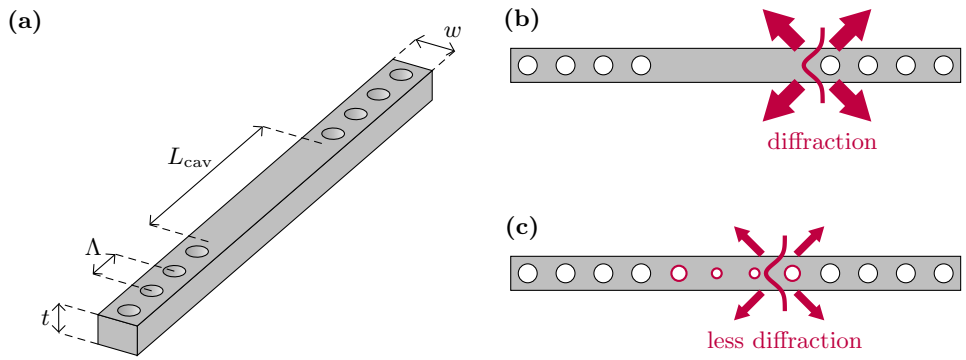

FIGURE 1.15. (a) Schematics of a PhC nanobeam cavity consisting of a waveguide segment of length L_{cav}, width w, and thickness t, embedded by two Bragg mirrors of lattice constant Λ. (b) Light diffraction at the cavity edges. (c) Mitigation of diffraction due to tapering of holes.

Material platform	Range	Configuration	Q factor	mode V $(\lambda/n)^3$	Ref
Silicon (Si)	NIR	Circular hole PhCNC	58,000	0.6	[94]
		Circular hole/ladder/stack mode-gap cavities in SOI and Si air-bridge	220,000–750,000	0.5–1.4	[95]
		Bowtie-shaped unit cell PhCNC	100,000	0.001	[96]
		Width-modulated PhC stack mode-gap cavity	27,000	1.48	[97]
		Nanoslotted single PhCNC	10,000	0.025	[98]
		Slotted PhCNC with parabolic modulated width	10,000	0.22	[99]
Silica (SiO_2)	Vis	Circular hole nanobeam in SiO_2	5,000	2.0	[100]
Polymer	NIR	Low-index-contrast polymeric PhCNC	36,000	–	[101]
InP-based	NIR	Stick-like cavity with tapered air holes	100,000	–	[102]
Porous silicon (p-Si)	NIR	PhCNC based on p-Si	9,000	–	[103]
SiN	Vis–NIR	Suspended SiN nanobeam	55,000	0.55	[104]
		SiN-on-insulator	440,000	–	[105]

TABLE 1.3. Comparison of selected PhC nanobeam cavities in different material platforms.

center of the cavity (Fig. 1.15(c)). Although it may induce slight increase in the mode volume V, a significant improvement of Q/V is still expected owing to the much larger increase in Q. This optimization procedure is relevant also to the scope of this dissertation, and is discussed in detail in Chapter 3. By this approach, a number of high-Q/V PhCNCs have been proposed with different geometries, from ladder to stack nanobeams, and with a vast choice of constituent materials. A partial report is given in Table 1.3. Numerical simulations show Q factors exceeding 10^8, with measured Q factors in the range 10^4–10^5, essentially limited by fabrication imperfections and

impurities. Ultra-small mode volumes $V < (\lambda_0/n)^3$ can be obtained by resorting to nanoslotted cavities [109] or engineering the geometrical shape of the unit cell (e.g., bowtie-shaped unit cell) [110]. Their application include tunable filtering [111], electro-optic modulation [112], ultra-low energy switching [113], low-threshold lasing [114, 115], biochemical sensing [116, 117], and cavity quantum electrodynamics [118].

Couplers. The small dimension of integrated waveguides makes the coupling to an optical fiber more difficult due to the large modal size mismatch. For instance, the standard single-mode fiber for telecom applications, Corning's SMF-28, has a mode field diameter of about 10.4 µm at 1550 nm (effective mode area of about 85 µm^2), compared to an effective mode area of the order of 0.1 µm^2 in submicrometric SOI waveguides. Direct edge coupling of both waveguides would result in coupling loss around −30 dB, not to mention the submicrometric alignment tolerance required. To avoid such impracticable loss, alternative coupling strategies have been found: *inverse-taper edge coupling* or *grating coupling* (Fig. 1.16).

In edge couplers, the (usually lensed) fiber is placed horizontally at the chip facet and directly aligned with the on-chip waveguide. By gradually shrinking the waveguide dimensions along the direction of propagation toward the chip edge (inverse taper), the effective mode area increases because of the weaker confinement, up to the point it becomes comparable with that of the fiber mode. By using inverse-taper edge couplers, one can achieve high coupling efficiency (i.e., the ratio between the optical power coupled to the fiber and the optical power propagating along the waveguide), with large operating bandwidth and low polarization dependence. However, post-fabrication cleaving and polishing are required to obtain high-quality coupling facets. In addition, the fiber positioning is restricted to the chip facets, with stringent alignment tolerance and impracticable wafer-level testing. To circumvent these disadvantages, one can bend the taper in the upward direction and align the fiber vertically, or use other ingenious 3D structures free from planar design limitations.

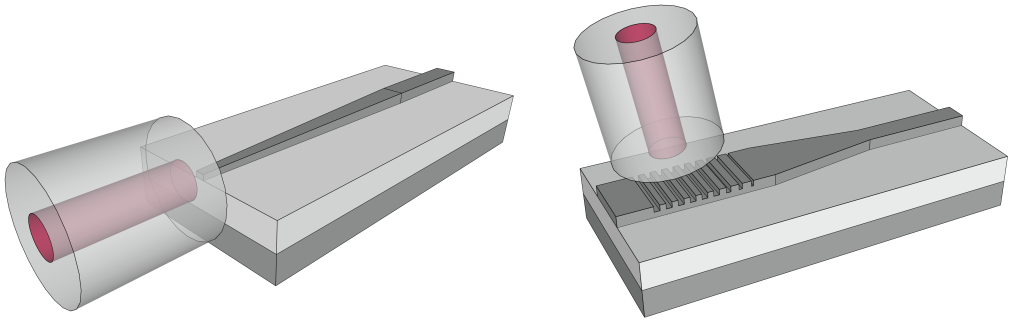

inverse-taper edge coupler grating coupler

FIGURE 1.16. Schematics of two prominent coupling schemes between optical fibers and integrated waveguides: inverse-taper edge coupler (left) and grating coupler (right).

Structure	Range	Configuration	CE (dB)	BW (nm)	Ref
Inverse-taper edge coupler	NIR	SOI edge coupler, parabolic-shape inverse taper	−3.3 (1550 nm)	–	[119]
	NIR	SOI edge coupler with polymer clad, inverse taper	−0.5 (1550 nm)	>100 (1 dB)	[120]
	NIR	SOI edge coupler	−0.25 (1550 nm)	100 (1 dB)	[121]
3D edge coupler	NIR	Vertical curved Si waveguide coupler	−2.2 (1550 nm)	>100 (1 dB)	[122]
	NIR	3D polymer coupler attached to a SiN waveguide	−2.07 (1550 nm)	>200 (1 dB)	[123]
Uniform grating coupler	NIR	SOI grating coupler	−5.2 (1550 nm)	40 (1 dB)	[124]
Directionality-enhanced grating coupler	NIR	SOI grating coupler with poly-Si overlay	−1.6 (1530 nm)	44 (1 dB)	[125]
	NIR	SOI grating coupler with Al bottom reflector	−0.58 (1560 nm)	71 (3 dB)	[126]
	Vis	SiN grating coupler with AlCu/TiN bottom reflector	−2.29 (660 nm)	–	[127]
	NIR	SOI grating coupler with bottom DBR	−1.58 (1510 nm)	36 (1 dB)	[128]
	NIR	SiN grating coupler with SOI grating bottom reflector	−1.3 (1536 nm)	80 (1 dB)	[129]
Apodized grating coupler	NIR	SOI grating coupler, pitch+duty cycle apodized	−0.9 (1550 nm)	37.4 (1 dB)	[130]
	NIR, n-Vis	LNOI grating coupler, duty cycle apodized	−3.27 (1550 nm), −3.48 (775 nm)	35 (3 dB), 11 (3 dB)	[131]
	NIR	Plasmonic grating coupler on dielectric-loaded SPP, pitch+duty cycle apodized	−2.9 (1550 nm)	115 (1 dB)	[132]

TABLE 1.4. A comparison of the coupling efficiency (CE) and bandwidth (BW) of selected couplers using different CE enhancement schemes.

Grating couplers are periodic corrugations (in one or two dimensions) that diffract light from the waveguide to free space, making it possible to couple light on top of the chip. Their behavior relies on Bragg's diffraction condition, which is nothing but a phase matching condition between the propagation constant of the waveguide mode and the wavevector of the light incident from the optical fiber above the chip. The grating vector makes up for the phase mismatch. Compared to edge couplers, grating couplers are more easily fabricated and require no additional post-processing steps. Plus, they can be placed anywhere on the chip, providing much easier fiber alignment and also wafer-level testing. On the contrary, they are intrinsically wavelength selective, with relatively narrow bandwidth, and it is not trivial to achieve high coupling efficiency, which is essentially limited by non-optimal directionality and poor overlap

between the fiber mode and the optical mode diffracted by the grating. Directionality can be increased by placing a backreflector, such as a metallic mirror or a DBR, at the bottom of the grating to recover part of the power leaked into the substrate, while the mode overlap can be enhanced by using non-uniform (apodized) gratings to produce a field distribution of the diffracted mode matching the Gaussian field distribution of the SMF fundamental mode. This requires intensive design optimization and can make the fabrication procedure more complex. Finally, 1D grating couplers are polarization sensitive, and can efficiently couple only one polarization. The working principles of 1D diffraction gratings are discussed in further detail in Chapter 4. A comparison of different couplers selected from the literature is presented in Table 1.4. A complete overview is provided in [133].

CHAPTER 2

Guiding BSWs: long-range BSWs in PhC ridges

2.1. PhC ridges supporting BSWs

BSWs can be easily managed using dielectric loading on the surface of the truncated multilayer. It makes them an interesting candidate for the development of integrated planar optical systems. The most common implementations are based on PhC ridges, which consist of a dielectric strip placed on top of the truncated multilayer. A schematic is shown in Fig. 2.1. In these structures, light confinement results from the hybrid combination of a PBG effect from the multilayer side and TIR in the other directions. Interestingly, the existence of guided modes depends very little on the ridge refractive index, which can be even lower than those of the multilayer materials.

Liscidini showed that, starting from the same multilayer but varying the ridge characteristics, PhC ridges can support at least three different kinds of modes, which the author effectively named the *good*, the *bad*, and the *ugly* (Fig. 2.2) [134]. These modes have different dispersion and field distribution, with light concentrated near the multilayer surface or in the ridge. Namely, the *good* is localized at the truncation surface irrespective of the ridge thickness. Its dispersion relation lies below the lightline of the ridge material, and thus the field is evanescent in the ridge. It is indeed a truly guided 2D BSW. The *bad* exists only in ultra-thin ridges and is characterized by a dispersion relation above the lightline of the ridge material. Unlike the good, the field is not evanescent in the ridge, and light is confined near the multilayer surface

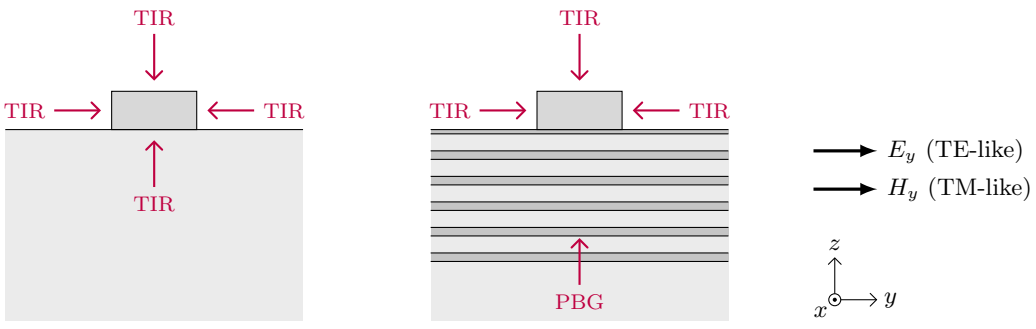

(a) ridge waveguide PhC ridge waveguide

FIGURE 2.1. Sketch of the cross section of (a) ridge waveguide and (b) PhC ridge waveguide.

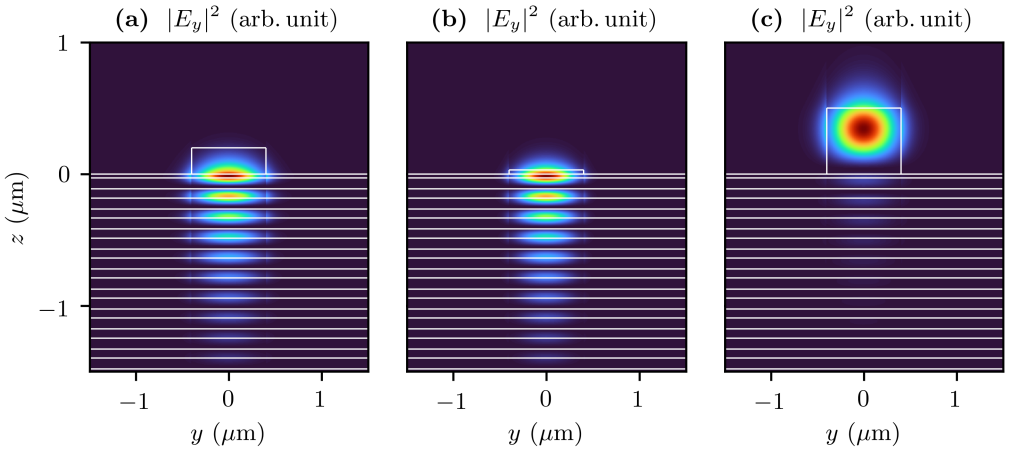

FIGURE 2.2. Intensity profile of (a) *good*, (b) *bad* and (c) *ugly* BSWs supported by the PhC ridges considered in [134]. The truncated multilayer is the same in the three cases, but is loaded with ridges of different thickness and refractive index. Note that in panel (c) the mode is confined by the PBG even though field oscillations in the multilayer are barely visible. Calculations are done via HEIM using an in-house implementation of the TMM. See the reference for details.

only because the ridge is shallow. In both cases, however, the modes originate from the unguided BSW supported by the bare multilayer as an effect of the dielectric perturbation. Finally, the *ugly* exists only for sufficiently thick ridges, with light being almost totally confined within the ridge. The dispersion relation is above the lightline of the ridge material. This mode does not originate from a perturbation of a BSW, and is reminiscent of guided modes in TIR-based rectangular waveguides, with higher-order modes appearing when the ridge thickness is increased. Notice that light is still confined by the PBG from the multilayer side.

A rigorous analytic treatment of PhC ridges is not possible, and various numerical algorithms such as RCWA, FDTD or finite element methods can be successfully utilized. To reduce the simulation complexity (memory and computation time) even further, the effective index method (EIM) is typically adopted. The basic concept of the EIM is the reduction of the 2D problem to two 1D problems that can be solved consecutively. Namely, one substitutes the ridge on top of the multilayer with an effective homogeneous layer of the same thickness t and refractive index $n_{\text{eff,slab}}$, calculated as the effective index of the fundamental mode supported by a symmetric air/ridge/air slab waveguide of width w (see Fig. 2.3(b)). The guided modes of the PhC ridge correspond to the guided modes supported by the resulting effective multilayer. We refer to this method as the *horizontal* EIM (HEIM).

In alternative, one can take a different approach. For sufficiently wide ridges, the strong confinement in the vertical direction over the lateral direction suggests that one should divide the cross section vertically into three different regions, namely the *bare*

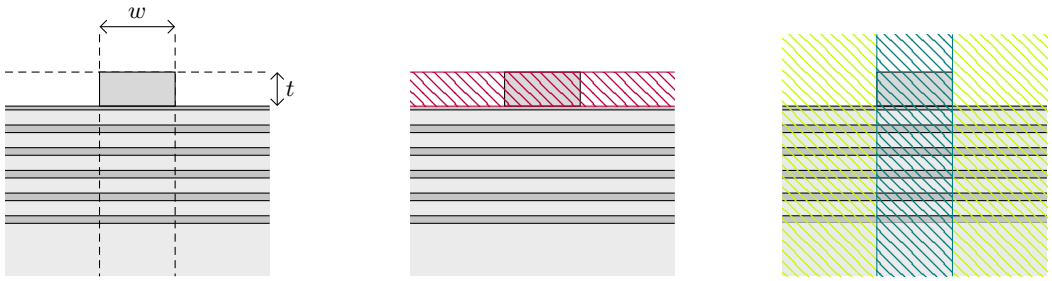

(a) PhC ridge (b) HEIM (c) VEIM

FIGURE 2.3. (a) Cross section of a PhC ridge of width w and thickness t. Illustration of the reduction of the problem dimensionality by using the (b) HEIM and (c) VEIM.

regions, corresponding to the 1D bare multilayer, and the *loaded* region, in which the 1D multilayer is loaded with an additional layer corresponding to the ridge. One can calculate the effective indices n_{bare} and n_{load} of the surface states supported by each region, and finally consider an effective slab waveguide of width w and refractive index n_{load} with cladding of refractive index n_{bare} (see Fig. 2.3(c)). The fundamental mode of this effective slab waveguide corresponds to the BSW guided by the PhC ridge. We refer to this second approach as the *vertical* EIM (VEIM). Obviously, the VEIM assumes that both bare and loaded regions support a 1D BSW, the loaded mode being indeed a perturbation of the bare one due to the presence of the additional dielectric layer. Therefore, using the nomenclature above, it cannot be applied to calculate the dispersion of *ugly* modes, which can be in fact determined using the HEIM only. As a rule of thumb, the VEIM is particularly indicated to describe those modes that are localized at the multilayer surface because of the strong vertical confinement of the field, while the HEIM is also suited to describe those modes that are strongly confined within the ridge.

The (often underemphasized) key assumption of effective index approaches is that the ridge modes are purely TE (TM) polarized. For instance, when dealing with TE (TM) ridge modes using the VEIM, one searches for the TE (TM) modes supported by the bare and loaded multilayers, and then for the TM (TE) fundamental mode supported by the effective bare/loaded/bare slab waveguide. Likewise, if one applies the HEIM, they search for the TM (TE) fundamental mode of the effective air/ridge/air slab waveguide, and then for the TE (TM) mode supported by the effective multilayer. However, as for any 2D dielectric waveguide, the ridge modes cannot be purely TE (TM) polarized because of the optical confinement being in both transverse directions. Therefore, the EIM fails to capture the hybrid nature of 2D guided modes, but is to some extent reliable, provided the dominant field component is TE (TM) polarized. We shall expand on this in the following section.

The goal of this dissertation is to demonstrate the potential integration of BSWs sustained by PhC ridges in on-chip devices. In particular, their peculiar mechanism of light confinement, based on the combination of TIR and PBG, allows one to operate with polymeric ridges, despite the relatively low refractive index contrast. The interest in using polymers is manifold [70]. They are already ubiquitous in nanotechnology, due to their relatively low cost, chemical stability, and mechanical robustness. Most importantly, they can be readily deposited and structured on the multilayer surface by simple lithographic techniques, such as electron beam lithography (EBL) [135] or direct laser writing (DLW) via two-photon polymerization (2PP) [136]. Although the small refractive index might be a limit to their light confinement abilities, on the other hand it can help reduce the scattering loss due to sidewall roughness and allow for higher fabrication tolerance. Next, their transparency window extends to visible wavelengths, which are not accessible with silicon photonics. Operating with visible light is of great interest in a large field of applications, from biochemical sensing and medical diagnostics to quantum information processing. In this respect, for example, polymers can be chemically functionalized for molecular recognition in biosensors [137], or can be doped with a wide range of nanoemitters, from organic dyes to quantum dots to color centers, which is appealing for on-chip integration of quantum light sources [138–142]. Finally, polymers can exhibit large second and third-order nonlinear optical properties [143].

Although this work is intended as a theoretical study, the feasibility of our ideas is validated numerically by considering structures whose features (geometry, dimensions, materials) are realistic and compatible with the actual fabrication. In particular, a titania (TiO_2)/silica (SiO_2) multilayer loaded with poly(methyl-methacrylate) (PMMA) and operating at visible wavelength $\lambda_0 = 532\,\text{nm}$ (corresponding to the second harmonic of a Nd:YAG laser) will be assumed as a de facto standard platform in this work.

2.2. Long-range BSWs in PhC ridges

Since their first experimental observation by Descrovi et al. [44], several works have focused on the control and manipulation of guided BSWs using dielectric loads on the multilayer surface to establish a complete integrated optical platform based on PhC ridges [45–52, 144–146]. Unfortunately, so far, experimental works have shown propagation loss of the order of dB/mm at best (see Table 2.1), which is one or two orders of magnitude larger than the typical loss reported in other integrated platforms (see Table 1.1). Propagation loss of the order of dB/cm is reported but for unguided BSWs [147]. This is not only frustrating, as it hinders the development of an integrated platform based on BSWs, but also unclear from a physical standpoint. Many authors claim that the use of lossless dielectric materials per se should guarantee

Structure	Material platform	λ (nm)	Propagation loss α (dB/cm)	Comments	Ref
Ultrathin ridge waveguide	a-SiN:H (multilayer) + AZ5214E photoresist (ridge)	1530	> 100		[44]
	SiO_2/Ta_2O_5 (multilayer) + PPST (ridge)	532	1042	Focusing planar lens for mode injection	[47]
	SiO_2/SiN (multilayer) + TiO_2 (ridge)	1553	350	Waveguide grating as a BSW reflector	[144]
Curved waveguides	SiO_2/SiN (multilayer) + AZ1518 photoresist (ridge)	1542	27 (straight), 178 (bend radius = 80 μm)		[45]
Ridge waveguide	SiO_2/SiN (multilayer) + SU-8 photoresist (ridge)	670	–	Two-photon laser lithography	[52]
	SiO_2/Ta_2O_5 (multilayer) + SU-8 photoresist (ridge)	670	–	Mach-Zender interferometer	[51]
Microdisk	SiO_2/SiN (multilayer) + TiO_2 (disk)	1550	~ 80 †	Q factor = 2,000, radius R = 100 μm	[48]
Microring	p-Si	1612	~ 25 †	Q factor = 4,000, radius R = 105 μm	[49]
Polymeric nanofibre	SiO_2/SiN (multilayer) + Nylon-6 (fiber)	633	8330	Nanofiber radius R = 125 nm	[145]

† Estimated from the Q factor under the assumption of critical coupling ($Q_{int} = 2Q$).

TABLE 2.1. Comparison of integrated waveguides supporting 2D BSWs.

long propagation lengths of BSWs, and take this strategic advantage for granted. In actual fact, FDTD simulations of idealized structures confirm that such high loss is not entirely due to fabrication imperfections [49], but it is intrinsically related to this very kind of light confinement relying on the combination of TIR and PBG.

Little research has been conducted on understanding the leading loss mechanisms. Earlier theoretical investigations on BSW dispersion and propagation rely on the use of approximated strategies, based mainly on EIMs [148]. As mentioned in the previous section, these approaches offer an advantage in terms of computational time and resources to calculating the dispersion relation and field distribution, and provide reliable results. At the same time, they are not able to capture all the physics of light propagation, especially for what concerns propagation loss. Here, by neglecting material absorption and scattering, we explain the physical mechanism behind the intrinsic loss of guided BSWs in PhC ridges and present a strategy to achieve significant improvement in the mode propagation length.

The structure under investigation is illustrated in Fig. 2.4. It consists of a dielectric ridge placed on the top of a truncated periodic multilayer. The multilayer has a finite number N of periods composed of two alternating layers of thicknesses d_a and d_b stacked along the z direction, with refractive indices n_a and $n_b < n_a$, respectively.

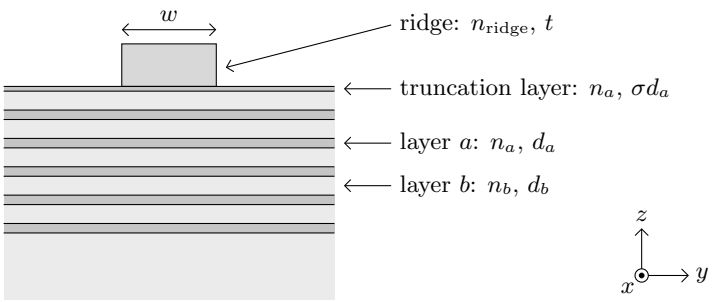

FIGURE 2.4. Sketch of the cross section of the PhC ridge.

The filling fraction $f = d_a/(d_a + d_b)$ determines the spectral position and extension of the (polarization-dependent) PBG with respect to the given refractive indices of the layers. The topmost n_a-index layer is truncated with thickness $d_\sigma = \sigma d_a$, with $\sigma \in (0, 1)$. On the top of the structure, a homogeneous dielectric ridge of width w, thickness t, and refractive index n_{ridge} sustains a guided BSW at a given operating wavelength λ_0 in vacuum. In SOI platforms, the waveguide dimensions are often preset by industry-standard wafers having a silicon thickness of 220 nm. Here, we require that the ridge width and thickness be of the same order of magnitude as λ_0 to ensure single-mode operation. Finally, we stress that we consider a very general case of PhC ridge, in which the guided BSW can be either a perturbation of the unguided BSW supported by the bare structure or not.

Due to the combination of TIR and reflection within the PBG, the guiding properties of the structure (number of modes, polarization dependence, dispersion profile, propagation loss, etc.) depend on both the ridge dimensions (for a given ridge material) and multilayer composition. It provides great freedom in terms of structure design, and yet sums up to a vast parameter space. It is worth reminding that the PBG is a bulk property of the sole multilayer, and its features depend only on its unit cell composition. The multilayer is the main focus here, for it is associated with the most complex confinement mechanisms and, as we shall see, its optimization is crucial to reducing the propagation loss.

Even in the presence of isotropic materials, the multilayer response at finite k_x depends on the light polarization. The PBG is intuitively understood to arise from the interference of the light reflected at each multilayer interface, whose amplitude depends on its polarization according to Fresnel's coefficients (see Appendix A.2). As a result of the mirror symmetry with respect to the xz plane and any other plane parallel to it, optical modes inside a 1D PhC can be labeled as either transverse electric (TE) or transverse magnetic (TM), with either $\mathbf{E}$ or $\mathbf{H}$ perpendicular to the xz plane. Consequently, one can classify eventual unguided 1D BSWs supported by

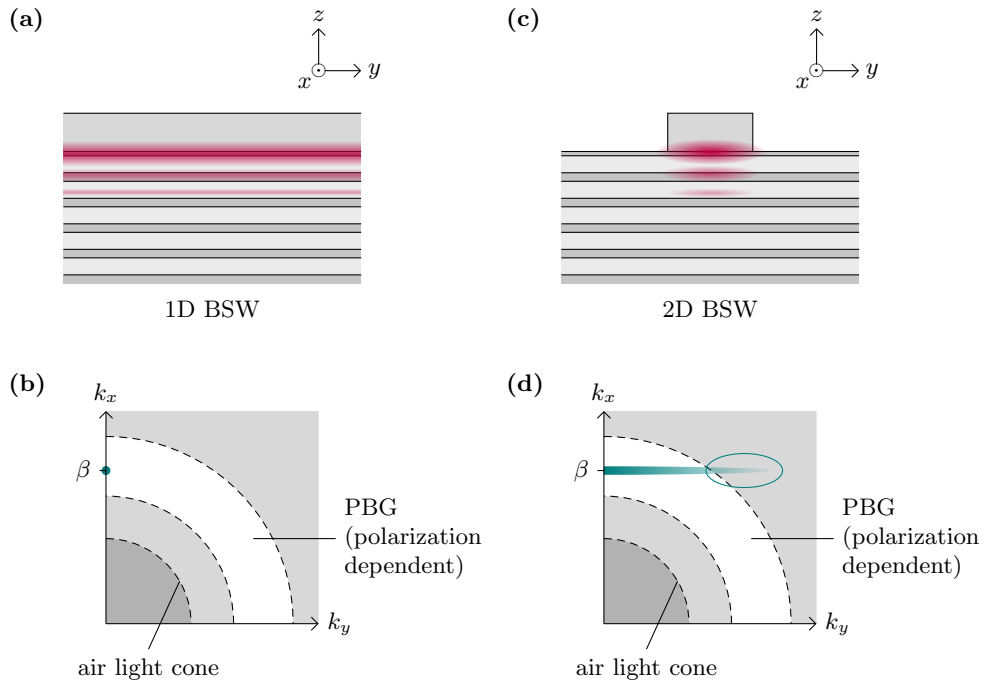

FIGURE 2.5. Pictorial representation of the field distribution and its Fourier spectrum in the (k_y, k_x) plane of the E_y component for (a), (b) TE BSW in a 1D structure and (c), (d) TE-like guided BSW in a PhC ridge.

a bare truncated multilayer as TE polarized, with only H_x, E_y, H_z nonvanishing field components, or TM polarized, with only E_x, H_y, E_z nonvanishing.

On the contrary, the guided mode propagating in the x direction along the ridge shown in Fig. 2.4 is characterized by the propagation constant $\beta = n_{\text{eff}} k_0$, with n_{eff} the effective mode index ($k_0 = 2\pi/\lambda_0$ is the free space wavevector), and by the electric and magnetic field profiles $\mathbf{E}(y, z)$ and $\mathbf{H}(y, z)$, which now are functions of both transverse spatial coordinates. Due to the finite width of the ridge, the structure is symmetric upon reflection with respect to the sole xz plane, i.e., at the center of the ridge ($y = 0$). In general, for $y \neq 0$, all six field components of any guided mode are nonvanishing. This can also be understood by considering that light confinement in the y direction implies $\partial/\partial y \neq 0$. Thus, a purely TE mode $\mathbf{E} = (0, E_y, 0)$ cannot be a solution to Maxwell's first equation $\nabla \cdot (n^2 \mathbf{E}) = 0$, with $n = n(y, z)$ the transverse refractive index profile. Indeed, from Maxwell's first equation one can show that a longitudinal electric field component E_x is always originated from the spatial gradient of the transverse field $\mathbf{E}_{\text{t}} = (E_y, E_z)$ [149]

$$E_x = \frac{\mathrm{i}}{\beta n^2} \nabla_{\text{t}} \cdot (n^2 \mathbf{E}_{\text{t}}), \tag{2.1}$$

where ∇_{t} denotes the transverse gradient. A stronger optical confinement in the transverse direction yields a larger longitudinal electric field component due to the

increasing spatial derivative. This is a major feature of any guided mode in a 2D waveguide. In silicon waveguides, for instance, the amplitude of the E_x component can be as high as 97% of that of the dominant transverse component $\mathbf{E}_\mathrm{t}$ [150]. In many cases, E_y (H_y) is the dominant field component, and the guided modes can be labeled as TE(TM)-like, despite preserving a nonzero longitudinal field component.

The hybrid polarization inherent in guided BSWs is of fundamental importance in addressing the origin of propagation loss. Indeed, while the condition of TIR is independent of light polarization (unless one deals with anisotropic media), in PhC ridges light confinement from the multilayer side is due to the PBG. Thus, the simultaneous presence of TE and TM PBGs around $k_x = \beta$ is always required to ensure that all six nonvanishing field components are guided.

A second important aspect is associated with the field distribution in the structure, which is connected to the Fourier components of the mode. In Fig. 2.5(a), we sketch the case of a purely 1D system, in which light is confined only along the z direction. At a given λ_0, the mode is characterized by a single point in the Fourier plane (k_y, k_x) (see Fig. 2.5(b)). On the contrary, in the case of a guided BSW, light confinement along the y direction (see Fig. 2.5(c)) determines a spread of the mode Fourier components along k_y (see Fig. 2.5(d)). The tighter the confinement, the larger the spread of the field Fourier components along k_y, with the risk of having a significant fraction of them outside the PBG, as pointed out in Fig. 2.5(d). In the latter case, light can couple to the radiation modes supported by the multilayer.

For a given wavelength λ_0 and a set of materials, one can design the structure on the basis of these two arguments to minimize the propagation loss. The idea is that, for a sufficiently large number of periods, longer propagation lengths require that all the field Fourier components be inside a PBG, so as to avoid leakage into the multilayer. In addition, since light is confined also by TIR, the Fourier components must be outside the cladding light cone to prevent coupling with the continuum of radiation modes in the cladding.

2.3. Simulation results and discussion

Following this approach, we consider the case of a PhC ridge realized on a TiO_2 ($n_a = 2.67$)/SiO_2 ($n_b = 1.46$) multilayer of $N = 10$ periods $\Lambda = d_a + d_b = 440\,\mathrm{nm}$. The topmost TiO_2 layer is truncated with thickness $d_\sigma = 10\,\mathrm{nm}$ and loaded with a PMMA ($n_\mathrm{ridge} = 1.49$) ridge of thickness $t = 0.4\,\mu\mathrm{m}$ and width $w = 1.0\,\mu\mathrm{m}$ to work in the visible spectrum at $\lambda_0 = 532\,\mathrm{nm}$. To restrict the number of possible configurations in the parameter space, we first let the filling fraction f be the only free parameter, with the TiO_2 and SiO_2 layers having thicknesses $d_a = f\Lambda$ and $d_b = (1-f)\Lambda$, respectively. For such a structure, in Fig. 2.6, we report the gapmap for both polarizations as

a function of the filling fraction f and the modulus $k_{\parallel} = \sqrt{k_x^2 + k_y^2}$ of the in-plane wavevector (k_x, k_y).

We can identify three different points A, B, and C that represent three qualitatively different situations given the ridge parameters indicated above. Point A corresponds to the case in which the PhC ridge is designed with a filling fraction $f_{\mathrm{A}} = 0.7$ and supports a TE-like BSW with a leading Fourier component at $k_{\parallel} = \beta_{\mathrm{A}} = 17.1\,\mu\mathrm{m}^{-1}$. In this case, one has a strong PBG for the TE components, but no gap for the TM components. Point B, at $f_{\mathrm{B}} = 0.45$ and $\beta_{\mathrm{B}} = 17.4\,\mu\mathrm{m}^{-1}$, represents the intermediate situation of a strong TE PBG overlapping with a moderately wide TM PBG. Finally, point C, at $f_{\mathrm{C}} = 0.22$ and $k_{\parallel} = \beta_{\mathrm{C}} = 17.5\,\mu\mathrm{m}^{-1}$, corresponds to the most favorable case in which both TE and TM PBGs are wide and well-overlapping.

Following the argument presented in Fig. 2.5, we calculate the Fourier transform (FT) of each field component as a function of $k_{\parallel}$ for the guided modes supported by the PhC ridges A, B, and C. This can be obtained from the electric field profile $\mathbf{E}(y, z)$ of the modes, which are calculated by means of Ansys/Lumerical 2D finite difference eigenmode (FDE) solver with perfectly matched layer (PML) boundary conditions. It should be noticed that, in general, $\mathbf{E}(y, z)$ is not separable as a product of two functions in the y and z coordinates separately, thus also the FT is not separable in k_y and k_z. This means that, for a proper analysis, one has to consider the FT distribution as a function of both $k_{\parallel}$ and k_z, as plotted in Figs. 2.7, 2.8, and 2.9.

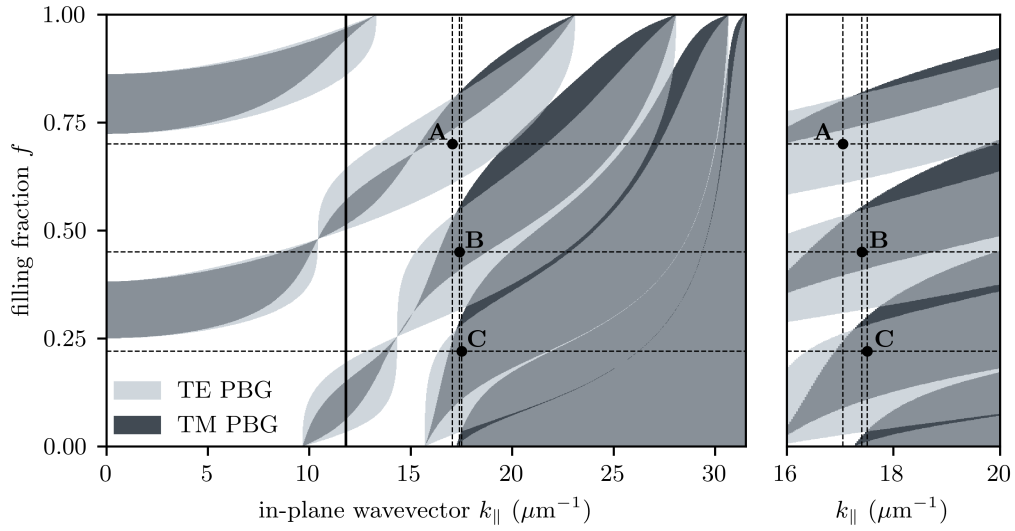

FIGURE 2.6. Gapmap at $\lambda_0 = 532\,\mathrm{nm}$ for the present TiO_2/SiO_2 multilayer of period $\Lambda = 440\,\mathrm{nm}$ as a function of the filling fraction f and the in-plane wavevector $k_{\parallel}$. The TE (TM) PBG is represented by the light (dark) area. The three investigated cases (dashed lines) and the air lightline (solid) are pointed out.

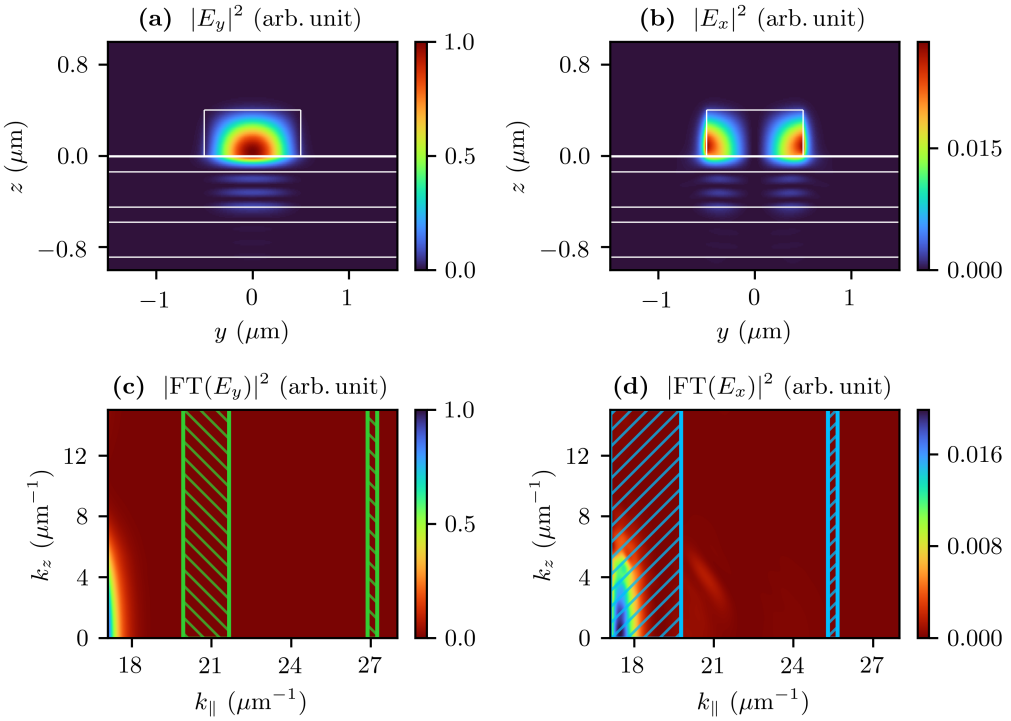

FIGURE 2.7. Intensity profiles (normalized to the maximum value) of (a) E_y and (b) E_x for the structure corresponding to case A, along with the FT spectrum of (c) E_y and (d) E_x. The dashed areas correspond to regions where the (c) (green) TE and (d) (cyan) TM PBGs are closed.

We start by considering the case $f_\mathrm{A} = 0.7$ (working point A of Fig. 2.6) for which $\beta_\mathrm{A} = 17.1\,\mu\mathrm{m}^{-1}$. The intensity profiles and Fourier spectra as a function of $k_\parallel$ and k_z for the two field components E_y and E_x are shown in Fig. 2.7. The results for E_z are not shown because its field intensity is sufficiently small to be neglected. In each graph, the dashed regions correspond to values of $k_\parallel$ for which the PBG for the relevant polarization is closed, and light is not guided. We observe that, while almost the entire FT for E_y is within a PBG, this is not so for E_x, for which most of the light cannot be confined on the multilayer side. This is confirmed by the relatively large propagation loss $\alpha_\mathrm{A} = 50.0\,\mathrm{dB/cm}$, as calculated from the imaginary part of the complex effective index: $\alpha\,(\mathrm{dB/cm}) = 8.68 \cdot (2\pi n_\mathrm{im}/\lambda_0\,(\mathrm{cm}))$.

A similar analysis can be done for the structure $f_\mathrm{B} = 0.45$ (working point B of Fig. 2.5), for which there exist TE and TM PBGs around the working point. In this case, the Fourier analysis (Fig. 2.8) unveils that a significant fraction of the Fourier components is within the TE and TM PBGs around $\beta_\mathrm{B} = 17.4\,\mu\mathrm{m}^{-1}$. The previous example suggests that, in this case, lower propagation loss should be expected. Indeed, the computed value is $\alpha_\mathrm{B} = 1.03\,\mathrm{dB/cm}$. This improvement is of more than one order of magnitude and indicates that a further optimization of the PBG position to confine the TM fraction of the mode could lead to better results.

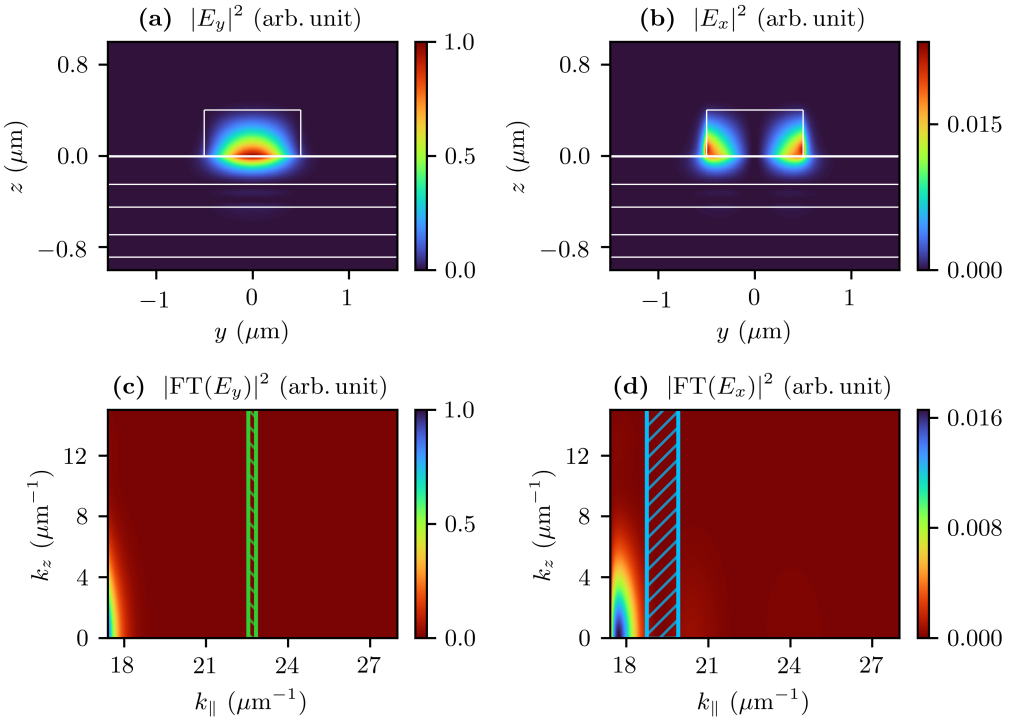

FIGURE 2.8. Intensity profiles (normalized to the maximum value) of (a) E_y and (b) E_x for the structure corresponding to case B, along with the FT spectrum of (c) E_y and (d) E_x. The dashed areas correspond to regions where the (c) (green) TE and (d) (cyan) TM PBGs are closed.

With this in mind, we now turn to the case $f_C = 0.22$ (working point C of Fig. 2.5). This point represents a favorable situation of wide and well-overlapping TE and TM PBGs. In this case, the computed propagation loss is $\alpha_C = 5.67 \times 10^{-5}$ dB/cm, six orders of magnitude lower than that of case A. The origin of such a noteworthy improvement is clear by looking at Fig. 2.9, where we show the Fourier analysis along with the electric field intensity profiles for the two dominant field components. In this case, almost all the field FTs are within the PBG regions for both polarizations. All the results are summarized in Tab. 2.2. We also report the mode effective areas as calculated by Eqs. (1.11) and (1.12). In the latter, we assume the ridge as the region with nonlinear optical (NLO) properties. PMMA by itself does not have significant NLO properties, but is a suitable host material for other highly NLO guest materials (although the linear refractive index may change significantly on account of the guest material concentration). However, in the present case, the field distribution is not always optimal to enhance possible nonlinear effects, for one would rather operate with *ugly* modes, in which light is mainly confined inside the NLO ridge itself, than *good* modes, in which light is mostly confined near the truncation surface. We expand on this point in Chapter 5.

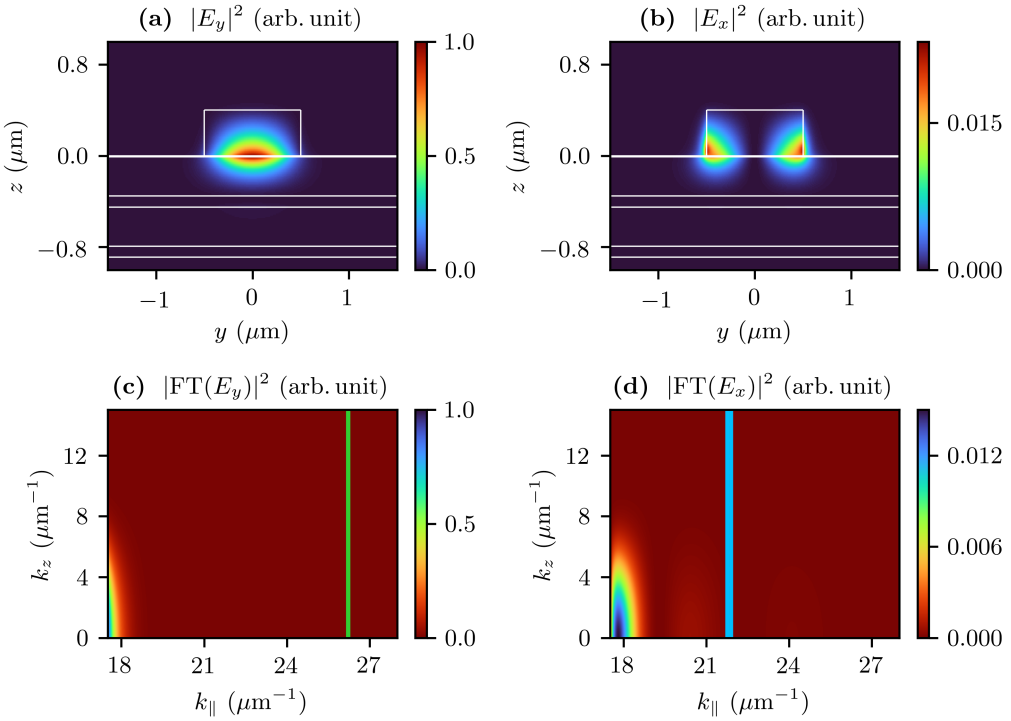

FIGURE 2.9. Intensity profiles (normalized to the maximum value) of (a) E_y and (b) E_x for the structure corresponding to case C, along with the FT spectrum of (c) E_y and (d) E_x. The dashed areas correspond to regions where the (c) (green) TE and (d) (cyan) TM PBGs are closed.

We stress that, in the discussion above, we always considered the situation in which the number N of multilayer periods is sufficiently large so that the confinement is essentially perfect in the whole region defined by the PBG of the corresponding infinite multilayer. For the best structure considered here, $N = 10$ is sufficient to obtain propagation loss that is equivalent to the case of an infinite number of periods. Indeed, in that case, the mode Fourier components are localized well within the PBGs and far from the photonic band edges (BEs) (see Fig. 2.9). However, care should be taken when the Fourier components are nonvanishing near the BEs, for a

Case	f	w (μm)	n_{eff}	α (dB/cm)	A_{eff} (μm^2)	$A_{eff,nl}$ (μm^2)
A	0.70	1.0	1.444	50.0	0.355	0.413
B	0.45	1.0	1.474	1.03	0.336	0.517
C	0.22	1.0	1.483	5.67×10^{-5}	0.365	0.640
		1.2	1.487	5.48×10^{-3}	0.418	0.727

TABLE 2.2. Results for the cases A, B, and C described in this section, with f the multilayer filling fraction, w the ridge width, n_{eff} the mode effective index, α the mode propagation loss, A_{eff} the mode effective area calculated with (1.11), and $A_{\mathrm{eff,nl}}$ the mode effective area calculated with (1.12) assuming the ridge as the NLO region.

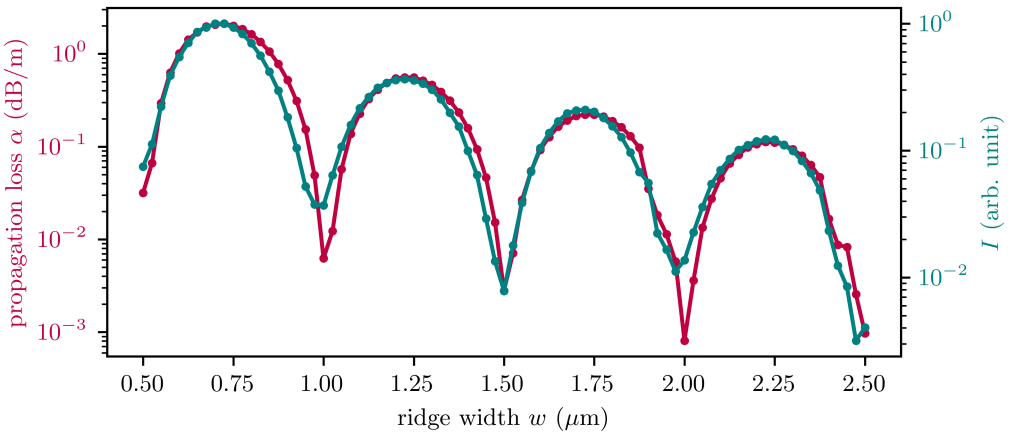

FIGURE 2.10. Propagation loss α (left axis) (red) and figure of merit I defined in Eq. (2.2) (right axis) (green) as a function of the ridge width w for the structure C, plotted in logarithmic scale.

considerably large number of periods could be required to achieve strong attenuation in the multilayer.

So far, we focused on the multilayer parameters that control the position and extension of the PBGs. However, one can also modify the FT distribution of the guided BSW by varying the ridge width w. This gives an additional tuning parameter that can be particularly useful in practice, when the multilayer is already fabricated and one wants to improve the propagation lengths even further. In the limit of wide ridges, propagation loss is expected to decrease, for the mode is more localized in the Fourier space and its polarization tends to become purely TE or TM. In the more interesting situation of tight confinement, when the ridge width is of the order of the operating wavelength, the FT distribution with respect to the PBGs is no longer intuitive, and a slight increase in the ridge width can lead also to a counterintuitive increase in the propagation loss. This is illustrated in Fig. 2.10 (left axis), where the ridge width in the structure C is varied from 0.5 µm to 2.5 µm with a 25 nm increment. For instance, by increasing the ridge width from $w = 1.0\,\mu\text{m}$ to $w = 1.2\,\mu\text{m}$, the propagation loss increases by almost two orders of magnitude (see Tab. 2.2).

To measure the effectiveness of our argument, we compare the intrinsic propagation loss with the fraction of leaky Fourier components. This is done in Fig. 2.10. Namely, in an attempt to include also the effect of a finite number N of multilayer periods (i.e., imperfect guiding in the PBG window due to finite mirror strength), we introduce the quantity

$$\begin{aligned} I = &\int |\mathrm{FT}(E_y)|^2 \mathrm{e}^{-2\,\mathrm{Im}(q_{\mathrm{TE}})N\Lambda}\,\mathrm{d}k_\parallel\,\mathrm{d}k_y \\ &+ \int \Big(|\mathrm{FT}(E_x)|^2 + |\mathrm{FT}(E_z)|^2\Big)\mathrm{e}^{-2\,\mathrm{Im}(q_{\mathrm{TM}})N\Lambda}\,\mathrm{d}k_\parallel\,\mathrm{d}k_y, \end{aligned} \tag{2.2}$$

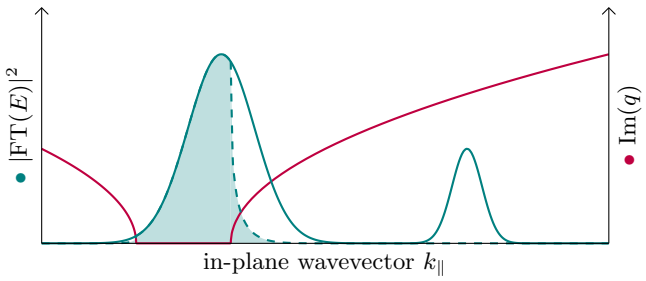

FIGURE 2.11. Illustration of the fraction of leaky Fourier components as expressed in Eq. (2.2) for a generic electric field component E and given k_z as a function of the in-plane wavevector $k_\parallel$. The function being integrated in Eq. (2.2) (dashed green) is the product of the Fourier spectrum of E (solid green) and an exponential factor $\mathrm{e}^{-2\,\mathrm{Im}(q)N\Lambda}$, with $\mathrm{Im}(q)$ being the imaginary part of the Bloch wavevector for the corresponding polarization (solid red). The intrinsic loss is approximately proportional to this integral (shaded area).

where the integrals extend over the whole wavevector space $(k_\parallel, k_y)$. The exponential factor $\mathrm{e}^{-2\,\mathrm{Im}(q)N\Lambda}$, with q being the Bloch wavevector for the relevant polarization, fully accounts for the Fourier components inside the leaky region ($\mathrm{Im}(q) = 0$), but also assigns different weights to the Fourier components inside the guiding region depending on the magnitude of $\mathrm{Im}(q) > 0$. This is illustrated in Fig. 2.11. Notice that the Fourier components in close proximity to the photonic BEs might be weakly guided due to the poor mirror strength, adding to the integral in (2.2). Fig. 2.10 clearly shows the same trend of α (left axis) and I (right axis) as functions of w, confirming the reliability of our approach.

In conclusion, we showed that the optimization of the PBGs for both light polarizations is essential to achieve long-range guided BSWs in PhC ridges. The propagation length can be improved by engineering the structure so that the field Fourier components for both polarizations are outside the cladding light cone and inside the corresponding PBG. We illustrated that this can be achieved by a proper design of the multilayer by choosing its period and filling fraction to adjust the PBG position and extension in the Fourier space. Our results clarify the nature of BSW propagation in PhC ridges and extend the possibilities of BSW-based integrated platforms for on-chip light control.

CHAPTER 3

Confining BSWs: BSW-based nanobeam cavities

3.1. BSW-based microresonators

As seen in previous chapters, the possibility of guiding BSWs by simply realizing a polymeric ridge waveguide makes them appealing for the development of an etchless, all-dielectric integrated photonic platform operating also at visible wavelengths. To this end, microresonators constitute an indispensable building block. Recently, Menotti et al. suggested that full 3D confinement of BSWs could be readily achieved by bending the ridge on itself to obtain high-Q ring resonators [148]. The authors outlined a very general design strategy based on the separation of the vertical and in-plane structure, and adopted a combination of EIM and 2D FDTD calculations to predict Q factors exceeding 10^7 at visible wavelengths. However, this approach neglects the polarization-related shortcomings inherent to EIMs. Dubey et al. first demonstrated a BSW-based microdisk resonator using a TiO_2 disk of radius $R = 100\,\mu m$ on top of a truncated SiO_2/SiN multilayer, with a reported $Q = 2000$ around 1550 nm [48]. Later, Rodriguez et al. fabricated a BSW-based microring resonator of radius $R = 105\,\mu m$ on a p-Si multilayer, with Q factors exceeding 10^3 at telecom wavelengths [49]. These values are below par as compared to typical microrings (see Table 1.2). Still, the authors believe that Q factors as high as 10^4 could be obtained with further optimization of the structure parameters.

It is known that WGM resonators can lead to relatively high Q factors, yet at the price of large mode volumes V owing to the large bend radii allowed by the gentle light confinement in the plane. It can be undesirable in many applications involving, for instance, spontaneous emission or strong coupling, for which the figure of merit is proportional to the Q/V ratio. Therefore, standing-wave optical resonators, characterized by small V, even smaller than a cubic wavelength of light, have been explored as an attractive alternative. Vosoughi Lahijani et al. fabricated a subwavelength Fabry-Pérot cavity exhibiting a Q factor of about 400 (at 633 nm) using ZEP (a positive e-beam resist) on top of a SiO_2/SiN multilayer [151]. Stella et al. designed a circular Fabry-Pérot cavity using dye-doped PMMA on top of a Ta_2O_5/SiO_2 multilayer. The structure also provided an external diffractive grating for light outcoupling. They experimentally observed Q factors of the order of 10^3 (at 570 nm), with a predicted mode volume $V = 2.23(\lambda/n)^3$ [152].

Structure	Material platform	λ (nm)	Q factor	Comments	Ref
Microdisk	SiO_2/SiN (multilayer) + TiO_2 (disk)	1550 nm	2,000 (20,000†)	radius = 100 μm	[48]
Microring	p-Si	1612 nm	4,000	radius = 105 μm	[49]
Fabry-Pérot cavity	SiO_2/SiN (multilayer) + ZEP (DBRs)	633 nm	400	subwavelength cavity length (L_c = 252 nm)	[151]
Circular Fabry-Pérot cavity	Ta_2O_5/SiO_2 (multilayer) + dye-doped PMMA (concentric rings)	570 nm	∼ 1,000 (1,440†)	mode V = 2.23(λ/n)^3	[152]

† Theoretical value.

TABLE 3.1. Comparison of BSW-based microresonators.

A different approach is that of photonic crystal nanobeam cavities (PhCNCs). They can be fabricated in a PhC ridge waveguide by directly patterning the ridge to create a cavity region surrounded by Bragg mirrors on each side. This leads to a structure in which light is confined by a PBG from the multilayer side and in the longitudinal direction of the nanobeam, and by TIR in all the other directions, in a combination that, to the best of our knowledge, has never been proposed before. In this chapter, we theoretically demonstrate the concept of a BSW-based PhCNC. Our design is essentially borrowed from Noda group's study of optimal field distribution in photonic double heterostructures [107], and it is optimized within the framework of Fourier space analysis. In addition, in order to limit the computational resources required for the numerical treatment of a 3D structure, the design is carried out by means of an effective index approach, which allows one to reduce the dimensionality of the problem.

3.2. BSW-based photonic crystal nanobeam cavity

We consider BSWs supported by a PhC ridge waveguide, as sketched in Fig. 3.1(a). The multilayer has a finite number N of periods composed of two alternating layers of thicknesses d_a and d_b, and refractive indices n_a and n_b, respectively. The filling fraction $f = d_a/(d_a + d_b)$ determines the spectral position and the extension of the PBG with respect to the given refractive indices of the layers. The multilayer termination is defined by a truncation layer of thickness $d_\sigma = \sigma d_a$, with $\sigma \in (0, 1)$, and refractive index n_a. On top of the multilayer, we consider a dielectric ridge of width w, thickness t, and refractive index n_{ridge}. The surrounding cladding is assumed to be air ($n_{\text{clad}} = 1$). The structure is designed to operate at a wavelength λ_0 (frequency ω_0) in vacuum. Without loss of generality, we consider a TE-like mode with E_y as the dominant field component.

The cavity is formed by patterning two Bragg mirrors into the ridge, each including N_{Bragg} periodically spaced rectangular stacks, in the fashion of a row of dominoes,

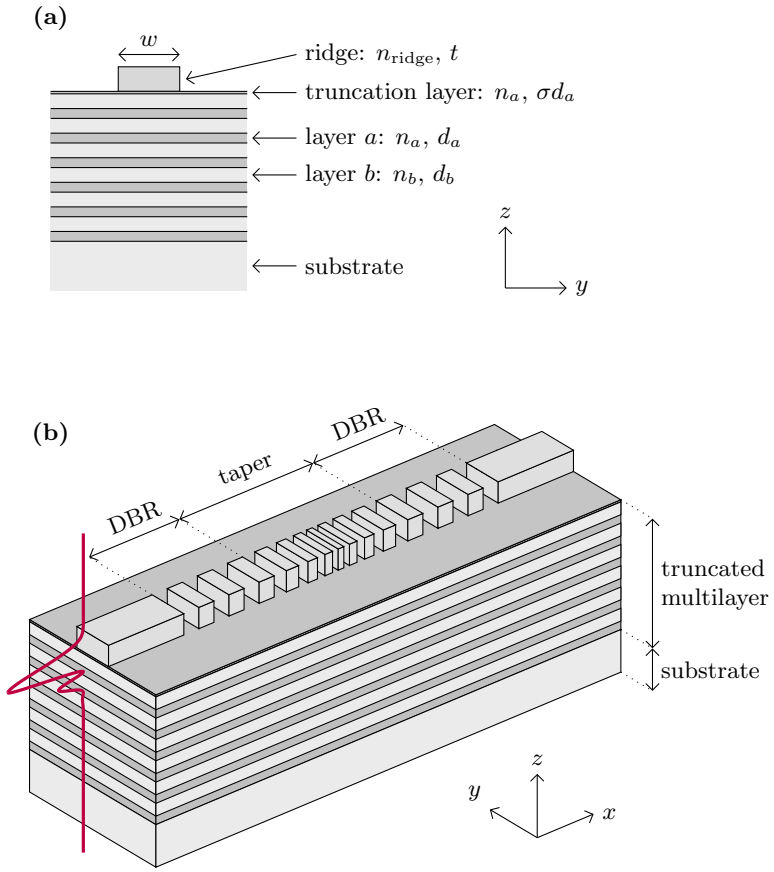

FIGURE 3.1. (a) Sketch of the cross section of the PhC ridge under study. (b) Sketch of the BSW-based PhCNC.

as shown in Fig. 3.1(b). The unit cell has a lattice constant $\Lambda_{\text{Bragg}} = s_{\text{Bragg}} + g_{\text{Bragg}}$, in which s_{Bragg} and g_{Bragg} are the thicknesses of the ridge stacks and air slits, respectively. The filling fraction is $f_{\text{Bragg}} = s_{\text{Bragg}}/\Lambda_{\text{Bragg}}$. This geometry greatly simplifies the fabrication procedure, which can be done by standard lithography. In addition, the system can be modeled within an effective index (EI) framework to reduce the dimensionality of the problem and limit the computational cost of its optimization, which usually requires to investigate a large parameter space.

Here, the EI method is applied twice. First, we determine the effective index of the guided BSW supported by the ridge (n_{eff}) by modeling its cross section as an effective slab waveguide, where the cladding and core refractive indices are those of the modes supported by the 1D bare (n_{bare}) and ridge-loaded (n_{load}) multilayers, respectively (VEIM, as described in Chapter 2). Second, the in-plane cavity is treated as an effective 1D multilayer of alternating layers of indices $n_1 = n_{\text{eff}}$ and $n_2 = n_{\text{bare}}$ for each ridge stack and air slit, respectively. In other words, we replace each ridge stack and air slit with a uniform layer having a refractive index corresponding to that

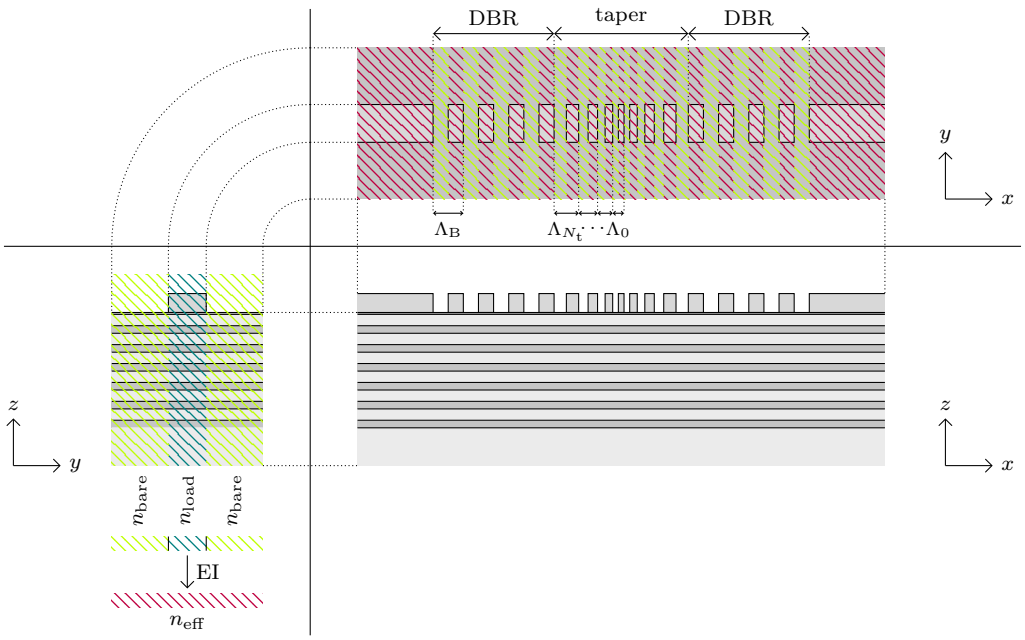

FIGURE 3.2. Illustration of the effective index approach for the PhCNC under investigation.

of the pertaining confined mode. This is illustrated in Fig. 3.2. All these tasks are easily solved via the transfer matrix method (TMM), which can take only minutes, if not seconds, on a standard personal computer. The EI approximation assumes the mode field to be factorized in the three spatial directions. Hence, the overall 3D mode profile can be obtained by combining the 1D mode profiles of the bare and loaded BSWs (which give the field distribution in the z direction), the 1D mode profile of the effective slab waveguide (which gives the field distribution in the y direction), and the 1D mode profile of the effective in-plane multilayer (which gives the field distribution in the x direction).

In our design, the Bragg mirrors are chosen as conventional quarter-wave stack, i.e., $\Lambda_{\text{Bragg}} = (\lambda_0/4)(1/n_1 + 1/n_2)$ and $f_{\text{Bragg}} = n_2/(n_1 + n_2)$, where $n_1 = n_{\text{eff}}$ and $n_2 = n_{\text{bare}}$ are the effective indices defined above. The mirrors are tapered by gradually resizing a number N_{taper} of stacks toward the cavity center. Tapering the Bragg mirrors is crucial to optimize the Q factor of the cavity mode. If we neglect material absorption and scattering from fabrication imperfections, the leading loss mechanisms are light leakage through the finite-sized Bragg mirrors in the x direction (with decay rate γ_{Bragg}) and light coupling to the radiation modes out of the nanobeam in the other directions (with decay rate γ_{rad}). The total Q factor is given by

$$\frac{1}{Q} = \frac{1}{Q_{\text{Bragg}}} + \frac{1}{Q_{\text{rad}}}, \tag{3.1}$$

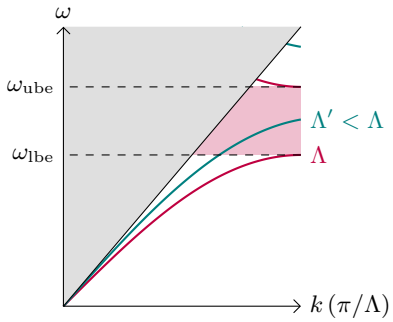

FIGURE 3.3. Band diagram for a PhC with lattice constant Λ (red) and another PhC with reduced lattice constant $\Lambda' < \Lambda$ (green). When the lower bandedge of the PhC with lattice constant Λ' lies inside the PBG of the PhC with lattice constant Λ (red shaded area), it serves as a defect mode. The gray shaded area indicates the cladding material lightcone.

where $Q_{\text{Bragg}} = \omega_0/\gamma_{\text{Bragg}}$ and $Q_{\text{rad}} = \omega_0/\gamma_{\text{rad}}$, respectively. In principle, Q_{Bragg} can be made arbitrarily high by increasing N_{Bragg}. Therefore, the total Q is limited by Q_{rad}. Coupling to the radiation modes arises from the Fourier components of the cavity mode that (i) lie inside the air lightcone, and thus violate the TIR condition, or (ii) lie outside the PBG of the underlying multilayer. Regions (i)+(ii) constitute the so-called *leaky region*. Therefore, a simple rule to achieve a high Q factor of the cavity mode is to minimize the fraction of Fourier components within the leaky region [153, 154].

Here is where the taper comes into play. By means of a "gentle" modification of the cavity geometry, the optical field in the real domain can be altered in such a way that its distribution in the Fourier domain is well-localized outside the leaky region. We remark that light polarization plays an essential role in determining the extension of the leaky region. As discussed in Chapter 2, due to the confinement in the lateral direction, the mode supported by the PhC ridge is not purely TE polarized, but TE-like polarized, in that it exhibits all six nonvanishing field components, with E_y being the dominant one and E_x, E_z being weak but nonzero. Hence, the simultaneous presence of both TE and TM PBGs is always required to have each field component's Fourier distribution well-located within the appropriate PBG. A careful choice of the PhC ridge geometry can ensure wide and well-overlapping TE and TM PBGs in the spectral region of interest.

We are interested in a dielectric-mode nanobeam, in which most of the optical energy is concentrated in the high-refractive-index cavity material. In the present case, a "gentle confinement" can be achieved by gradually reducing the lattice constant of the mirror segments toward the cavity center. It results in a blueshift of the PBG, so that the segment with a reduced lattice constant $\Lambda' < \Lambda$ has the lower bandedge lying within the PBG of the segment with lattice constant Λ (Fig. 3.3). It acts as a defect mode in the PhC with lattice constant Λ, which serves, in turn, as a Bragg mirror.

In other words, the decrease in lattice constant gives rise to an optical potential well for the dielectric mode, which is pulled from the dielectric band within the PBG. On a side note, we remark that an air-mode nanobeam can also be designed using the same principle. In this case, by progressively increasing the lattice constant of the mirror segments, the air mode moves inside the PBG from the air band.

In the next paragraph, we show that a Gaussian field envelope ensures a very gentle confinement and we obtain a simple geometric rule to achieve it in our structure. Our results are comparable with similar design strategies proposed to analogous PhCNCs [155]. Incidentally, we notice that other approaches are also possible, e.g., modulating the ridge width w, and have been promisingly tested in the trial design but have not been investigated any further in this dissertation. Moreover, different solutions might be combined simultaneously, but at the cost of introducing additional degrees of freedom.

In-plane optimization. The essence of our optimization strategy is tapering the cavity Bragg mirrors so that we can minimize the fraction of Fourier components inside the leaky region. We follow the argument in [107]. In the case of quarter-wave Bragg mirrors with lattice constant $\Lambda = (\lambda_0/4)(1/n_1 + 1/n_2)$ and filling fraction $f = n_2/(n_1 + n_2)$ (here we temporarily drop the subscript for ease of reading), the Bloch wavevector within the PBG is a complex quantity:

$$q = \frac{\pi}{\Lambda} + \mathrm{i}\gamma, \tag{3.2}$$

where the attenuation constant (or mirror strength) at the center of the PBG is, according to Eq. (1.5), $\gamma = \Delta n/(n\Lambda)$, with $\Delta n = |n_1 - n_2|$ the refractive index contrast and $n = (n_1 + n_2)/2$ the average refractive index. Thus, the electric field in the reflector region decays exponentially with

$$E_y(x) \propto \cos\Big(\frac{\pi}{\Lambda}x\Big)\exp(-\gamma x). \tag{3.3}$$

When two Bragg mirrors are placed back to back to form a FP cavity with length L (Fig. 3.4(a1)), the electric field can be expressed as a sinusoidal wave modulated by an envelope function that is determined by the cavity geometry (Fig. 3.4(a2)):

$$\begin{aligned} E_y(x) \propto & \cos\Big(\frac{\pi}{\Lambda}x\Big)\mathrm{rect}\Big(\frac{x}{L}\Big) + \\ & \cos\Big(\frac{\pi}{\Lambda}x\Big)\Big[1 - \mathrm{rect}\Big(\frac{x}{L}\Big)\Big]\exp\Big[-\gamma\Big(|x| - \frac{L}{2}\Big)\Big], \end{aligned} \tag{3.4}$$

where $\mathrm{rect}(x)$ is the rectangular function. The Fourier transform of (3.4) is shown in Fig. 3.4(a3). The sinusoidal wave gives a delta distribution peaked at $k_x = \pm\pi/\Lambda$, while the envelope function modifies the spectrum. The more abrupt the change of slope in the envelope function at the cavity edges, the larger the Fourier components inside the leaky region.

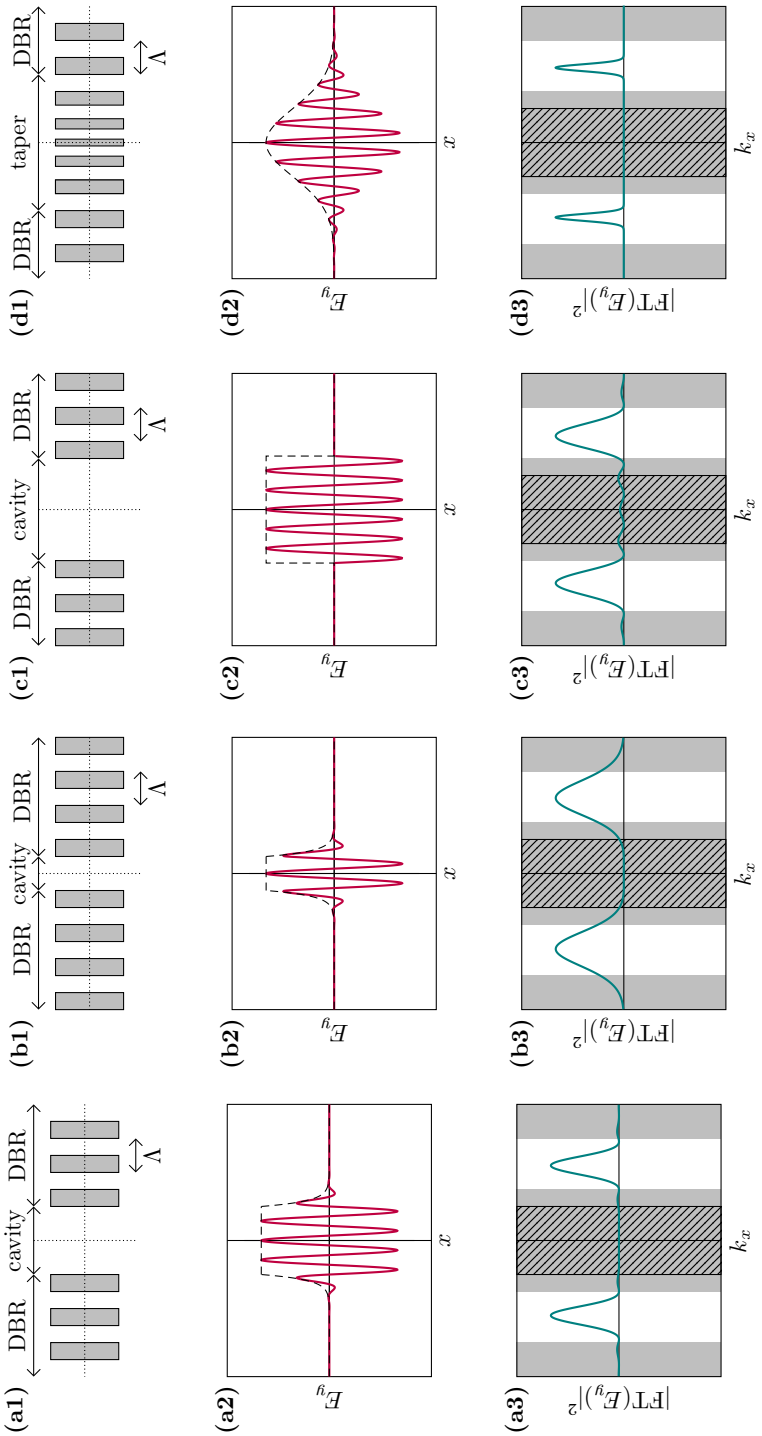

FIGURE 3.4. Analysis of cavity loss for different geometries: (a) FP cavity; (b) FP cavity with very short cavity length; (c) FP cavity with perfect Bragg mirrors; (d) cavity with tapered mirrors. For each geometry, insets show (1) a sketch of the cavity, (2) the electric field profile, and (3) the spatial Fourier spectrum. The shaded area indicates the leaky region. The patterned area indicates the air lightcone.

It is instructive to consider the Fourier distribution of the cavity field in the limiting cases of (i) very short cavity ($L \ll \lambda_0$, Figs. 3.4(b1),(b2)) and (ii) perfect mirrors ($\gamma \to \infty$, Figs. 3.4(c1),(c2)). In the case (i), the Fourier transform involves the convolution of a delta distribution with a Lorentzian function (Fig. 3.4(b3)):

$$\mathrm{FT}(E_y)(k_x) \propto \frac{1}{(k_x - \pi/\Lambda)^2 + \gamma^2} + \frac{1}{(k_x + \pi/\Lambda)^2 + \gamma^2}, \tag{3.5}$$

with a spectral width Δk_x in the vicinity of $k_x = \pi/\Lambda$ of the order of the attenuation constant γ. In the case (ii), the Fourier transform is the convolution of a delta distribution with a sinc function (Fig. 3.4(c3)):

$$\mathrm{FT}(E_y)(k_x) \propto \mathrm{sinc}\Big(\frac{L}{2}\Big(k_x - \frac{\pi}{\Lambda}\Big)\Big) + \mathrm{sinc}\Big(\frac{L}{2}\Big(k_x + \frac{\pi}{\Lambda}\Big)\Big). \tag{3.6}$$

Away from the peaks at $k = \pm\pi/\Lambda$, the spectrum decreases $\propto 1/||k_x| - \pi/\Lambda|$ but revives at every local extremum. In both cases, appreciable components are pulled within the leaky region.

In order to localize more tightly the Fourier components away from the leaky region, we would rather have a Gaussian envelope, which ensures a "gentle confinement" of the field at the cavity edges. Indeed, if the field is modulated by a Gaussian function with variance σ (Fig. 3.4(d2)),

$$E_y(x) \propto \cos\Big(\frac{\pi}{\Lambda}x\Big)\exp\Big(-\frac{1}{2}\frac{x^2}{\sigma^2}\Big), \tag{3.7}$$

its Fourier transform is the convolution of a delta distribution with another Gaussian function (Fig. 3.4(d3)),

$$\mathrm{FT}(E_y)(k_x) \propto \exp\Big[-\frac{\sigma^2}{2}\Big(k_x - \frac{\pi}{\Lambda}\Big)^2\Big] + \exp\Big[-\frac{\sigma^2}{2}\Big(k_x + \frac{\pi}{\Lambda}\Big)^2\Big]. \tag{3.8}$$

The spectral width Δk_x around each peak $k_x = \pm\pi/\Lambda$ is of the order of $1/\sigma$ and can be tuned by adjusting the width σ of the Gaussian envelope in the real domain. In particular, the modal distribution in the Fourier domain can be narrowed around $k_x = \pm\pi/\Lambda$ by increasing σ, hence minimizing the Fourier components in the leaky region. This maximises Q, yet at the cost of a slight increase in the mode volume V.

From Eqs. (3.3) and (3.7), it becomes clear that the exponentially-attenuated field in the reflector region can be modulated to a Gaussian profile by making the attenuation constant γ a linear function of the spatial coordinate x, i.e.,

$$\gamma = \frac{x}{2\sigma^2}. \tag{3.9}$$

This can be achieved by reducing the lattice constant Λ of each taper section toward the cavity center (Fig. 3.4(d1)). Such a modification leads to a blueshift of the lower-bandedge frequencies toward the cavity center, thus forming an optical potential well. The complex dispersion relation within the PBG can be found by analytic

continuation, i.e., by expanding the real dispersion relation into its complex form via a Taylor expansion at the bandedge ($k = \pi/\Lambda$). Due to the even symmetry of the dispersion relation around this point, only even powers of $(k_x - \pi/\Lambda)$ appear in the expansion. Up to second order, we have for the dielectric band:

$$\omega = \omega(\pi/\Lambda) + c_1(k_x - \pi/\Lambda)^2, \tag{3.10}$$

where $c_1 < 0$ due to its negative curvature. Substitution of $k_x = \pi/\Lambda + \mathrm{i}\gamma$ gives the dispersion in the bandgap as a function of γ:

$$\omega = \omega^{\mathrm{lbe}} - c_1\gamma^2, \tag{3.11}$$

where $\omega^{\mathrm{lbe}} = \omega(\pi/\Lambda)$ is the lower-bandedge frequency. Plugging (3.9) into (3.11) and rearranging the terms yields the required distribution of the lower-bandedge frequency along the x direction at a given operating frequency ω:

$$\omega^{\mathrm{lbe}}(x) = \omega + c_1\Big(\frac{x}{2\sigma^2}\Big)^2 = \omega(1 - \alpha x^2), \tag{3.12}$$

where $\alpha = -c_1/(4\sigma^4\omega)$ is a positive constant ($c_1 < 0$). The frequency is inversely proportional to the lattice constant Λ. With respect to the cavity center (subscript 0), the lower bandedge can be shifted by adjusting the lattice constant according to

$$\frac{\Lambda(x)}{\Lambda_0} = \frac{\omega_0^{\mathrm{lbe}}}{\omega^{\mathrm{lbe}}(x)} = \frac{1}{1 - \alpha x^2}. \tag{3.13}$$

Provided $\alpha x^2 \ll 1$, it can be simplified to

$$\Lambda(x) = \Lambda_0(1 + \alpha x^2). \tag{3.14}$$

Eq. (3.14) introduces a quadratic dependency of the lattice constant Λ on the x coordinate. It should be noticed that $\alpha \propto 1/\sigma^4$, so for large values of α the field has a narrow Gaussian envelope in the real domain, which results in undesirable broadened spectral components in the Fourier domain.

Optimal taper parameters. In our design, the untapered Bragg mirrors are chosen as conventional quarter-wave stacks comprising N_{Bragg} unit cells (on each side) of lattice constant $\Lambda_{\mathrm{Bragg}} = (\lambda_0/4)(1/n_1 + 1/n_2)$ and filling fraction $f_{\mathrm{Bragg}} = n_2/(n_1 + n_2)$ (we restore the subscript), where $n_1 = n_{\mathrm{eff}}$ and $n_2 = n_{\mathrm{bare}}$ are the effective indices defined above. Eq. (3.14) shows that a quadratic taper profile results in the desired Gaussian field attenuation. With a finite number N_{taper} of stacks in the taper, the lattice period is changed stepwise according to

$$\Lambda_i = \Lambda_0(1 + \alpha(i/N_{\mathrm{taper}})^2), \tag{3.15}$$

where the integer $i \in [-N_{\mathrm{taper}}, N_{\mathrm{taper}}]$ and Λ_0 is the minimum lattice constant (at the cavity center). The filling fraction is kept constant throughout: $f_i = f_{\mathrm{Bragg}}$. Under the continuity condition $\Lambda_{\pm N_{\mathrm{taper}}} = \Lambda_{\mathrm{Bragg}}$ at the taper boundaries, which implies

that $\alpha = \Lambda_{\text{Bragg}}/\Lambda_0 - 1$, Eq. (3.15) can be written in the form

$$\Lambda_i = \Lambda_0 + (\Lambda - \Lambda_0)(i/N_{\text{taper}})^2. \tag{3.16}$$

We can make an estimate of the modulation parameter α by choosing Λ_0 such that the lower-bandedge frequency ω_0^{lbe} at the cavity center is equal to the midgap frequency of the outer Bragg mirror, i.e., $\omega_0^{\text{lbe}} = \omega_{\text{Bragg}}^{\text{mid}}$. From Eqs. (1.3) and (1.4), we express $\omega_{\text{Bragg}}^{\text{mid}} \simeq \pi c/(n\Lambda)$ and

$$\omega_0^{\text{lbe}} = \omega_0^{\text{mid}} - \frac{\Delta\omega_0}{2} = \omega_0^{\text{mid}}\left(1 - \frac{\Delta\omega_0}{2\omega_0^{\text{mid}}}\right) \simeq \frac{\pi x}{n\Lambda_0}\left(1 - \frac{\Delta n}{n\pi}\right), \tag{3.17}$$

with $\Delta n = |n_1 - n_2|$ the refractive index contrast and $n = (n_1 + n_2)/2$ the average refractive index. Eq. (3.17) entails

$$\frac{\Lambda_0}{\Lambda_{\text{Bragg}}} \simeq 1 - \frac{\Delta n}{n\pi}, \qquad \text{hence} \qquad \alpha \simeq \frac{1}{1 - \Delta n/(n\pi)} - 1. \tag{3.18}$$

It should be noticed that (3.18) is a rough estimate, for α (which controls the depth of the optical potential well) should be adjusted according to the choice of N_{taper} (which affects the width of the optical potential well), such that the cavity mode is tuned at the target frequency.

It should be possible to achieve arbitrarily high in-plane Q factors by increasing N_{taper}. However, this requires arbitrarily fine (subnanometer) features, not feasible with the current fabrication technology. In addition, an increase in N_{taper} leads to a flatter quadratic taper profile, in which the stacks neighboring the cavity center display almost the same thickness. As a consequence, the field distribution in the real domain exhibits a plateau in this region, with an envelope function not dissimilar to Eq. (3.4) (where in this case L is the spatial extension of the plateau) and a large fraction of leaky Fourier components.

3.3. Simulation results and discussion

We consider a PhCNC on the usual truncated TiO_2/SiO_2 multilayer loaded with a PMMA ridge, operating in the visible spectrum at $\lambda_0 = 532\,\text{nm}$. The multilayer is composed of two alternating $TiO_2(a)/SiO_2(b)$ layers of thicknesses $d_a = 100\,\text{nm}$ and $d_b = 182\,\text{nm}$, and refractive indices $n_a = 2.67$ and $n_b = 1.46$, respectively. The multilayer has $N = 15$ periods, and the first TiO_2 layer is truncated with thickness $d_\sigma = \sigma d_a$, where $\sigma = 0.11$. The ridge has width $w = 1\,\mu\text{m}$, thickness $t = 400\,\text{nm}$, and refractive index $n_{\text{ridge}} = 1.49$. The surrounding cladding is air ($n_{\text{clad}} = 1$). These parameters guarantee the existence of a TE-like guided BSW that propagates along the ridge with estimated propagation loss of about 5.4 dB/m, according to the polarization-wise argument outlined in Chapter 2.

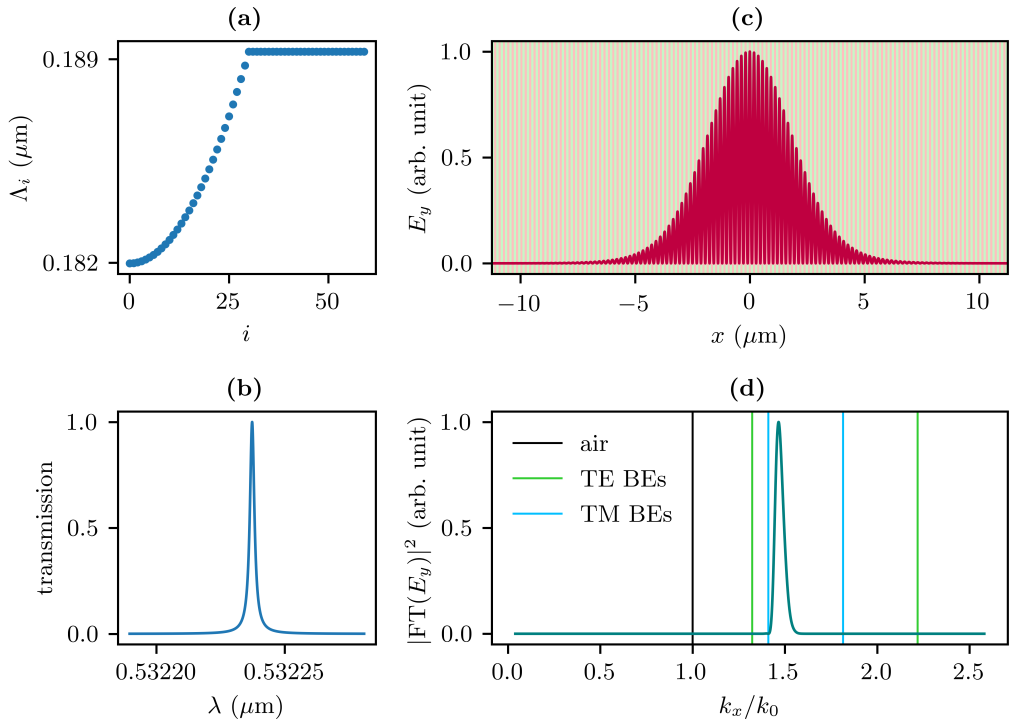

FIGURE 3.5. Electric field distribution and Fourier transform calculated via the TMM within the EI framework referenced in the text. (a) Lattice parameter Λ_i, the layer number i being counted from the cavity center. (b) Transmission spectrum at normal incidence showing the mode resonance at λ_0. (c) Electric field intensity (normalized to the maximum value) at normal incidence as a function of the spatial coordinate x ($x = 0$ is fixed at the cavity center, the external leads are omitted). (d) Fourier spectrum distribution (normalized to the maximum value) along the k_x axis. The air lightline (black) and the multilayer photonic bandedges (BEs) for TE (green) and TM (cyan) polarization are also shown.

The nanobeam is designed according to the previous EI-based guidelines using an in-house TMM code.[1]

First, we set the EI framework by determining the TE dispersion relations in the bare and loaded region, for which we find $n_{\mathrm{bare}} = 1.3416$ and $n_{\mathrm{load}} = 1.4918$, respectively (Figs. 1.11 and 1.12). The mode effective index is calculated by considering the fundamental TM guided mode for the effective slab waveguide with core of refractive index n_{load} and cladding of refractive index n_{bare}. It results $n_{\mathrm{eff}} = 1.4757$.

Second, we implement the in-plane effective multilayer with alternating layers of refractive indices $n_1 = n_{\mathrm{eff}}$ and $n_2 = n_{\mathrm{bare}}$ stacked along x. The ridge stacks and air slits have widths satisfying the quarter-wave condition, i.e., $s_{\mathrm{Bragg}} = \lambda_0/(4n_1) = 89\,\mathrm{nm}$ and $g_{\mathrm{Bragg}} = \lambda_0/(4n_2) = 100\,\mathrm{nm}$. The lattice constant results $\Lambda_{\mathrm{Bragg}} = 189\,\mathrm{nm}$ with filling fraction $f_{\mathrm{Bragg}} = 0.47$. The taper is created by modulating the lattice

[1] The author is grateful to Dr. Daniele Aurelio for his support in implementing the TMM code and stimulating discussion.

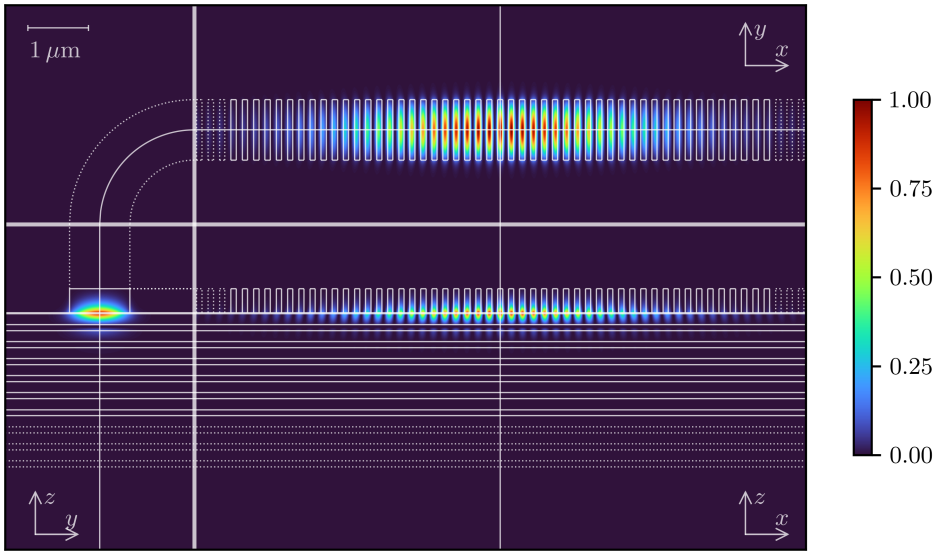

FIGURE 3.6. Intensity profile (normalized to the maximum value) of the electric field from 3D FDTD simulation.

constant quadratically according to Eq. (3.16) while keeping the filling fraction constant. The modulation spans $N_{\text{taper}} = 30$ periods in both directions away from the cavity center, the last stack having the same width of those of the Bragg mirrors. The lattice constant of the central stack is $\Lambda_0 = \Lambda_{\text{Bragg}}/(1+\alpha)$, where $\alpha = 0.04$ for the present structure, such that the cavity mode is tuned at λ_0 (Fig. 3.5(a)).

Third, we simulate the 1D effective multilayer by means of the TMM. The transmission spectrum reveals a resonance peak at λ_0 with a quality factor $Q_{1\text{D}} = \lambda/\Delta\lambda = 2.53 \times 10^5$ (Fig. 3.5(b)). This essentially accounts for energy loss through the finite number of layers in each Bragg mirror. It cannot be assumed as a direct estimate of the latter, though, for it is evaluated in the EI framework. Once the electric field profile is evaluated at the resonance frequency for normal incidence (Fig. 3.5(c)), the Fourier distribution can be calculated by a standard fast Fourier transform (FFT) algorithm. In Appendix A.5, we also suggest a possible computation directly using the TMM. Fig. 3.5(d) unveils that the majority of the Fourier components are outside the leaky region.

Finally, the structure is simulated via Ansys/Lumerical FDTD Solutions. We use a conformal mesh (maximum mesh step 10 nm) with a mesh refinement in a region around the truncation layer, where we expect the maximum field. It is a good tradeoff between numerical accuracy and computational resources, though full vectorial 3D simulations can take up to several hours on a standard computer. The simulation boundaries are terminated by PMLs. The mode is excited by an electric dipole. The Q factor is determined from the slope of the envelope of the decaying

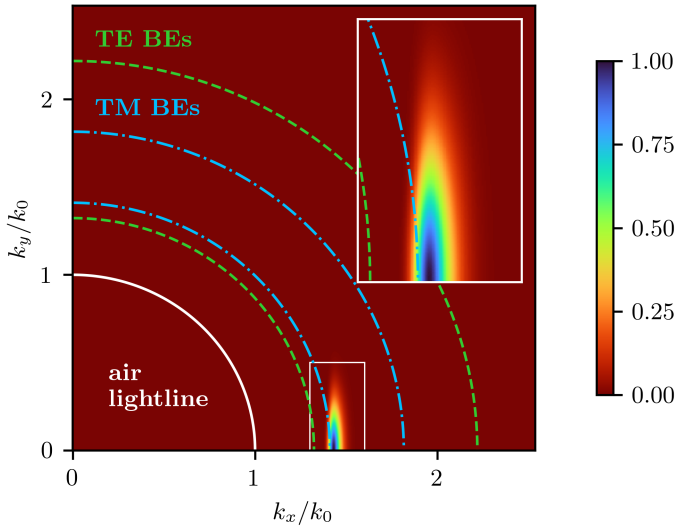

FIGURE 3.7. Fourier spectrum of the dominant electric field component E_y (normalized to the maximum value). The air lightline (white) and the multilayer photonic bandedges (BEs) for TE (dashed green) and TM (dash-dotted cyan) polarization are also shown.

time signal, recorded by a cloud of field time monitors. As a preliminary countercheck, we simulate the 2D in-plane structure (top view). We consider finite-sized stacks of refractive index n_{load} with width w and quadratically-modulated thickness s_i, whereas the background region has refractive index n_{bare}. A simulated quality factor $Q_{\text{2D,top}} = 1.7 \times 10^5$ is observed at the resonance wavelength $\lambda_{\text{2D,top}}/\lambda_0 = 0.998$, in conformity with the results provided by the TMM simulation. We then proceed with a full 3D FDTD simulation. It shows a quality factor $Q = 5.5 \times 10^4$ at a slightly detuned resonance wavelength $\lambda/\lambda_0 = 0.987$, thereby providing validation of our design assumptions. It should be noticed that Q is limited only by diffraction, thus with negligible loss in the multilayer. This depends on the large value of N considered here, which is sufficient to guarantee a strong attenuation of the field in the region of Fourier space in which the mode is localized. Further optimization of the multilayer could lead to a smaller N while preserving a high Q factor.

The electric field intensity profile of the fundamental mode of the cavity is illustrated in Fig. 3.6 over different cross sections (clockwise from top left: top, side, and front views). The mode is confined in three dimensions, the field being peaked at the interface between the multilayer and the ridge with the maximum intensity located at the central stack of the cavity. The corresponding Fourier spectrum is shown for the dominant component E_y in Fig. 3.7. As expected, it reveals a narrow profile mainly confined within the guiding region. Similar results hold for the other field components. The mode volume V is estimated to be $\sim \lambda_0^3$, which is two orders of magnitude smaller than the one estimated for a ring resonator with the same cross section and a radius $R = 100\,\mu\text{m}$.

In conclusion, we demonstrated a novel PhC resonator based on BSWs. This structure, characterized by a high Q/V and a field enhancement near the structure surface, has a small footprint size, is mechanically stable, is flexible in terms of constituent materials, and can be fabricated with etching-free technologies, e.g., from low-refractive-index polymeric ridges on commercially available multilayers. In principle, it can be implemented in a wide spectral range, from infrared to visible wavelengths. All these properties are not easily obtained at once in conventional nanobeam cavities relying on high refractive index contrast to achieve ultrahigh Q/V ratio, which are typically realized in suspended structures with limited mechanical stability. This makes our platform appealing for a number of applications that require large enhancement of surface light-matter interaction, from optical sensing to quantum nanophotonics.

CHAPTER 4

Coupling BSWs: excitation of BSWs with gratings

4.1. Excitatation of BSWs

The excitation of BSWs is a major challenge in most of the current platforms. As explained in previous chapters, BSWs exist within the PBG of the underlying multilayer and below the lightline of the cladding medium. Consequently, they cannot be excited directly by light incident from free space, in that their propagation constant is always larger than that of any radiation mode. Thus, one needs to provide additional momentum to the wavevector of the incident radiation mode to fulfill the phase matching condition with the BSW propagation constant. The most common and conceptually simple solution is to use a *dielectric prism*, either in the so-called Kretschmann configuration, in which the multilayer structure is deposited on top of the prism (Fig. 4.1(a)), or Otto configuration, in which there is an air gap between the multilayer and the prism (Fig. 4.1(b)). By tuning the angle of incidence of the totally reflected beam inside the prism, it can be phase-matched and efficiently coupled to the BSW. Prism coupling is widely used in sensing schemes, but, in general, it is bulky and not compatible with the concept of integrated optics. Very recently, though, an integrated microprism coupler in the Otto configuration was proposed to implement highly efficient unidirectional coupling [156].

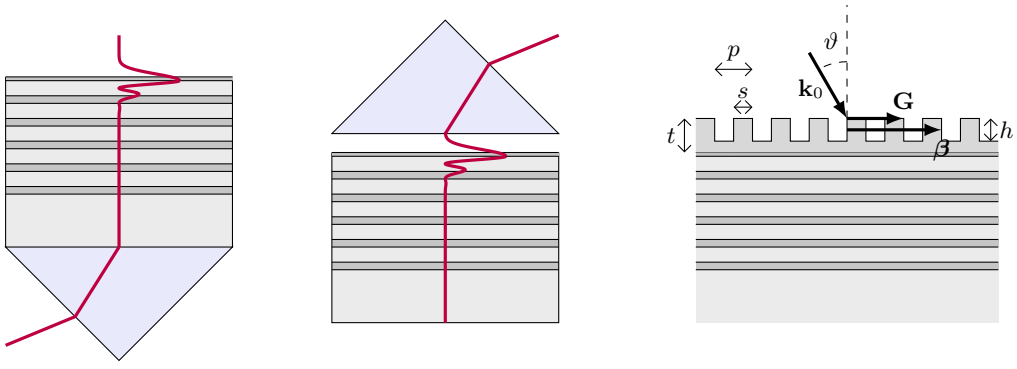

(a) Kretschmann configuration

(b) Otto configuration

(c) grating coupler

FIGURE 4.1. Coupling schemes used to excited BSWs. Cross sectional schematics of (a) prism coupling in the Kretschmann, (b) prism coupling in the Otto configuration, and (c) grating coupling using a uniform diffraction grating.

Another approach is the use of *gratings*, in which light incident near vertically above the structure can be coherently diffracted into the surface modes. Fig. 4.1(c) illustrates a uniform grating coupler patterned on top of a truncated PhC in air ($n_{\text{clad}} = 1$). Each diffracting unit consists of a tooth of length s and thickness t, and a trench of length g and depth $h \in (0, t)$. The grating *pitch* is the period of the diffracting unit, $p = s + g$, and the *duty cycle* is the filling fraction with respect to the tooth length, $d = s/p$. Let $k_0 = 2\pi/\lambda_0$ be the free space wavevector of the incident beam, tilted by an angle ϑ with respect to the vertical direction, and $\beta = n_{\text{eff,a}} k_0$ the propagation constant of the coupled surface mode propagating along the waveguide with the grating, where $n_{\text{eff,a}}$ is the average effective index. In general, $n_{\text{eff,a}} \neq n_{\text{eff}}$ (the effective index of the surface mode without the grating). For a weakly perturbing grating, $n_{\text{eff,a}}$ can be approximated by n_{eff}, which is not necessarily the case in PhC ridges, though. We can write the phase matching condition (Bragg's condition) as

$$k_0 \sin\vartheta + mG = \beta, \tag{4.1}$$

where m is the (integer) diffraction order and $G = 2\pi/p$ is the additional wavevector provided by the grating. Due to their diffractive behavior, grating couplers are wavelength selective. This is advantageous in terms of mode selectivity but comes at the price of narrow bandwidth (no bandwidth in an ideally infinite grating) and stringent fabrication tolerance. Slight detuning from the peak wavelength or tiny variations of some structural features can result in a degradation of the coupling efficiency.

The idea of grating-assisted excitation of BSWs was first proposed by Kang et al. [157] and by Scaravilli et al. [158] for biosensing applications. In these works, the diffraction grating is realized at the bottom of the multilayer in order to couple a BSW on the opposite facet. This configuration is intended to prevent the grating deterioration when exposed to the sensing environment. The concept was experimentally validated by directly writing the grating on the tip of a single-mode fiber, and subsequently depositing the multilayer [159]. For applications in integrated optics, grating couplers have been scarcely investigated. Kovalevich et al. reported a double cross grating coupler capable of controlling the BSW propagation direction by switching the polarization of the incident light [50]. Input and output grating couplers fabricated using two-photon polymerization (2PP) were also demonstrated by Abrashitova et al. [51, 52].

Achieving large fiber-to-chip coupling efficiency is the principal concern with grating couplers even in silicon photonics [133], let alone much more complex BSW-based platforms. In a grating coupler for BSW-based waveguide systems, loss arises from multiple mechanisms, as illustrated in Fig 4.2. We follow a notation analogous to the one used in [160]. For input coupling (left side of Fig. 4.2), only a fraction η (coupling efficiency) of the input power (P_{in}) is actually coupled to the waveguide (P_{wg}).

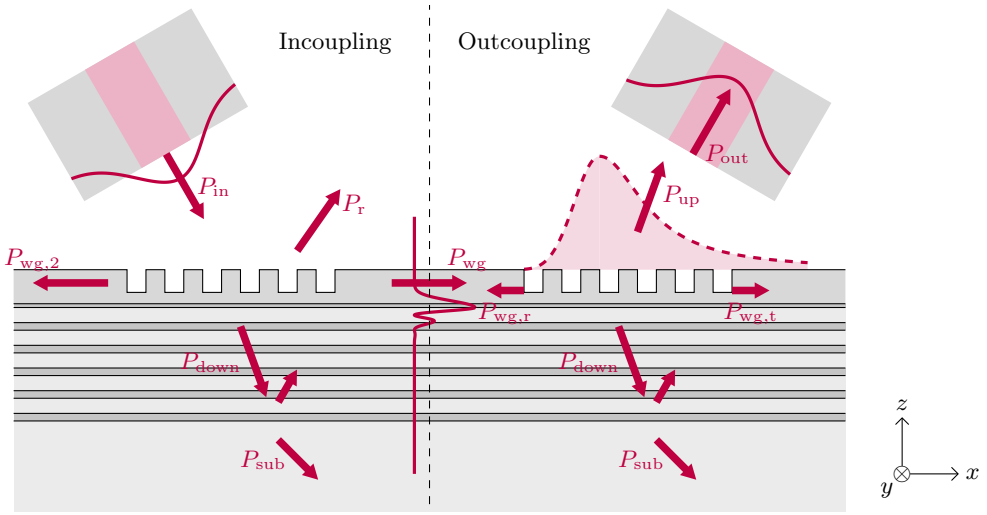

FIGURE 4.2. Loss channels in input and output grating coupling. Adapted from [160].

Some power is coupled opposite to the waveguide ($P_{wg,2}$) and some is reflected to the free space (P_r). Finally, some power will propagate downward (P_{down}): part of it is actually reflected upward to the waveguide, but another part will ultimately leak in the substrate (P_{sub}). The power coupled to the waveguide is given by

$$P_{wg} = \eta P_{in} = P_{in} - P_{sub} - P_r - P_{wg,2}. \tag{4.2}$$

We notice that adopting a fiber tilt angle in place of perfectly vertical coupling prevents bidirectional propagation of coupled light and reduces $P_{wg,2}$ (at $\vartheta = 0$, $P_{wg,2} = P_{wg}$ for diffraction order $m = \pm 1$).

In the output configuration (right side of Fig. 4.2), the situation is slightly more complicated, for the intensity profile diffracted upward by the grating is, in general, different from that of the optical fiber. For a uniform grating, it has a nearly exponential decay shape, with a reduced overlap with the Gaussian profile of the fiber mode. Thus, the outcoupled power (P_{out}) depends also on the overlap factor Γ_{out} of the two field patterns according to

$$P_{out} = \eta P_{wg} = \Gamma_{out} P_{up} = \Gamma_{out}(P_{wg} - P_{sub} - P_{wg,t} - P_{wg,r}), \tag{4.3}$$

where P_{wg} is the power in the waveguide, P_{up} is the power diffracted upward, P_{sub} is the power leaked in the substrate, $P_{wg,t}$ is the power transmitted beyond the grating, and $P_{wg,r}$ is the power reflected back to the waveguide at the grating interface. The overlap factor Γ_{out} is given by

$$\Gamma_{out} = \frac{\left| \int E^*_{up}(x) E_{out}(x)\, dx \right|^2}{\int |E_{up}(x)|^2\, dx \int |E_{out}(x)|^2\, dx}, \tag{4.4}$$

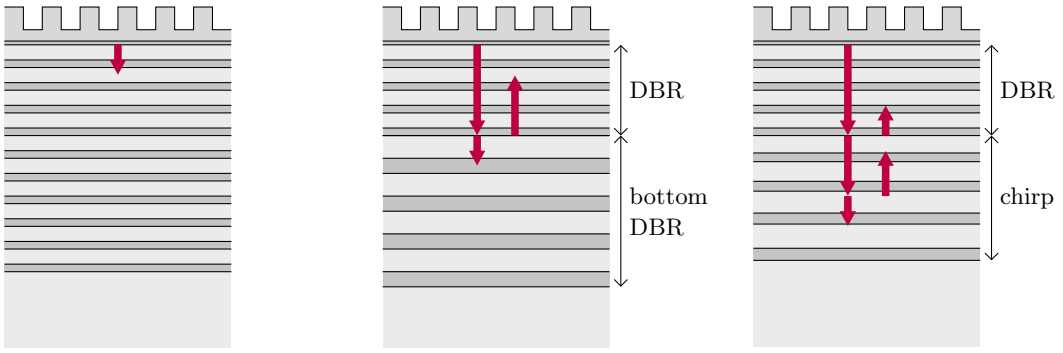

(a) dual-purpose DBR (b) two-segment DBR (c) linearly chirped DBR

FIGURE 4.3. Design strategies to enhance the directionality of grating couplers on PhC ridges: (a) dual-purpose DBR, (b) two-segment DBR, and (c) chirped DBR. The red arrows illustrate the power radiated downward and "recycled" upward.

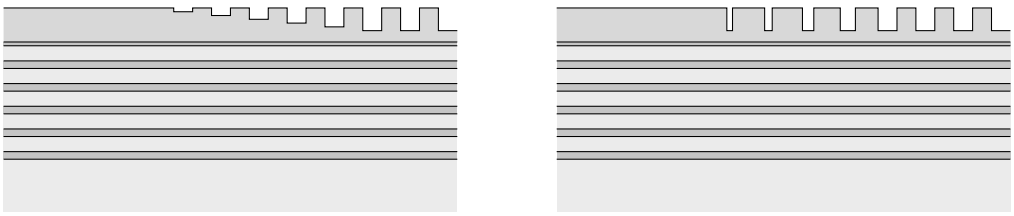

(a) apodized trench depth (b) apodized duty cycle

FIGURE 4.4. Nonuniform grating couplers on PhC ridges: (a) linear apodization of trench depth and (b) linear apodization of duty cycle (with constant pitch).

where E_{up} and E_{out} are the field profiles of the mode diffracted upward and the fiber mode, respectively; x is the propagation direction. Sometimes, another figure of merit called directionality is introduced, which is nothing but the ratio $P_{\text{up}}/P_{\text{wg}}$. Poor directionality in grating couplers is consequent to substantial fraction of power being radiated downward and eventually leaked in the substrate.

The coupling efficiency can be increased by improving both the directionality and the overlap factor. One straightforward way to enhance the directionality is to recover part of the power radiated downward by inserting a backreflector at the bottom of the grating. It comes naturally in PhC ridges since the multilayer itself, which already provides the PBG for sustaining the surface mode, can be engineered to suppress substrate leakage. For instance, one can choose the unit cell composition (lattice constant and filling fraction) of the multilayer in the first place, such that it results highly reflective also in this range of interest (Fig. 4.3(a)). Otherwise, one can change the multilayer parameters, either by gradually chirping them (Fig. 4.3(c)) or simply by juxtaposing a different multilayer (Fig. 4.3(b)). Incorporating a backreflector in

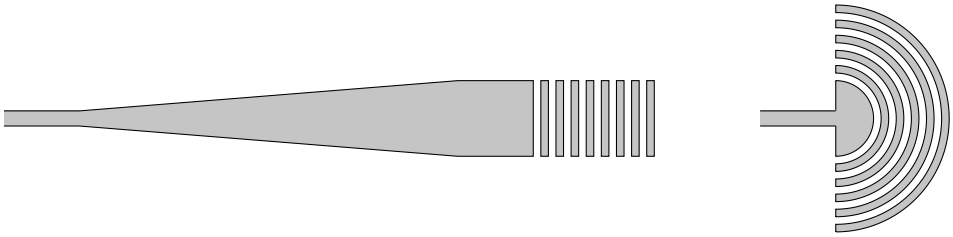

(a) linear taper (b) focusing grating

FIGURE 4.5. Top view of (a) grating with rectangular trenches and varying taper width (b) focusing grating with circular trenches.

PhC ridges adds no further complexity to the fabrication, since the layer thicknesses can be varied throughout the deposition process.

The overlap factor can be increased by employing nonuniform (apodized) gratings, e.g., by using multiple trench depths (Fig. 4.4(a)) or by varying the pitch and/or duty cycle of each diffracting unit (Fig. 4.4(b)). This allows one to tailor the diffracted field profile and mitigate the mismatch with the Gaussian field profile of the fiber mode. Linearly apodized gratings are reportedly fit for purpose, though more complex and time consuming optimization techniques lead to substantially improved overlap factors [130].

So far, we have considered the grating behavior only along the propagation direction x. However, the grating width in the y direction is also an important feature, for it must accommodate the spot size of the fiber (about 10 µm in telecom-wavelength fibers and 5 µm in visible-wavelength fibers). This is larger than the typical waveguide width (micrometric or submicrometric, to ensure single-mode operation), so a mode size converter must be implemented. It can consist of a linear taper of hundreds of microns (Fig. 4.5(a)), which allows for an adiabatic transition, or other small-footprint focusing configurations (Fig. 4.5(b)), in which the grating trenches are shaped as ellipses with one common focal point at the integrated waveguide.

In the following section, starting from the basic design of a uniform grating, we discuss some possible approaches for coupling efficiency enhancement. As usual, we are interested in polymer-loaded PhC ridges for visible light operation. We stress that the moderately low refractive index of polymeric materials strongly reduces the attainable grating strength. It aggravates the already existing difficulty in realizing efficient grating couplers for BSW-based waveguide systems, which are plagued by multiple loss channels due to the much complex confinement mechanism. Still, the advantages of gratings in terms of flexible design, ease of fabrication, and tolerant positional requirements make them a preferred candidate for BSW coupling in integrated devices. For reasons of expediency, the designs are carried out on the 2D cross-sectional model of the structure, and full 3D modeling is left for future research.

Though, we believe that it shall not represent a major challenge, for transition tapers and focusing grating couplers have been successfully demonstrated in many other platforms, even using low-refractive-index-contrast materials in the visible and near-visible wavelength range [131], and often show negligible difference between 2D and 3D simulations [161].

4.2. Simulation results and discussion

An exhaustive analysis is virtually impossible because of the enormous parameter space. Thus, we shall limit our attention to the structures considered in the previous chapters, with the aim of providing them with an excitation scheme compatible with the idea of integrated circuits. We start from the PhC ridge supporting long-range BSWs described in Chapter 2 (case C). Namely, it consists of a TiO_2 (refractive index $n_a = 2.67$)/SiO_2 (refractive index $n_b = 1.46$) periodic multilayer with $N = 10$ periods of lattice constant $\Lambda = 440\,\text{nm}$ and filling fraction $f = 0.22$. Its TE/TM gapmap is illustrated in Fig. 4.7(c). The multilayer is truncated with a 10 nm-thick TiO_2 layer and loaded with a PMMA ($n_{\text{ridge}} = 1.49$) ridge of width $w = 1.0\,\mu\text{m}$ and thickness $t = 0.4\,\mu\text{m}$ in air. As usual, we operate at a target wavelength $\lambda_0 = 532\,\text{nm}$. This geometry guarantees the existence of a TE-like guided BSW that propagates along the ridge with effective index $n_{\text{eff}} = 1.483$ and intrinsic propagation loss of about 5.7 dB/km.

Ansys/Lumerical FDTD Solutions is used to model the longitudinal 2D cross section of the structure. A sketch of the computational domain is presented in Fig. 4.6. We consider the grating as an incoupling device. A Gaussian beam of waist radius 2 µm (comparable to that of standard SMFs operating in the visible range) is launched from a source plane 5 µm above the structure, with an offset distance 15 µm from the left edge of the grating. The input beam consists of a frequency-domain pulse centered at $\lambda_0 = 532\,\text{nm}$ with bandwidth $\Delta\lambda_0 = 50\,\text{nm}$. As mentioned before, using a non-normal angle of incidence can provide better directionality to the light coupled through the grating. In particular, we use a negative tilt angle $\vartheta = -12^\circ$ (backscattering design), also in view of matching a possible angular-polished end face of the fiber array. The electric field of the Gaussian beam is polarized along the y direction. A frequency-domain power monitor spanning the height of the simulation domain is placed 50 µm away from the left edge of the grating to compute the optical power coupled to the waveguide (normalized to the source power) (T_{wg}). Such a distance ensures that spatial transient fields have decayed sufficiently to be negligible. A second monitor is used to compute the optical power flowing in the direction opposite to the waveguide ($T_{\text{wg},2}$). Similarly, other two monitors spanning the width of the simulation domain are placed at the top and bottom of structure to evaluate the power reflected upward (T_{up}) or radiated downward (T_{down}). The normalized power

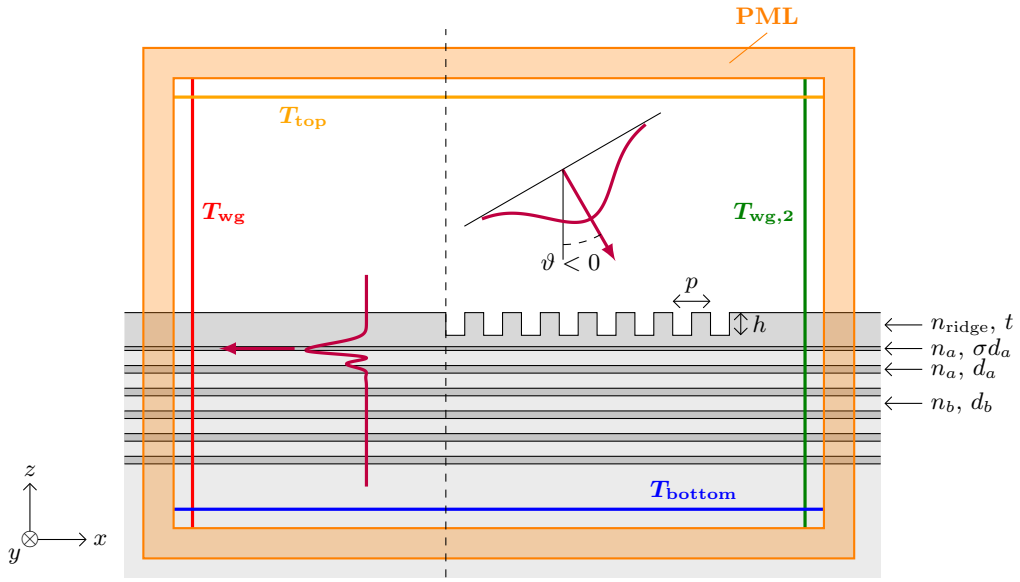

FIGURE 4.6. Schematic of the longitudinal 2D cross section of a PhC ridge with a grating coupler (here, sketched as uniform for simplicity). The computational domain is terminated by PMLs (orange thick line). A Gaussian beam tilted by a negative angle ϑ with respect to the normal direction is launched above the grating (backscattering design). Four power monitors are used to compute the power flowing along the $-x$ direction into the waveguide (red solid), along the x direction (green solid), downward in the substrate (blue solid), and upward in free space (yellow solid), respectively. The dashed line correspond to the left edge of the grating.

transmission (as a function of wavelength) for each monitor is calculated as

$$T(\lambda) = \frac{\frac{1}{2}\int_{\text{monitor}} \text{Re}(\mathbf{S}(\lambda)) \cdot \text{d}\mathbf{a}}{\text{source power}(\lambda)} \tag{4.5}$$

where $\mathbf{S}$ is the Poynting vector and d$\mathbf{a}$ is the surface normal. The simulation grid is defined as an automatic conformal mesh, with an additional refinement at the truncation layer, and is terminated by PML boundaries.

Starting from Bragg's condition (4.1), the grating pitch must satisfy, for the lowest grating order ($m = 1$),

$$p = \frac{\lambda_0}{n_{\text{eff,a}} - \sin\vartheta}. \tag{4.6}$$

The grating effective index $n_{\text{eff,a}}$ is not always easily determined in the case of PhC ridges supporting BSWs. When dealing with *good* or *bad* BSWs, which originate from the surface mode supported by the bare multilayer owing to the dielectric perturbation, it can be reasonably approximated as $n_{\text{eff,a}} = dn_{\text{load}} + (1-d)n_{\text{bare}}$, where n_{bare} and n_{load} are the effective indices of the BSWs supported by the bare and loaded, respectively, and d is the duty cycle. For the present structure, $n_{\text{bare}} = 1.393$ and $n_{\text{load}} = 1.497$. We consider a fully etched grating, i.e., $t = h = d_{\text{ridge}} = 400\,\text{nm}$, with

a duty cycle $d = 0.5$. Exact tuning of p can be performed by running a 2D FDTD simulation using a broadband pulse source and checking that $T_{\mathrm{wg}}(\lambda)$ is peaked at λ_0; otherwise, one scales p accordingly. Here, we set $p = 324\,\mathrm{nm}$. Notice that, on account of the dimensionality reduction in 2D simulations, the ridge on top of the multilayer should be substituted with an effective homogeneous medium of refractive index $n_{\mathrm{eff,ridge}}$, where $n_{\mathrm{eff,ridge}}$ is the effective index of the fundamental mode supported by a symmetric air/ridge/air slab waveguide of width equal to the extension w_{gc} of the grating in the y direction. Since the grating must accommodate the spot size of the fiber, w_{wg} must be greater than $4\,\mu\mathrm{m}$. It results $n_{\mathrm{eff,ridge}} = 1.489$ in the case of $w_{\mathrm{gc}} = 4\,\mu\mathrm{m}$, therefore, in practice, we can safely use $n_{\mathrm{eff,ridge}} = n_{\mathrm{ridge}}$.

Starting from a uniform design with constant pitch $p = 324\,\mathrm{nm}$ and duty cycle $d = 0.5$, we introduce a linear apodization spanning $20\,\mu\mathrm{m}$ on the grating. Namely, we linearly modify the duty cycle such that the trench next to the waveguide segment has a minimal feature of $50\,\mathrm{nm}$ (in practice, it should correspond to the smallest feature achievable in the fabrication process). By doing so, the grating effective index can be slowly increased to match the waveguide mode effective index, which significantly reduces the scattering at the grating/waveguide boundary.

The time-averaged distribution of the electric field in the longitudinal cross section is shown in Fig. 4.7(b). The coupling efficiency is the fraction of power that couples from the incident Gaussian beam to the BSW mode of the waveguide. In reality, the actual transmitted field in the $-x$ direction does not have exactly the same profile of the guided BSW (Fig. 4.7(a)). This is not surprising, considering that the photonic structure supports a multiplicity of modes other than the BSW, most of which are in fact highly lossy and rapidly decay to zero. As a result, the coupling efficiency can be evaluated from the normalized power transmission T_{wg}, reduced by an overlap factor Γ_{in} that accounts for the difference in the field distribution between the BSW (E_{bsw}) and the actual transmitted field (E_{wg}):

$$\Gamma_{\mathrm{in}} = \frac{\left| \int E^*_{\mathrm{bsw}}(z) E_{\mathrm{wg}}(z)\,\mathrm{d}z \right|^2}{\int |E_{\mathrm{bsw}}(z)|^2\,\mathrm{d}z \int |E_{\mathrm{wg}}(z)|^2\,\mathrm{d}z}. \tag{4.7}$$

We report $T_{\mathrm{wg}} \approx 8.4\%$ and $\Gamma_{\mathrm{in}} \approx 92.4\%$, with an overall coupling efficiency $\eta = \Gamma_{\mathrm{in}} T_{\mathrm{wg}} \approx 7.8\%$. This also explains the intensity beat that can be seen along the waveguide, which is attributed to a (moderately lossy) spurious mode that is excited in the waveguide with a slightly different propagation constant ($n_{\mathrm{eff}} = 1.359$). The phase difference between this mode and the BSW is compatible with the observed beatlength of about $3.7\,\mu\mathrm{m}$. This spurious mode is actually extinguished over few tens of microns.

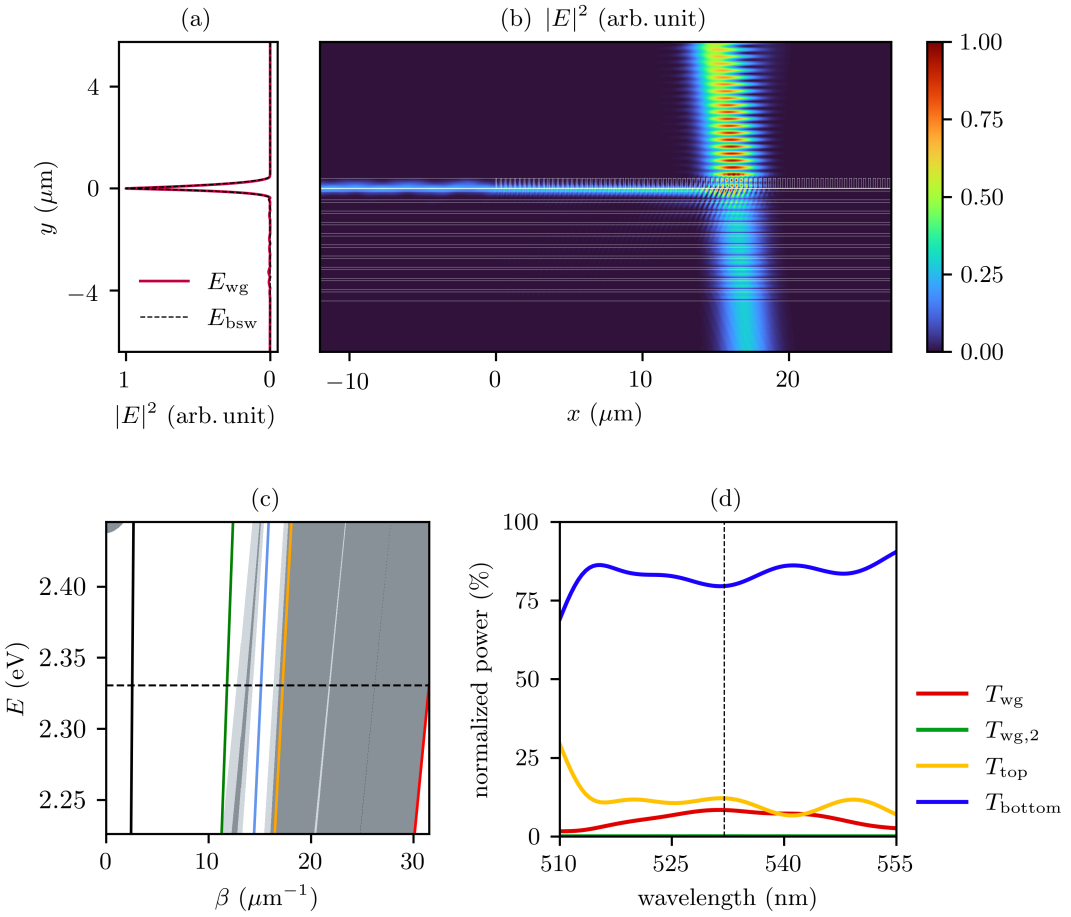

FIGURE 4.7. Distribution of $|E|^2$ computed using the FDTD (a) over the line power monitor T_{wg} and (b) over the longitudinal 2D cross section of the structure. (c) Gapmap of the underlying multilayer (lattice constant $\Lambda = 440\,\mathrm{nm}$, filling fraction $f = 0.22$) along with the lightlines of free space (green), SiO_2 (orange), TiO_2 (red), free space at a tilt angle $-12°$ (black), and at SiO_2/TiO_2 Brewster's angle (lightblue). The TE (TM) PBG is represented by the light (dark) area. (d) Transmitted normalized power across the monitors T_{wg} (red), $T_{\mathrm{wg,2}}$ (green), T_{top} (yellow), and T_{bottom} (blue).

We notice that the normalized power $T_{\mathrm{wg,2}}$ transmitted in the direction opposite to the waveguide is almost zero owing to the use of negative tilt angle. However, a considerable fraction $T_{\mathrm{down}} \approx 80\%$ leaks in the substrate. Indeed, the multilayer is designed according to the procedure of Chapter 2 to exhibit wide and well-overlapping TE and TM PBGs for $k_{\parallel} \geq k_0 n_{\mathrm{eff}}$, with $k_{\parallel} = (k_x, k_y)$ the in-plane wavevector, whereas no PBG is present around the parallel component $k_0 \sin\vartheta$ of the incident wavevector. This is detrimental for the grating directionality, unless part this substrate leakage is "recycled" using one of the solutions illustrated in Fig. 4.3.

As a first alternative, we introduce $N_{\mathrm{bottom}} = 10$ additional periods to the multilayer structure, albeit with lattice constant $\Lambda_{\mathrm{bottom}} = 141\,\mathrm{nm}$ and filling fraction $f_{\mathrm{bottom}} = 0.35$, corresponding to a quarter-wave stack at the bottom of the structure

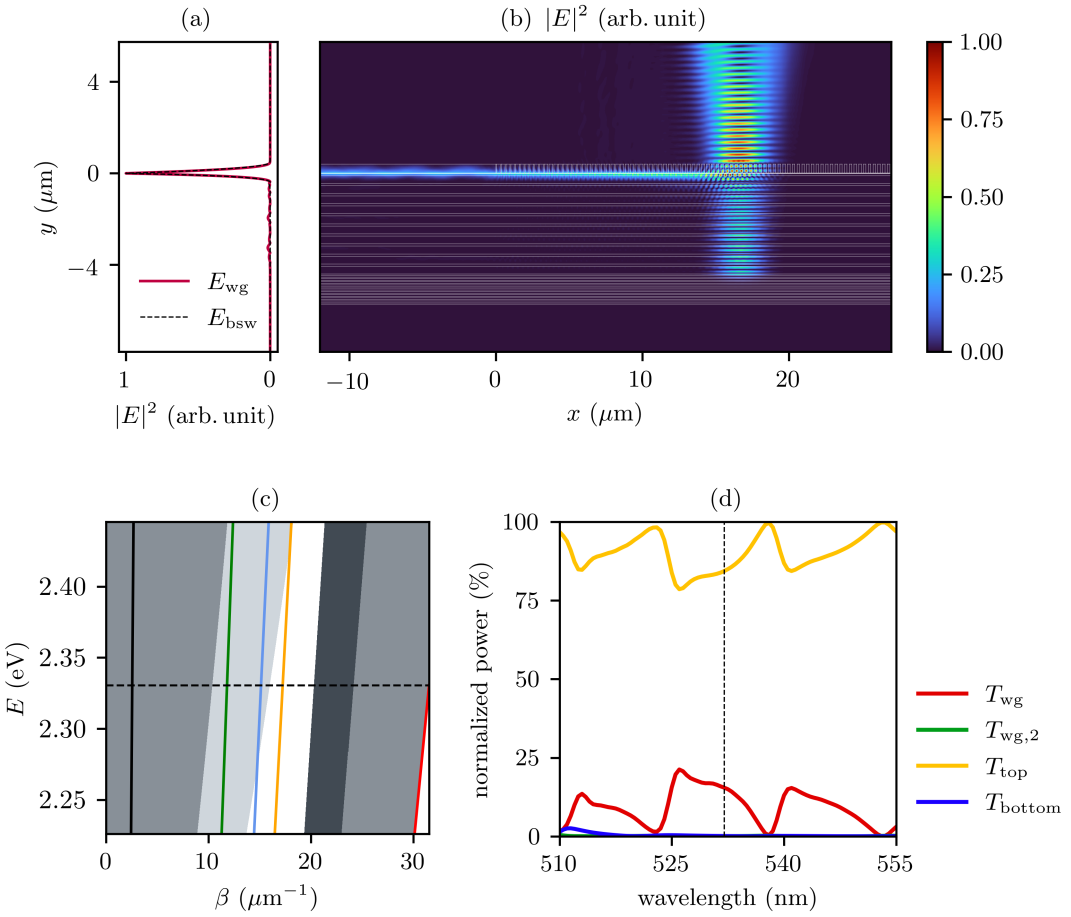

FIGURE 4.8. Distribution of $|E|^2$ computed using the FDTD (a) over the line power monitor T_{wg} and (b) over the longitudinal 2D cross section of the structure. (c) Gapmap of the multilayer bottom segment (lattice constant $\Lambda = 140\,\mathrm{nm}$, filling fraction $f = 0.35$) along with the lightlines of free space (green), SiO_2 (orange), TiO_2 (red), free space at a tilt angle $-12°$ (black), and at SiO_2/TiO_2 Brewster's angle (lightblue). The TE (TM) PBG is represented by the light (dark) area. The gapmap of the top segment is the same of Fig. 4.7(c). (d) Transmitted normalized power across the monitors T_{wg} (red), $T_{\mathrm{wg,2}}$ (green), T_{top} (yellow), and T_{bottom} (blue).

(Fig. 4.3(b)). Hence, the top multilayer segment is designed to support a long-range BSW, while the bottom segment is designed to function as a backreflector, with increased reflectivity around the angle of incidence (see Fig. 4.8(c)). The grating geometry is unaltered. The time-averaged distribution of the electric field is shown in Fig. 4.7(b). As expected, the high reflectivity provided by the bottom segment results in $T_{\mathrm{down}} \approx 0$ and, consequently, an increase in the power coupled to the waveguide, with $T_{\mathrm{wg}} \approx 15.5\%$. Although this "recycling" mechanism is also responsible for some parasitic scattering in the bulk modes of the PhC ($\Gamma_{\mathrm{in}} \approx 91.5$), the coupling efficiency is $\eta \approx 14.2\%$, which is almost twofold with respect to the one-segment multilayer.

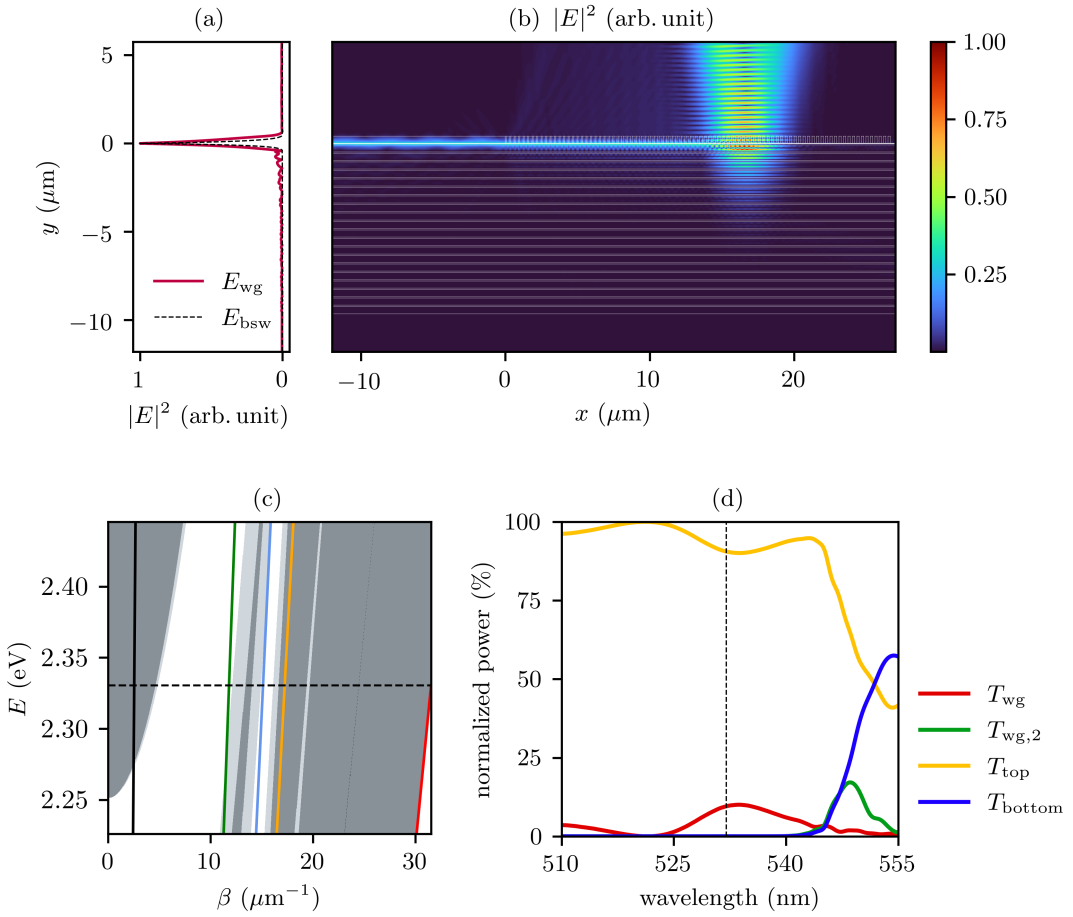

FIGURE 4.9. Distribution of $|E|^2$ computed using the FDTD (a) over the line power monitor T_{wg} and (b) over the longitudinal 2D cross section of the structure. (c) Gapmap of the underlying multilayer (lattice constant $\Lambda = 482\,\mathrm{nm}$, filling fraction $f = 0.15$) along with the lightlines of free space (green), SiO_2 (orange), TiO_2 (red), free space at a tilt angle $-12°$ (black), and at SiO_2/TiO_2 Brewster's angle (lightblue). The TE (TM) PBG is represented by the light (dark) area. (d) Transmitted normalized power across the monitors T_{wg} (red), $T_{\mathrm{wg,2}}$ (green), T_{top} (yellow), and T_{bottom} (blue).

This result is on par with those reported in recent literature, with coupling efficiency up to 18% at telecom wavelengths [50].

As a second alternative, we modify the multilayer structure in the first place, namely, by choosing $\Lambda = 482\,\mathrm{nm}$ and $f = 0.15$. The truncation thickness and ridge parameters are left unchanged. Naturally, we are considering a different structure from the previous case, but it sustains a BSW with comparable effective index $n_{\mathrm{eff}} = 1.484$ ($n_{\mathrm{load}} = 1.498$, $n_{\mathrm{bare}} = 1.395$) and field distribution. However, the multilayer is now designed with a dual purpose, i.e., to support a BSW and, simultaneously, to provide a stopband around the angle of incidence ϑ, as can be seen from the gapmap in Fig. 4.9(c). In this case, the grating pitch is modified to $p = 310\,\mathrm{nm}$ to fulfill Bragg's condition. The simulation results are shown in Fig. 4.9. We obtain $T_{\mathrm{wg}} \approx 10\%$ and

$T_{\text{bottom}} \approx 0$, without significant improvement of the coupling efficiency, which results $\eta = 9.7\%$ (overlap factor $\Gamma_{\text{in}} \approx 97.1\%$). This is not entirely surprising given the high reflectivity of the whole multilayer, for which most light is reflected back to the incidence medium ($T_{\text{top}} \approx 90\%$) and only a small fraction can be actually coupled. This is a major drawback of this strategy, which was worth to be investigated anyway.

In conclusion, we examined the possibility of efficiently coupling BSWs using diffraction gratings. This approach can facilitate the integration of BSW-based devices, eliminating the requirements of bulky prisms. Indeed, they are compatible with the same fabrication process used to manufacture the PhC ridge, and can be easily adapted to achieve fairly good coupling efficiency by using apodized designs or directionality-improving backreflectors.

CHAPTER 5

Conclusion and perspectives

Controlling light in 2D integrated platforms is one of the most challenging efforts in today's photonics. If one focuses on dielectric structures, such control is achieved by exploiting only two different phenomena: total internal reflection (TIR) and/or interference, which gives rise to the formation of the so-called photonic band gaps (PBGs) in photonic crystal (PhC) structures. In Chapter 1, we briefly reviewed that these two effects can be combined in many different ways, leading to several configurations supporting propagating modes confined in two dimensions. An interesting case is that of Bloch surface waves (BSWs), electromagnetic modes that propagate at the interface between a truncated periodic multilayer and an external dielectric medium. In such truncated multilayers, light confinement in the vertical direction is obtained by means of TIR from the homogenous side and by the presence of a PBG from the multilayer side. In terms of surface field enhancement, BSWs have been shown to offer strategic advantages with respect to simpler solutions based only on TIR. BSWs provide large freedom in terms of constituent materials, from organic compounds to semiconductors, and operate in a wide spectral range, remarkably at visible wavelengths, for which there is paucity of transparent materials having a strong refractive index contrast.

In Chapter 2, we investigated the possibility of guiding BSWs by simply realizing polymeric ridge waveguides, which makes BSWs appealing for the development of an etchless, all-dielectric integrated photonic platform. Since one essential requirement for large-scale integration is that the overall loss should be low, we focused on propagation loss in BSW-based ridge waveguides. These systems are plagued by high propagation loss (of the order of dB/mm or higher) not only in experimental realizations but also in theoretical simulations of idealized structures free of material absorption and surface scattering. We addressed the problem by describing the simple design rule that light should be confined polarization-wise in order to achieve low propagation loss. For the BSW supported by the ridge is not purely TE (TM) polarized, but shows all nonvanishing field components as a consequence of the lateral confinement, the simultaneous presence of both TE and TM PBGs in the spectral region of interest is essential to guide all components. Another possible point of view is looking at the field distribution of the mode in the Fourier domain. Indeed, the field Fourier components that fall inside the cladding material light cone or outside

the corresponding PBG are not guided and can couple to radiation modes. This suggests that a possible approach to reduce propagation loss is minimizing the fraction of Fourier components in the leaky regions. This can be accomplished by changing the width and thickness of the ridge, which influences the field distribution and its Fourier transform, or by changing the multilayer composition (e.g., changing the filling fraction and, if necessary, the period), with the purpose of engineering the TE and TM PBG spectral position. In particular, we focused on the latter aspect, which turns out to be the most effective strategy. We showed that even a slight variation of the multilayer composition can determine a considerable modification in the spectral position and extension of the polarization-dependent leaky window, which can result in a dramatic increase or decrease in propagation loss. Proper design allowed us to reduce radiation loss to a level of dB/km without the need to resort to ultra-wide ridges, thus ensuring small mode areas in a single-mode regime.

In Chapter 3, we demonstrated a photonic crystal nanobeam cavity (PhCNC) in a PhC ridge supporting BSWs. This kind of resonator structure is characterized by a moderately high Q/V ratio and a large field enhancement close to the structure surface. In particular, we suggested the possibility of texturing two Bragg mirrors in a PhC ridge, each of which consisting of periodically spaced rectangular stacks. In our design, the Bragg mirrors are adiabatically tapered by quadratically resizing a number of stacks toward the cavity center. Tapering the Bragg mirrors is crucial to mitigate the effect of diffraction loss, which is expected to be the leading loss mechanism when one neglects scattering loss from fabrication imperfections and finite size effects of the multilayer. Once again, this can be understood by looking at the mode field distribution in the Fourier domain. The field Fourier components that fall inside the cladding material light cone or outside the multilayer PBG are not guided and can couple to the continuum of radiation modes. A smooth modification of the nanobeam geometry gives rise to a gentle variation of the electric field, and therefore, to a narrower distribution of its Fourier components, which can be piloted away from the leaky region. Light polarization plays an essential role, for the simultaneous presence of PBGs for both polarizations is always required to have each field component's Fourier distribution well-located within the appropriate PBG. We reported the design of a polymeric structure operating at visible wavelengths characterized by a Q factor exceeding 5×10^4 and mode volume $V \sim \lambda_0^3$.

At last, we tackled the critical aspect of coupling light from an optical fiber into a PhC ridge waveguide. A prevalent approach is to use bulky prisms, which are not compatible with the idea of an integrated structure. Thus, we investigated on the use of gratings. Grating couplers are well established in silicon photonics, and provide some of the highest coupling efficiencies. However, their application to PhC ridges is particularly challenging, given the complexity of the light confinement mechanism,

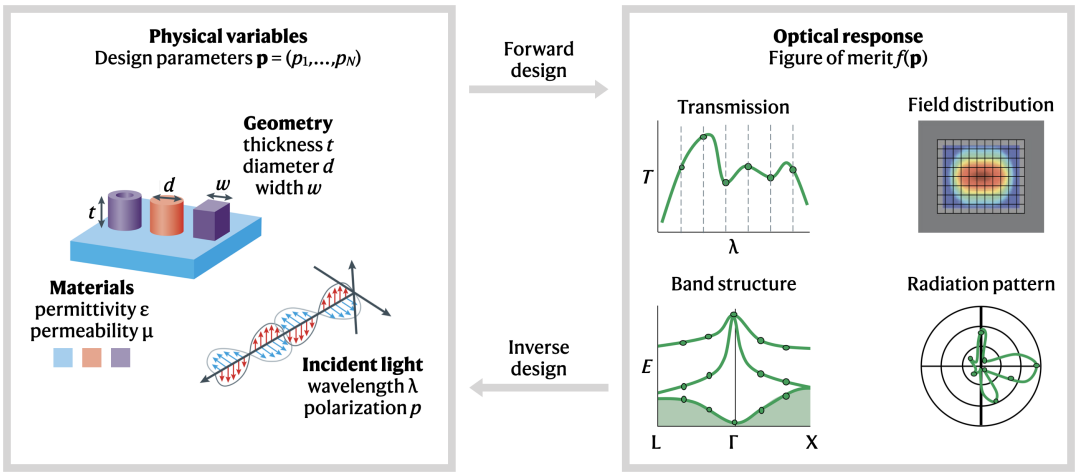

FIGURE 5.1. Forward and inverse design of photonic structures. Adapted from [162].

and hardly investigated in literature. In Chapter 4, starting from the basic design of a uniform grating, we discussed some possible approaches to enhance the coupling efficiency. Namely, to avoid incoupling in the direction opposite to the waveguide, we introduced a backscattering scheme with a negative angle of the incident beam. A linear apodization helped us improve the quality of the incoupled beam by attenuating the strong impedance mismatch at the grating/waveguide interface. Finally, we adopted some "recycling" strategies to mitigate light leakage in the multilayer and substrate. Choosing the unit cell composition of the multilayer such that it results highly reflective also at the angle of the incident beam can be a valid solution, but difficult to achieve since the PBGs must be simultaneously optimized to minimize propagation loss as well. More effectively, one can use a two-segment multilayer, where the top segment is designed to support the surface mode, while the bottom segment is designed to function as a backreflector. Starting from the same structure proposed in Chapter 2, we demonstrated that this latter strategy leads to a twofold increase in the coupling efficiency.

On a final note, we want to draw the reader's attention to the design process adopted throughout this work. It may be regarded as a forward design approach, in which the search for the optimal structure is primarily driven by our physical intuition. First, we specify the design parameters of a given structure (geometry, materials, excitation sources, etc.) according to our a priori theoretical assumptions and, second, we compute its optical response via the numerical electromagnetic solver, in order to minimize or maximize a certain figure of merit (FOM) that benchmarks the structure performance (e.g., BSW field distribution, waveguide propagation loss, cavity Q factor, grating coupling efficiency, etc.). This reflects the spirit of our work, in which the proposed designs are essentially understood as numerical proofs of concept

that help us clarify the relevant physical aspects of BSWs from a theoretical standpoint. However, this approach does not necessarily lead to an optimal design with the highest possible performance. Actually, by doing so, we explore just a small subspace of the entire parameter space, with only a handful of free parameters allowed by the physics-inspired design. Inspection by hand is clearly inefficient, while full inspection by brute-force parameter sweeping becomes, in general, computationally intensive. For instance, in the design strategy employed in Chapter 2 to improve the propagation length of BSWs guided by PhC ridges, first, we let the multilayer filling fraction be the only free parameter and, second, we fine-tuned the geometry through a brute-force sweeping of the ridge width. In principle, we could vary other geometrical parameters (multilayer period, truncation thickness, ridge thickness) or even working with a different topology (e.g., using quasi-periodic or aperiodic multilayers).

In contrast to the forward design approach, inverse design methods target the desired FOM and retrieve the optimal structure (Fig. 5.1) [163, 164]. By combining an electromagnetic solver with efficient optimization algorithms, either gradient-based (such as the adjoint method [165, 166]) or evolution-based (such as genetic algorithms [167] or particle swarm algorithms [168]), it is possible to manage a larger number of degrees of freedom at a much lower computational cost. Inverse design has led to a number of counterintuitive devices with better performance and smaller footprint than traditional devices, in a range of applications from silicon photonic components [169, 170] to photonic crystals [171] to metamaterials [172]. Thus, it could prove a powerful tool also for BSW-based optical components, capable of handling the complex properties of BSWs.

Among others, genetic algorithms (GAs) are a class of stochastic optimization methods inspired by the principles of natural evolution [173]. GAs operate on a population of individuals that are each represented by a chromosome $\mathbf{p} = (p_1, \ldots, p_N)$, where the genes p_i are the design parameter. Initially, a random population of individuals is formed and the fitness function $f(\mathbf{p})$, i.e., the FOM to be optimized, is evaluated for each individual. The better performing individuals are selected to form a mating pool. Optionally, a number of most-fit individuals are passed directly to the next generation with no change (elitism). Next, pairs of parent individuals are selected in the mating pool and their chromosomes are crossed over to form a new generation of child individuals, which will inherit their parents' genetic material. A small fraction of the offspring is randomly mutated to maintain a level of genetic diversity in the population. Once the new generation is populated, it can be evaluated by the fitness function and undergo the same process of selection, crossover, and mutation until the optimum is reached. GAs can produce highly optimized individuals in a relatively small number of generations, despite the vast space of all possible gene crossovers and mutation.

To date, a number of robust and fast-converging frameworks have been created for working with GAs. In particular, GAs are also suited for multiobjective optimization, i.e., when two ore more (possibly conflicting) FOMs must be optimized at once. In this case, there exists no single solution that simultaneously optimizes each FOM, but a multiplicity of solutions that are no worse than any other, in the sense that no FOM can be improved without deteriorating the others (Pareto optimum). We believe that multiobjective numerical optimization could be successfully applied in a number of contexts related to BSWs, e.g., designing ultra-low-loss PhC ridges while minimizing the effective mode area, or apodizing a grating coupler to simultaneously maximize coupling efficiency and bandwidth. It might be fruitful to first establish a properly constrained input solution by means of our forward design approach, and then apply a GA for further optimization.

In conclusion, we demonstrated the complete optical architecture necessary for a fully integrated operation of BSWs. It works in a wide spectral range (from visible to mid-IR wavelengths), is flexible in terms of constituent materials, has a small footprint size, is mechanically stable, and can be fabricated with etching-free technologies from low-refractive-index polymeric ridges on commercially available multilayers. All these properties, which are not easily obtained at once, make this structure well-suited for a number of applications requiring the enhacement of surface light-matter interaction. In particular, the use of cost-effective, mass-produced polymers with customizable physical and optical properties provides interesting functionalities. For instance, polymers can embed diverse quantum emitters, such as single molecules, quantum dots, or nitrogen-vacancy centers in diamond, opening the possibility of realizing on-demand single-photon sources. Furthermore, several organic and inorganic polymers show nonlinear optical (NLO) properties, with NLO coefficient up to two orders of magnitude larger than those of most semiconductors. Taking advantage of the remarkable nonlinearity of polymers and the small effective mode areas achievable in PhC ridges would be of great interest to access nonlinear regimes that are hard to explore in state-of-the-art integrated platforms, e.g., ultra-high-efficient four-wave mixing (FWM) or sub-milliwatt threshold for optical parametric oscillation (OPO).

APPENDIX A

General background

A.1. Plane waves in a dielectric

The behavior of the electromagnetic field in a medium is governed by macroscopic Maxwell's equations. In the absence of charges and currents, they read [1]

$$\begin{aligned} \nabla \cdot \mathbf{D} &= 0, \qquad & \nabla \times \mathbf{E} &= -\frac{\partial \mathbf{B}}{\partial t}, \\ \nabla \cdot \mathbf{B} &= 0, \qquad & \nabla \times \mathbf{H} &= \frac{\partial \mathbf{D}}{\partial t}, \end{aligned} \tag{A.1}$$

where $\mathbf{E}$ is the electric field and $\mathbf{H}$ is the magnetic field. The electric displacement $\mathbf{D}$ and the magnetic induction $\mathbf{B}$ are related to the electric and magnetic fields, respectively, by the constitutive relations $\mathbf{D} = \mathbf{D}(\mathbf{E})$ and $\mathbf{B} = \mathbf{B}(\mathbf{H})$, which depend on the medium electric and magnetic properties, the externally applied fields, etc. We shall be dealing with nonmagnetic, linear, and isotropic media, for which

$$\mathbf{D} = \varepsilon_0 \varepsilon \mathbf{E}, \qquad \mathbf{B} = \mu_0 \mathbf{H}, \tag{A.2}$$

where $\varepsilon_0 = 8.854 \cdot 10^{-12}\,\mathrm{F/m}$ and $\mu_0 = 4\pi \cdot 10^{-7}\,\mathrm{H/m}$ are the vacuum permittivity and permeability, respectively. The scalar quantity ε is the dielectric function; in general, it depends on the frequency and the position within the medium.

A basic feature of Maxwell's equations is the existence of traveling wave solutions. We consider a homogeneous, nonmagnetic, linear, and isotropic medium, which can be described by a spatially constant dielectric function ε. We assume ε to be real and positive (lossless medium). Under these assumptions, Maxwell's equations can be combined into well-known Helmholtz's equation, e.g., for the electric field,

$$\nabla^2 \mathbf{E} - \mu_0 \varepsilon_0 \varepsilon \frac{\partial^2 \mathbf{E}}{\partial t^2} = 0. \tag{A.3}$$

The solutions to this equation are monochromatic plane waves of the form

$$\mathbf{E}(\mathbf{r}, t) = \mathbf{E}_0 \exp(\mathrm{i}\mathbf{k} \cdot \mathbf{r} - \mathrm{i}\omega t), \tag{A.4}$$

with amplitude $\mathbf{E}_0$, frequency ω, and wavevector $\mathbf{k}$. The real part is understood to be the physical field. This functional form describes an oscillating field propagating in the direction of $\mathbf{k}$ with phase velocity $v = \omega/k$. The frequency ω is related to the

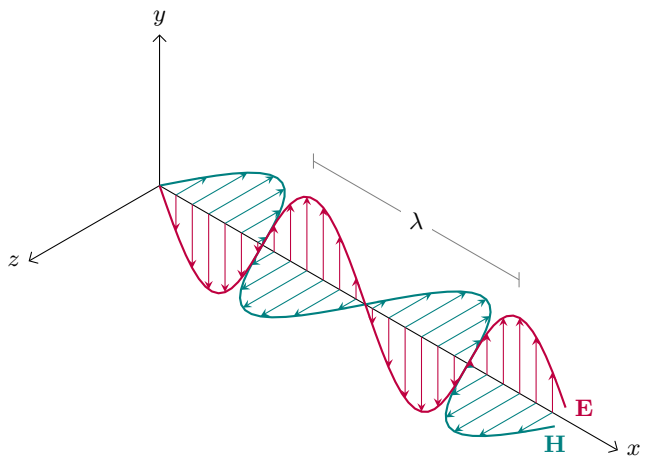

FIGURE A.1. Electric and magnetic fields in an electromagnetic wave.

magnitude of the wavevector **k** by the dispersion relation

$$\omega = \frac{k}{\sqrt{\mu_0 \varepsilon_0 \varepsilon}} = k\frac{c}{n} \qquad \text{whit } n = \sqrt{\varepsilon} \tag{A.5}$$

where n is the refractive index of the medium ($c = 1/\sqrt{\mu_0 \varepsilon_0} = 2.998 \times 10^8$ m/s is the speed of light in vacuum).

The same equations hold when **E** is replaced with **H**. It is easily seen from Maxwell's equations the three vectors **E**, **H**, and **k** are mutually orthogonal. Fig. A.1 illustrates the geometrical form of the plane wave solution.

Electromagnetic waves carry energy. The instantaneous magnitude and direction of the power flow of the electromagnetic field is given by the Poynting vector $\mathbf{S} = \mathbf{E} \times \mathbf{H}$. The optical intensity I (power flow across a unit area normal to **S**) is the magnitude of the time-averaged Poynting vector $\langle S \rangle$.

A.2. Reflection and refraction at the interface of two dielectrics

At the interface of two media of different optical properties, field components must satisfy certain boundary conditions. Namely, the tangential components of **E** and **H** and the normal components of **D** and **B** must be continuous across the interface (Fig. A.2). These can be derived directly from Maxwell's equations.

We now consider the simple case of reflection and refraction at the planar interface of two dielectric media that are linear, isotropic, and lossless, with refractive indices n_1 and n_2, respectively. Using the coordinate system shown in Fig. A.3, the interface lies in the xy plane. Let $\mathbf{E}_1$, $\mathbf{E}'_1$, and $\mathbf{E}_2$ denote the electric fields associated with the incident (from medium 1), reflected, and transmitted waves, respectively. For an incident plane wave, these fields have the form (A.4), where $\mathbf{k}_1$, $\mathbf{k}'_1$, and $\mathbf{k_2}$ denote the incident, reflected, and transmitted wavevectors, respectively. Phase continuity

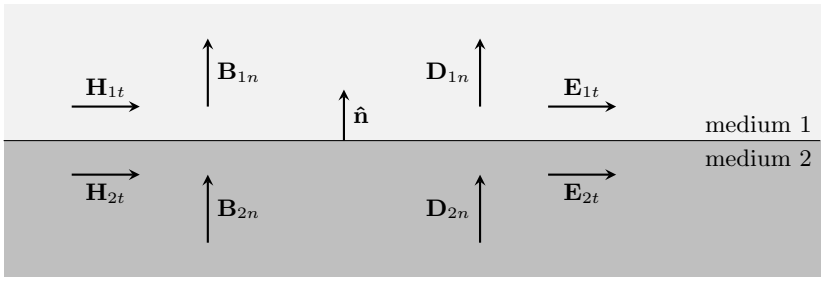

FIGURE A.2. Boundary conditions for optical fields.

at all points along the interface (at all times) implies that the three wavevectors lie in the same plane, known as the plane of incidence (the xz plane). The wavevector components parallel to the interface are conserved: $k_{1x} = k'_{1x} = k_{2x}$. This can be expressed as

$$k_1 \sin\vartheta_1 = k'_1 \sin\vartheta'_1 = k_2 \sin\vartheta_2, \tag{A.6}$$

where ϑ_1, ϑ'_1, and ϑ_2 are the angles of incidence, reflection, and transmission, respectively, as measured with respect to the normal $\hat{\mathbf{n}}$ to the interface. Since $k_1 = k'_1$ and $k_1/k_2 = n_1/n_2$, Eq. (A.6) yields the familiar *law of reflection*

$$\vartheta_1 = \vartheta'_1, \tag{A.7}$$

which indicates that the angle of reflection is equal to the angle of incidence, and *Snell's law of refraction*

$$n_1 \sin\vartheta_1 = n_2 \sin\vartheta_2. \tag{A.8}$$

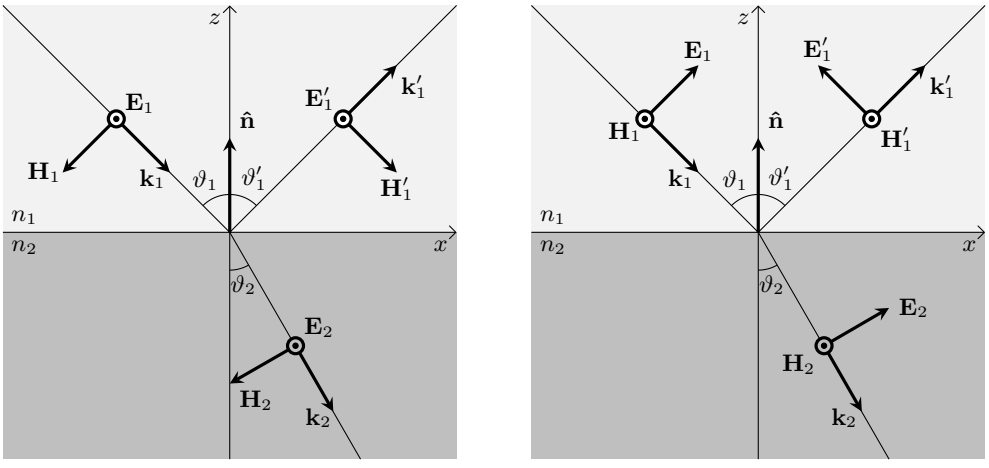

(a) TE polarization (b) TM polarization

FIGURE A.3. Reflection and transmission of (a) TE and (b) TM waves at the planar interface of two isotropic dielectric media (here shown for the case $n_1 < n_2$).

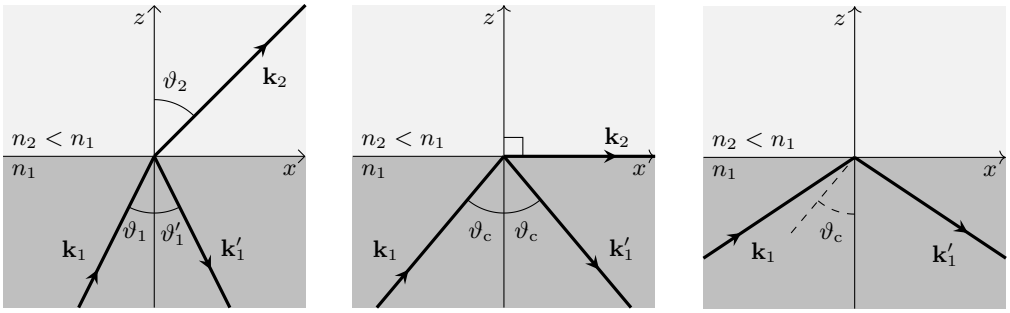

FIGURE A.4. When an optical wave travels from a high-index medium (n_1) to a low-index medium ($n_2 < n_1$), the transmitted wave is bent away from the normal ($\vartheta_2 > \vartheta_1$), according to Snell's law (A.8) (left). When the angle of incidence is equal to the critical angle ϑ_c, the angle of transmission is $\pi/2$ (center). If ϑ_1 is greater than ϑ_c, total internal reflection occurs (right).

Interestingly, when a wave is incident on a rarer medium ($n_2 < n_1$), the incident wave is refracted away from the normal ($\vartheta_2 > \vartheta_1$) in such a way that, as ϑ_1 increases, ϑ_2 reaches $\pi/2$ first (Fig. A.4). This occurs when ϑ_1 is equal to the so-called *critical angle* $\vartheta_c = \arcsin(n_2/n_1)$. At exactly the critical angle, the transmitted wave travels along the interface since $k_{2x} = k_{1x} = k_2$ and $k_{2z} = \sqrt{k_2^2 - k_{2x}^2} = 0$. If light is incident at an angle $\vartheta_1 \geq \vartheta_c$, $k_{2x} = k_{1x} > k_2$ and k_{2z} becomes imaginary: $k_{2z} = \mathrm{i}\gamma$, where γ is real. The propagation of the transmitted wave is thus described by a decreasing exponential $\mathrm{e}^{\mathrm{i}k_{2z}z} = \mathrm{e}^{-\gamma z}$, i.e., an *evanescent wave*, and no energy is transmitted in medium 2. The incident wave is said to be totally reflected, for all of the energy is carried by the reflected wave. This phenomenon is called *total internal reflection* (TIR) and is the basis for guiding light, since for $\vartheta_1 \geq \vartheta_c$ light is restricted to the high-refractive-index medium.

By applying the boundary conditions, one can also determine the reflection coefficient r and transmission coefficient t, defined as the ratio of the reflected and transmitted field amplitudes to the incident field amplitude, respectively,

$$r = \frac{E_1'}{E_1} \quad \text{and} \quad t = \frac{E_2}{E_1}$$

The reflected and transmitted field amplitudes depend on the wave polarization. Every incident plane wave can be resolved into two polarization components: (i) TE (transverse electric) or s polarization, with the electric field perpendicular to the plane of incidence, as shown in Fig. A.3(a), and (ii) TM (transverse magnetic) or p polarization, with the electric field in the plane of incidence, as shown in Fig. A.3(b). As can be seen from symmetry reason, for isotropic dielectrics these two polarizations are preserved upon reflection and refraction, albeit with different reflection and transmission coefficients. We summarize the reflection and transmission coefficients

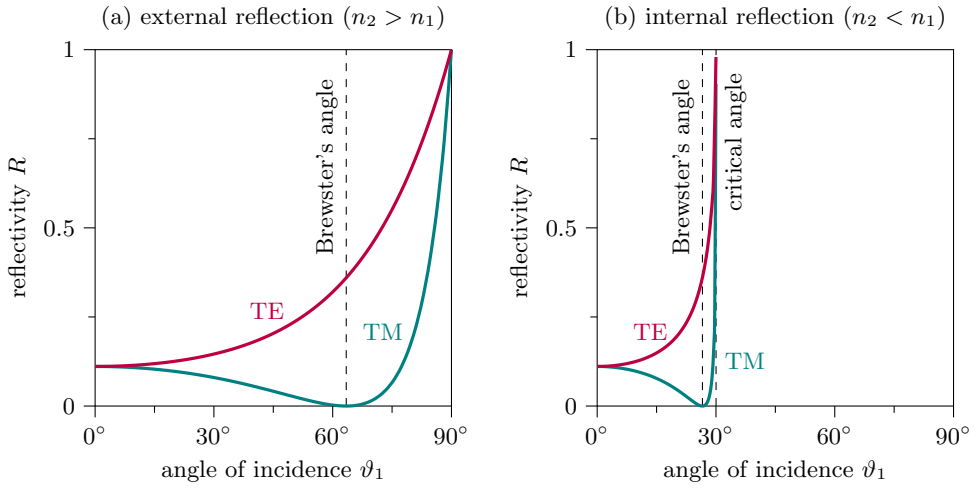

FIGURE A.5. Reflectivity of TE (red) and TM (green) waves at the interface of two lossless, isotropic media as a function of the angle of incidence for (a) external reflection (here shown for $n_1 = 1$ and $n_2 = 2$) and (b) internal reflection (shown for $n_1 = 2$ and $n_2 = 1$).

for the two cases:

$$r_s = \frac{w_1 - w_2}{w_1 + w_2}, \qquad t_s = \frac{2w_1}{w_1 + w_2} = 1 + r_s, \tag{A.9}$$

$$r_p = \frac{n_2^2 w_1 - n_1^2 w_2}{n_2^2 w_1 + n_1^2 w_2} \qquad t_p = \frac{2n_1 n_2 w_1}{n_2^2 w_1 + n_1^2 w_2} = \frac{n_1}{n_2}(1 + r_p), \tag{A.10}$$

where $w_i = k_i \cos\vartheta_i$ is the wavevector component normal to the interface in the medium $i = 1, 2$. These are known as *Fresnel's coefficients*. It is interesting to notice that, in the case of TM polarization, if the angle of incidence is such that $\vartheta_1 = \vartheta_p \equiv \arctan(n_2/n_1)$, called *Brewster's angle*, then $r_p = 0$ and the wave is totally transmitted. In general, for an unpolarized wave incident at an angle $\vartheta_1 = \vartheta_p$, the reflected wave is completely TE polarized.

The reflectivity R and transmissivity T are defined as the ratios of power flow (along a direction normal to the interface) of the reflected and transmitted waves to that of the incident wave,

$$R = \frac{|\mathbf{S}_1' \cdot \hat{\mathbf{n}}|}{|\mathbf{S}_1 \cdot \hat{\mathbf{n}}|} \qquad \text{and} \qquad T = \frac{|\mathbf{S}_2 \cdot \hat{\mathbf{n}}|}{|\mathbf{S}_1 \cdot \hat{\mathbf{n}}|}.$$

In the absence of absorption loss, $T = 1 - R$. Because the incident and reflected waves propagate in the same medium and make the same angle with the normal to the surface, it follows that $R_{s,p} = |r_{s,p}|^2$. On the contrary, $T_{s,p}$ is generally not equal to $|t_{s,p}|^2$ since the incident and transmitted waves travel in different media and at different angles. The reflectivity of TE and TM waves as a function of ϑ_1 is shown in Fig. A.5. It can be seen that, in the case of internal reflection ($n_2 < n_1$), total internal reflection occurs when $\vartheta_1 > \vartheta_c = \arcsin(n_2/n_1)$.

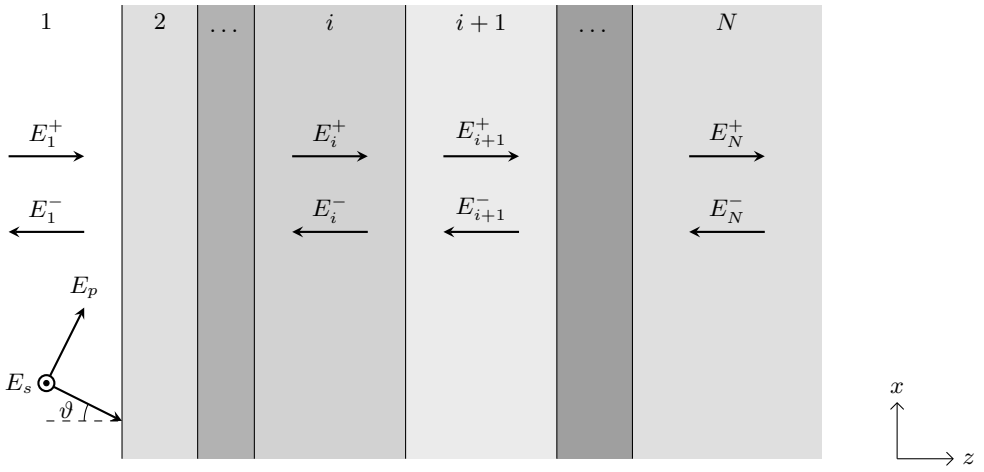

FIGURE A.6. Schematic of a multilayer. $E_i^{\pm}$ indicate the forward and backward propagating amplitudes within layer i.

A.3. Transfer matrix method

For treating an arbitrary number of dielectric layers, the transfer matrix method (TMM) is an extremely useful approach [20]. We consider N layers of thickness d_i and dielectric constant ε_i, with $i = 1, 2, \ldots, N$, stacked along the z direction, as illustrated in Fig. A.6. The plane of incidence is the xz plane. In the case of harmonic time dependence $\mathrm{e}^{-\mathrm{i}\omega t}$, the electric field (for each polarization s or p) at any point within layer i can be written as a superposition of forward and backward propagating waves, i.e.,

$$E_i(\mathbf{r}, t) = [E_i^+ \mathrm{e}^{\mathrm{i}w_i z} + E_i^- \mathrm{e}^{-\mathrm{i}w_i z}]\mathrm{e}^{\mathrm{i}(\beta x - \omega t)}. \tag{A.11}$$

Here, $E_i^{\pm}$ indicate the forward and backward propagating wave amplitudes, respectively; $\beta = k_{ix}$ and $w_i = k_{iz} = \sqrt{k_i^2 - \beta^2}$ are the wavevector components along x and z, respectively, with $k_i = (\omega/c)\sqrt{\varepsilon_i}$. According to (A.6), β is conserved throughout the multilayer (hence we drop the layer index i) and is referred to as the *propagation constant*.

The field components in layer $i+1$ are linked to those in layer i via the relation

$$\begin{pmatrix} E_{i+1}^+ \\ E_{i+1}^- \end{pmatrix} = \mathbf{I}_{i,i+1}\mathbf{\Phi}_i \begin{pmatrix} E_i^+ \\ E_i^- \end{pmatrix}, \tag{A.12}$$

where $\mathbf{\Phi}_i$ is the *propagation matrix*, which accounts for the phase gained by the field components as they propagate within layer i,

$$\mathbf{\Phi}_i = \begin{pmatrix} \mathrm{e}^{\mathrm{i}w_i d_i} & 0 \\ 0 & \mathrm{e}^{-\mathrm{i}w_i d_i} \end{pmatrix}, \tag{A.13}$$

while $\mathbf{I}_{i,i+1}$ is the *interface matrix* from layer i to layer $i+1$, which follows from the continuity conditions for the field components across the interface,

$$\mathbf{I}_{i,i+1} = \frac{1}{t_{i+1,i}} \begin{pmatrix} 1 & r_{i+1,i} \\ r_{i+1,i} & 1 \end{pmatrix}. \tag{A.14}$$

Fresnel's coefficients $r_{i+1,i}$ and $t_{i+1,i}$ depend on the polarization of the incident field according to Eqs. (A.9) and (A.10).

Ordered multiplication of these matrices connects the amplitudes in each layer of the structure. If we carry out the amplitude transfer over the whole multilayer, we obtain

$$\begin{pmatrix} E_N^+ \\ E_N^- \end{pmatrix} = \mathbf{M}_{1,N} \begin{pmatrix} E_1^+ \\ E_1^- \end{pmatrix}, \tag{A.15}$$

where $\mathbf{M}_{1,N}$ is the *transfer matrix* of the whole structure

$$\mathbf{M}_{1,N} = \begin{pmatrix} m_{11} & m_{12} \\ m_{21} & m_{22} \end{pmatrix} = \mathbf{I}_{N-1,N} \mathbf{\Phi}_{N-1} \dots \mathbf{\Phi}_2 \mathbf{I}_{1,2}. \tag{A.16}$$

The transfer matrix of a lossless structure is unimodular, i.e., $\det \mathbf{M}_{1,N} = 1$.

Once the transfer matrix is evaluated, reflection and transmission coefficients are readily derived. Assuming that the field is incident only upon the first layer, we can write

$$\begin{pmatrix} E_N^+ \\ 0 \end{pmatrix} = \begin{pmatrix} m_{11} & m_{12} \\ m_{21} & m_{22} \end{pmatrix} \begin{pmatrix} E_1^+ \\ E_1^- \end{pmatrix}, \tag{A.17}$$

where E_1^+ is the incident field, while E_1^- and E_N^+ are the reflected and transmitted fields, respectively. The reflection and transmission coefficients r and t result

$$r = \frac{E_1^-}{E_1^+} = -\frac{m_{21}}{m_{22}}, \tag{A.18}$$

$$t = \frac{E_N^+}{E_1^+} = \frac{\det \mathbf{M}_{N1}}{m_{22}} = \frac{1}{m_{22}}, \tag{A.19}$$

where the unimodularity of the transfer matrix has been taken into account.

We can also use the transfer matrix to determine the bound modes of the structure by requiring the incoming waves on the first and last layers to vanish, i.e., $E_1^+ = E_N^- = 0$. This results in the following equation

$$\begin{pmatrix} E_N^+ \\ 0 \end{pmatrix} = \begin{pmatrix} m_{11} & m_{12} \\ m_{21} & m_{22} \end{pmatrix} \begin{pmatrix} 0 \\ E_1^- \end{pmatrix}, \tag{A.20}$$

which can be satisfied with nontrivial E_1^- and E_N^+ provided that

$$m_{22} = 0. \tag{A.21}$$

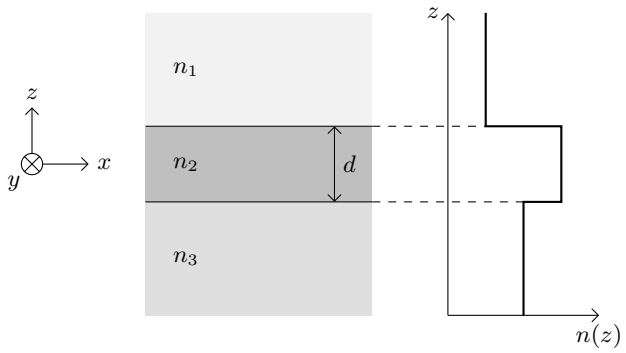

FIGURE A.7. Schematic of a dielectric slab waveguide.

From Eq. (A.18), we see that solving (A.21) is equivalent to studying the poles of the reflection coefficient of the structure.

A.4. Dielectric slab waveguides

We adopt the TMM to obtain the guided modes supported by a dielectric slab waveguide, whose characteristics have been outlined in Chapter 1. In the notation of Fig. A.7, the refractive index depends only on the z coordinate, $n = n(z)$, with $n_2 > n_3 > n_1$. We can always choose the x axis along the direction of propagation of the wave, and write the solutions to Maxwell's equations in the form

$$\mathbf{E}(\mathbf{r}, t) = \mathbf{E}_m(z)\mathrm{e}^{\mathrm{i}\beta x - \mathrm{i}\omega t}, \tag{A.22}$$

where m is the mode index, $\mathbf{E}_m(z)$ is the transverse field profile, and β is the propagation constant of the mode. Before proceeding with a full derivation, it is worth noticing that guided modes correspond to a TIR mechanism: when $k_2 > \beta > k_3 > k_1$, the field components are oscillating within the core and evanescent in the substrate and cladding.

Mirror symmetry with respect to the plane of incidence xz allows one to classify the modes by separating them in two polarizations, according to their parity with respect to the mirror symmetry operator σ_{xz}: (i) TE modes (odd parity, $\sigma_{xz} = -1$), with nonvanishing field components (H_x, E_y, H_z), and (ii) TM modes (even parity, $\sigma_{xz} = 1$), with nonvanishing field components (E_x, H_y, E_z).

The structure transfer matrix can be written as

$$\begin{aligned}
\mathbf{M}_{1,3} &= \mathbf{I}_{2,3}\mathbf{\Phi}_2\mathbf{I}_{1,2} \\
&= \frac{1}{t_{3,2}}\begin{pmatrix} 1 & r_{3,2} \\ r_{3,2} & 1 \end{pmatrix}\begin{pmatrix} \mathrm{e}^{\mathrm{i}w_2 d} & 0 \\ 0 & \mathrm{e}^{-\mathrm{i}w_2 d} \end{pmatrix}\frac{1}{t_{2,1}}\begin{pmatrix} 1 & r_{2,1} \\ r_{2,1} & 1 \end{pmatrix} \\
&= \frac{\mathrm{e}^{-\mathrm{i}w_2 d}}{t_{2,1}t_{3,2}}\begin{pmatrix} r_{2,1}r_{3,2} + \mathrm{e}^{2\mathrm{i}w_2 d} & r_{3,2} + r_{2,1}\mathrm{e}^{2\mathrm{i}w_2 d} \\ r_{2,1} + r_{3,2}\mathrm{e}^{2\mathrm{i}w_2 d} & 1 + r_{2,1}r_{3,2}\mathrm{e}^{2\mathrm{i}w_2 d} \end{pmatrix}
\end{aligned} \tag{A.23}$$

Applying Eq. (A.21) to (A.23) and observing that $r_{3,2} = -r_{2,3}$ gives the condition for the existence of guided modes:

$$1 - r_{2,1} r_{2,3} \mathrm{e}^{2\mathrm{i} w_2 d} = 0. \tag{A.24}$$

In the case of TE modes, from Fresnel's relations (A.9), we can write

$$1 - \frac{w_2 - w_1}{w_2 + w_1} \frac{w_2 - w_3}{w_2 + w_3} \mathrm{e}^{2\mathrm{i} w_2 d_2} = 0. \tag{A.25}$$

For a guided mode, $k_2 > \beta > k_3 > k_1$, so w_2 is real, and w_3 and w_1 are imaginary. Therefore, positive real parameters h_2, q_3, and q_1 exist such that

$$\begin{aligned} w_2 &= h_2 \qquad \text{with} \quad h_2^2 = k_2^2 - \beta^2 \\ w_3 &= \mathrm{i} q_3 \qquad \text{with} \quad q_3^2 = \beta^2 - k_3^2 \\ w_1 &= \mathrm{i} q_1 \qquad \text{with} \quad q_1^2 = \beta^2 - k_1^2 \end{aligned}$$

Eq. (A.25) reads

$$1 - \frac{h_2 - \mathrm{i} q_1}{h_2 + \mathrm{i} q_1} \frac{h_2 - \mathrm{i} q_3}{h_2 + \mathrm{i} q_3} \mathrm{e}^{2\mathrm{i} h_2 d} = 0$$

or, equivalently, with a slight variation,

$$1 + \mathrm{e}^{2\mathrm{i} h_2 d} = 1 + \frac{h_2 + \mathrm{i} q_1}{h_2 - \mathrm{i} q_1} \frac{h_2 + \mathrm{i} q_3}{h_2 - \mathrm{i} q_3}.$$

This leads to

$$\begin{aligned} &1 + \cos(2h_2 d) + \mathrm{i} \sin(2h_2 d) \\ &\qquad = \frac{2(h_2^2 - q_1 q_3)}{(h_2^2 + q_1^2)(h_2^2 + q_3^2)} [(h_2^2 - q_1 q_3) + \mathrm{i} h_2 (q_1 + q_3)]. \end{aligned}$$

By equating the ratio of imaginary to real parts of the LHS to that of the RHS,

$$\frac{\sin(2h_2 d)}{1 + \cos(2h_2 d)} = \frac{h_2 (q_1 + q_3)}{h_2^2 - q_1 q_3},$$

we obtain the well-known eigenvalue equation for the dispersion of TE guided modes in an asymmetric slab waveguide [2]:

$$\tan(h_2 d) = \frac{h_2 (q_1 + q_3)}{h_2^2 - q_1 q_3}. \qquad \text{(TE modes)} \tag{A.26}$$

The solution yields a finite number of allowed values of β. The number of guided modes depends on the core thickness d: the thicker the slab, the larger the number of guided modes. In particular, to support the m-th TE mode (with $m = 0, 1, 2, \dots$), its value of d/λ must be larger than the following cutoff value

$$\left(\frac{d}{\lambda} \right)_{\text{c.o.,TE}} = \frac{1}{2\pi \sqrt{n_2^2 - n_3^2}} \left[m\pi + \arctan \sqrt{\frac{n_3^2 - n_1^2}{n_2^2 - n_3^2}} \right]. \tag{A.27}$$

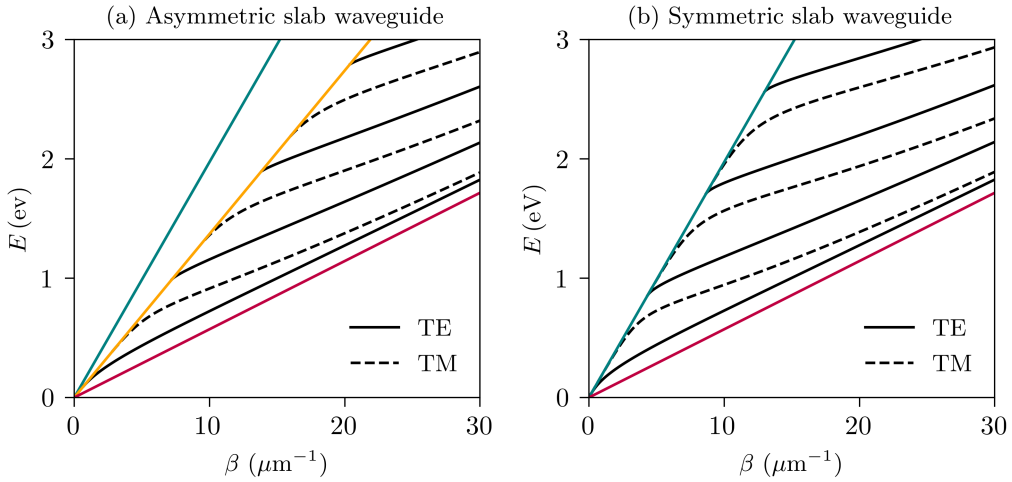

FIGURE A.8. Dispersion curves of TE (solid black) and TM modes (dashed black) supported by (a) asymmetric air-silicon-silica and (b) symmetric air-silicon-air slab waveguide of thickness $d = 220\,\text{nm}$. Lightlines of air ($n_1 = 1$) (green), silicon ($n = 3.45$) (red), and silica ($n_3 = 1.44$) (orange) are indicated. Chromatic dispersion is neglected.

A similar derivation holds for TM modes, for which the eigenvalue equation is

$$\tan(h_2 d) = \frac{(h_2/n_2^2)(q_1/n_1^2 + q_3/n_3^2)}{(h_2/n_2^2)^2 - (q_1/n_1^2)(q_3/n_3^2)}, \qquad \text{(TM modes)} \tag{A.28}$$

with cutoff condition

$$\left(\frac{d}{\lambda}\right)_{\text{c.o.,TM}} = \frac{1}{2\pi\sqrt{n_2^2 - n_3^2}}\left[m\pi + \arctan\frac{n_2^2}{n_1^2}\sqrt{\frac{n_3^2 - n_1^2}{n_2^2 - n_3^2}}\right]. \tag{A.29}$$

As an example, Fig. A.8(a) shows the dispersion of guided TE and TM modes for an asymmetric slab waveguide made of a silicon core ($n_2 = 3.45$) of thickness $d = 1\,\mu\text{m}$ deposited on a silica substrate ($n_3 = 1.44$); the cover is air ($n_1 = 1$). We notice that the dispersion relation for the different guided modes lie between the lightlines $\omega = c\beta/n_2$ and $\omega = c\beta/n_3$, i.e., in the region where TIR within the core is ensured. For a given guided mode with propagation constant β, it is useful to define the *effective mode index* n_{eff} via the relation $\omega = c\beta/n_{\text{eff}}$. With respect to the mode propagation, the slab waveguide can be treated as an effective homogeneous medium with refractive index n_{eff}.

A special case of a slab waveguide occurs when the substrate and cover consist of the same medium, $n_1 = n_3$. In this case, the mirror symmetry with respect to the slab midplane xy allows one to further classify the modes as even ($\sigma_{xy} = 1$) or odd ($\sigma_{xy} = -1$). By equating q_1 to q_3, the eigenvalue equation (A.26) for TE modes can

be cast in the following two equations

$$\tan\frac{h_2 d}{2} = \frac{q_1}{h_2}, \qquad \text{(TE even modes)} \tag{A.30}$$

$$-\cot\frac{h_2 d}{2} = \frac{q_1}{h_2}. \qquad \text{(TE odd modes)} \tag{A.31}$$

Similarly, Eq. (A.28) can be transformed to

$$\tan\frac{h_2 d}{2} = \frac{n_2^2}{n_1^2}\frac{q_1}{h_2}, \qquad \text{(TM even modes)} \tag{A.32}$$

$$-\cot\frac{h_2 d}{2} = \frac{n_2^2}{n_1^2}\frac{q_1}{h_2}. \qquad \text{(TM odd modes)} \tag{A.33}$$

As can be seen from Eqs. (A.27) and (A.29), in the symmetric case both fundamental TE and TM modes ($m = 0$) have no cutoff and are guided for all values of d/λ. Thus, any symmetric slab waveguide supports at least one TE and one TM mode. An example is illustrated in Fig. A.8(b).

A.5. Fourier transform via transfer matrix method

The electric field spatial Fourier transform (FT) is defined as follows:

$$\widetilde{E}(k) = \int \mathrm{Re}(E(z))\mathrm{e}^{-2\pi\mathrm{i}kz}\,\mathrm{d}z = \frac{1}{2}\int [E(z) + E^*(z)]\mathrm{e}^{-2\pi\mathrm{i}kz}\,\mathrm{d}z\,. \tag{A.34}$$

Here we show that, when the electric field is determined by means of the TMM, the FT can be computed semi-analytically. We consider the usual multilayer of Fig. A.6 composed by N layers of thickness d_i and refractive index n_i, with $i = 1, 2, \ldots, N$. By introducing the cumulative thickness $z_i = \sum_{j=0}^{i} d_j$, where we set $d_0 = 0$, we can write the integral in (A.34) as follows:

$$\widetilde{E}(k) = \sum_{i=0}^{N-1}\int_{z_i}^{z_{i+1}} \frac{1}{2}[E(z) + E^*(z)]\mathrm{e}^{-2\pi\mathrm{i}kz}\,\mathrm{d}z\,. \tag{A.35}$$

Within each layer, the electric field can be expressed as the combination of forward and backward waves in the form of Eq. (A.11). After change of the spatial variable $z \to z - z_j$ and some rearrangement, we obtain

$$\begin{aligned}
\widetilde{E}(k) &= \sum_{i=0}^{N-1}\int_0^{d_i} \frac{1}{2}\big[(E_i^+ + E_i^{-*})\mathrm{e}^{\mathrm{i}w_i z} + (E_i^- + E_i^{+*})\mathrm{e}^{-\mathrm{i}w_i z}\big]\mathrm{e}^{-2\pi\mathrm{i}k(z+z_j)}\,\mathrm{d}z \\
&= \sum_{i=0}^{N-1}\mathrm{e}^{-2\pi\mathrm{i}kz_i}\int_0^{d_i} \frac{1}{2}\big[(E_i^+ + E_i^{-*})\mathrm{e}^{\mathrm{i}w_i z} + (E_i^- + E_i^{+*})\mathrm{e}^{-\mathrm{i}w_i z}\big]\mathrm{e}^{-2\pi\mathrm{i}kz}\,\mathrm{d}z \\
&= \sum_{i=0}^{N-1}\mathrm{e}^{-2\pi\mathrm{i}kz_i}\widetilde{E}_i(k),
\end{aligned} \tag{A.36}$$

with obvious notation. Calculation of $\widetilde{E}_i(k)$ in (A.36) can be performed analytically:

$$\begin{aligned}\widetilde{E}_i(k) &= \int_0^{d_i} \frac{1}{2}\Big[(E_i^+ + E_i^{-*})\mathrm{e}^{\mathrm{i}(w_i-2\pi k)z} + (E_i^- + E_i^{+*})\mathrm{e}^{-\mathrm{i}(w_i+2\pi k)z}\Big]\,\mathrm{d}z \\ &= \frac{1}{2}\frac{\mathrm{i}(E_i^+ + E_i^{-*})}{w_i - 2\pi k}\Big[1 - \mathrm{e}^{\mathrm{i}(w_i-2\pi k)d_i}\Big] \\ &\quad - \frac{1}{2}\frac{\mathrm{i}(E_i^- + E_i^{+*})}{w_i + 2\pi k}\Big[1 - \mathrm{e}^{-\mathrm{i}(w_i+2\pi k)d_i}\Big]. \end{aligned} \tag{A.37}$$

Hence, the FT of the overall electric field can be determined directly from the TMM-calculated amplitudes (E_i^+, E_i^-).

A.6. Dielectric ridge waveguides: effective index method

A *ridge waveguide*, shown in Fig. A.9 (left), is formed by loading a planar slab (the substrate) with a high-refractive-index strip of width w and height d that serves as guiding core (the ridge). The ridge is surrounded on three sides by a low-refractive-index cladding, which provides optical confinement in both transverse directions. If the ridge is infinitely wide, the problem reduces to a 1D asymmetric slab waveguide, for which the guided modes can be classified as TE or TM polarized. If the ridge has a finite width w, the existence of purely TE or TM modes is not possible because the two transverse field components E_y, E_z are coupled by the boundary conditions at the dielectric interfaces given by $n = n(y, z)$. Thus, in general, all six electromagnetic field components are nonvanishing. However, the modes can sometimes be labeled as TE-like or TM-like, in that E_y or H_y is the dominant field component, respectively.

Since an analytical treatment is not feasible, one is interested in obtaining approximate solutions that give the guided mode characteristics. One of the simplest, yet most useful, approximate approaches is the effective index method (EIM). The basic concept of the EIM is to replace the 2D ridge waveguide with a combination of 1D slab waveguides, as illustrated in Fig. A.9. First, one considers the symmetric slab waveguide of width w that corresponds to the horizontal cross section of the layer containing the ridge (waveguide I: cladding/ridge/cladding), and calculates the effective index $n_{\mathrm{eff,I}}$ of the supported guided mode. Second, one substitutes the ridge region with a uniform layer of height h having refractive index $n_{\mathrm{eff,I}}$, and looks for the mode supported by the effective asymmetric slab waveguide (waveguide II: cladding/effective ridge/substrate). It should be noticed that, for a TE-like (TM-like) mode of the 2D ridge waveguide, one first does the TM (TE) mode analysis of waveguide I and then the TE (TM) mode analysis of waveguide II.

This approach offers an advantage in terms of computational time and resources to calculating the dispersion relation and field distribution, but at the same time is not able to capture all the physics of light propagation, for instance, the group index or propagation loss.

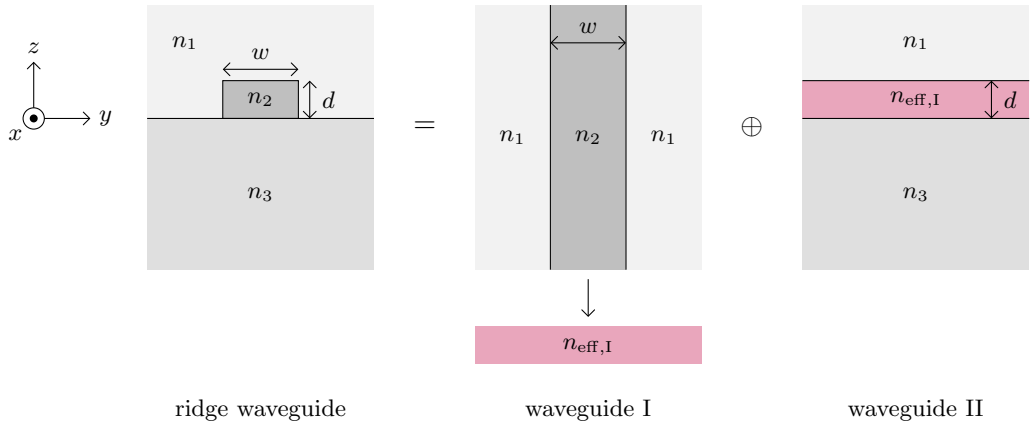

FIGURE A.9. Concept of the effective index method applied to a ridge waveguide ($n_2 > n_3 > n_1$).

A.7. Photonic crystals

Photonic crystals (PhCs) are media displaying a spatial periodicity in their dielectric function. The description of light propagation in PhCs begins with Maxwell's equations (A.1). If we assume nonmagnetic media, $\mu = \mu_0$, and harmonic time dependence, Maxwell's equations can be cast into a second-order differential equation for the electric field,

$$\nabla \times \nabla \times \mathbf{E} = \frac{\omega^2}{c^2}\varepsilon(\mathbf{r})\mathbf{E}(\mathbf{r}) \qquad \text{with} \quad \nabla \cdot [\varepsilon(\mathbf{r})\mathbf{E}(\mathbf{r})] = 0 \tag{A.38}$$

or an analogous one for the magnetic field,

$$\nabla \times \left[\frac{1}{\varepsilon(\mathbf{r})}\nabla \times \mathbf{H}(\mathbf{r})\right] = \frac{\omega^2}{c^2}\mathbf{H}(\mathbf{r}) \qquad \text{with} \quad \nabla \cdot \mathbf{H}(\mathbf{r}) = 0. \tag{A.39}$$

The latter of these equations is usually taken as the starting point for computing the photonic band structure since it can be cast in the form of an eigenvalue problem:

$$\Theta\mathbf{H}(\mathbf{r}) = \frac{\omega^2}{c^2}\mathbf{H} \qquad \text{with} \quad \Theta = \nabla \times \left[\frac{1}{\varepsilon(\mathbf{r})}\nabla\times\right]. \tag{A.40}$$

It can be shown that Θ is self-adjoint, thus Eq. (A.40) has real eigenvalues $(\omega/c)^2$ and one can find a set of orthonormal eigenmodes. Such a problem has strong analogies with the matrix formulation of quantum mechanics. However, it is worthwhile to point out that the linear operator Θ does not correspond to the energy observable (as a purely formal analogy with Schrödinger's equation might suggest). It is also interesting to notice that the dielectric function $\varepsilon(\mathbf{r})$ appears in the denominator of Θ. Thus, modes corresponding to lower eigenvalues tend to concentrate their energy in high-permittivity regions (unlike in quantum mechanics, where the lower eigenstates typically have their amplitude concentrated in regions of low potential).

One important feature of Eq. (A.40) is its scale invariance, provided the material chromatic dispersion can be neglected. By reducing the length scale by a factor s ($\mathbf{r} \to \mathbf{r}/s$), the eigenmodes are unchanged while the eigenfrequencies are all scaled by a factor s ($\omega \to s\omega$). Thus, there is no fundamental length scale for the photonic problem (other than the assumption that the medium is macroscopic) unlike the electronic problem, for which the Bohr radius is the natural unit length. In particular, if one scales down the coordinates by s and also the dielectric constant ε by s^2, the eigenfrequencies are unchanged. As a consequence, in a structure made up of only two different dielectric media of permittivity ε_1 and ε_2, its photonic properties only depend on the dielectric contrast $\varepsilon_1/\varepsilon_2$. Scale invariance proves to be quite useful in practice, since one can create a magnified PhC structure that is more easily fabricated and characterized, and later scale it down to operate in the desired spectral region.

A PhC is invariant under translation by vectors $\mathbf{R} = m_1\mathbf{a}_1 + m_2\mathbf{a}_2 + m_3\mathbf{a}_3$, where $\mathbf{a}_1, \mathbf{a}_2, \mathbf{a}_3$ are non-coplanar vectors (primitive vectors) and m_1, m_2, m_3 are integer numbers. All translation vectors $\mathbf{R}$ form a Bravais lattice. The dielectric constant satisfies the relation

$$\varepsilon(\mathbf{r} + \mathbf{R}) = \varepsilon(\mathbf{r}), \tag{A.41}$$

and the magnetic field has the form implied by Bloch's theorem

$$\mathbf{H}_{m\mathbf{k}}(\mathbf{r}) = e^{i\mathbf{k}\cdot\mathbf{r}}\mathbf{u}_{m\mathbf{k}}(\mathbf{r}), \tag{A.42}$$

where $\mathbf{u}_{m\mathbf{k}}(\mathbf{r} + \mathbf{R}) = \mathbf{u}_{m\mathbf{k}}(\mathbf{r})$ is a periodic function, m is a discrete band index, and $\mathbf{k}$ is the Bloch vector (which may be restricted to the first Brillouin zone). The fundamental Eq. (A.39) can be expressed in terms of the periodic component $\mathbf{u}_{m\mathbf{k}}$:

$$(i\mathbf{k} + \nabla) \times \left[\frac{1}{\varepsilon(\mathbf{r})}(i\mathbf{k} + \nabla) \times \mathbf{u}_{m\mathbf{k}}(\mathbf{r})\right] = \frac{\omega_m^2(\mathbf{k})}{c^2}\mathbf{u}_{m\mathbf{k}}(\mathbf{r}), \tag{A.43}$$

with the further condition that $(i\mathbf{k} + \nabla) \cdot \mathbf{u}_{m\mathbf{k}}(\mathbf{r}) = 0$. The eigenvalues $\omega = \omega_m(\mathbf{k})$ of Eq. (A.43), for each $\mathbf{k}$ within the first Brillouin zone, describe the band structure of the system, which consists of allowed frequency regions (photonic bands) separated by forbidden frequency regions (PBGs). Except for the 1D case, numerical techniques have to be invoked to solve Eq. (A.43), e.g., plane-wave expansion (PWE), rigorous coupled-wave analysis (RCWA), and finite-different time-domain (FDTD) method.

A.8. 1D photonic crystals

The photonic band structure of a 1D PhC is conveniently calculated by means of the TMM. We consider an infinite number of planar layers of two or more different materials stacked with a certain period Λ along a given direction, say z, as illustrated in Fig. A.10(a). For each polarization, the electric fields takes the form $E(x, z, t) = E(z)\mathrm{e}^{\mathrm{i}\beta x - \mathrm{i}\omega t}$, where β is the propagation constant. According to Eq. (A.11), let $E_0^{\pm}$

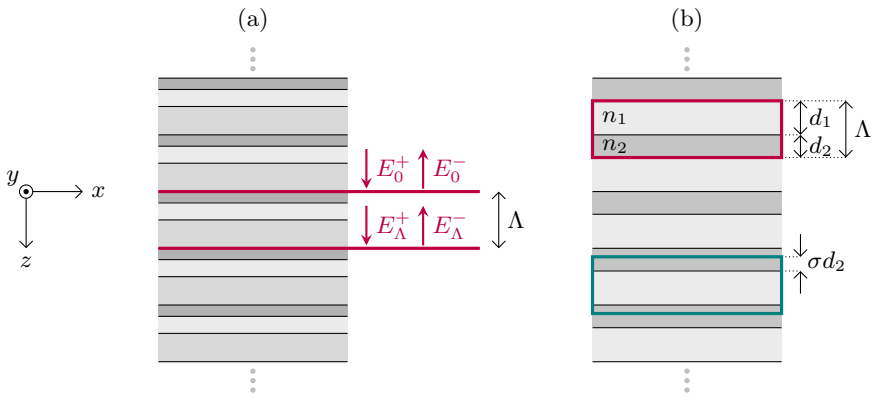

FIGURE A.10. (a) Notation used in the TMM analysis of 1D PhCs. (b) Different choices of unit cell for a 1D PhC composed of two alternating layers of thicknesses d_1, d_2 and refractive indices n_1, n_2.

be the forward and backward components at the beginning of a generic unit cell. After propagating through a period Λ, the amplitudes $E_\Lambda^\pm$ are given by

$$\begin{pmatrix} E_\Lambda^+ \\ E_\Lambda^- \end{pmatrix} = \mathbf{M}_\Lambda \begin{pmatrix} E_0^+ \\ E_0^- \end{pmatrix}. \tag{A.44}$$

where $\mathbf{M}_\Lambda$ is the (polarization-dependent) transfer matrix associated with the unit cell. As stated by Bloch's theorem, the electric field must be invariant up to a phase factor $\mathrm{e}^{\mathrm{i}q\Lambda}$ when translating over a period Λ, i.e., $E(z+\Lambda) = \mathrm{e}^{\mathrm{i}q\Lambda}E(z)$, where q is the Bloch wavevector. Thus, we look for amplitudes $E_\Lambda^\pm$ that satisfy

$$\begin{pmatrix} E_\Lambda^+ \\ E_\Lambda^- \end{pmatrix} = \mathrm{e}^{\mathrm{i}q\Lambda} \begin{pmatrix} E_0^+ \\ E_0^- \end{pmatrix}. \tag{A.45}$$

Application of (A.45) to (A.44) leads to

$$\mathbf{M}_\Lambda \begin{pmatrix} E_0^+ \\ E_0^- \end{pmatrix} = \mathrm{e}^{\mathrm{i}q\Lambda} \begin{pmatrix} E_0^+ \\ E_0^- \end{pmatrix}. \tag{A.46}$$

This is an eigenvalue problem for the unit-cell transfer matrix $\mathbf{M}_\Lambda$. Due to its unimodularity, the eigenvalues of $\mathbf{M}_\Lambda$ have to be $\lambda_{1,2} = \mathrm{e}^{\pm\mathrm{i}q\Lambda}$. For the trace of a matrix is invariant upon diagonalization, we obtain the following compatibility equation

$$\operatorname{tr}\mathbf{M}_\Lambda = \lambda_1 + \lambda_2 = \mathrm{e}^{\mathrm{i}q\Lambda} + \mathrm{e}^{-\mathrm{i}q\Lambda} = 2\cos(q\Lambda). \tag{A.47}$$

Since $\cos(q\Lambda)$ is bounded in the range $[-1, 1]$, solutions cannot exist when $|\operatorname{tr}\mathbf{M}_\Lambda|/2$ is larger than unity. The nonexistence of solutions gives rise to the formation of the PBGs. In the particular case of a 1D PhC with a unit cell composed of two layers of thickness d_1 and d_2, and refractive indices n_1 and n_2, respectively, the transfer matrix reads

$$\mathbf{M}_\Lambda = \mathbf{\Phi}_2\mathbf{I}_{1,2}\mathbf{\Phi}_1\mathbf{I}_{2,1}. \tag{A.48}$$

Here, the unit cell is chosen in such a way that it begins just on the d_1 side of an interface and finishes one lattice period $\Lambda = d_1 + d_2$ away (Fig. A.10(b) (solid red)). The compatibility equation (A.47) can be cast in the form of the implicit equation (1.1), as illustrated in Chapter 1.

Following [40], we now consider a less intuitive choice of a unit cell that begins with a layer of thickness σd_2, where $\sigma \in [0, 1]$ (Fig. A.10(b) (solid green)). The transfer matrix associated with this unit cell is

$$\mathbf{M}_\sigma = \mathbf{\Phi}_\sigma^{-1}\mathbf{\Phi}_2\mathbf{I}_{1,2}\mathbf{\Phi}_1\mathbf{I}_{2,1}\mathbf{\Phi}_\sigma = \mathbf{\Phi}_\sigma^{-1}\mathbf{M}_\Lambda\mathbf{\Phi}_\sigma, \tag{A.49}$$

where $\mathbf{M}_\Lambda$ is given by (A.48) and $\mathbf{\Phi}_\sigma = \mathrm{diag}(\mathrm{e}^{\mathrm{i}w_2\sigma d_2}, \mathrm{e}^{-\mathrm{i}w_2\sigma d_2})$ is the propagation matrix in the layer of thickness σd_2. Since $\mathbf{\Phi}_\sigma$ is invertible, matrices $\mathbf{M}_\Lambda$ and $\mathbf{M}_\sigma$ are similar. Matrices related by similarity represent the same linear transformation under two different bases, with $\mathbf{\Phi}_\sigma$ being the change-of-basis matrix. Similar matrices have invariant eigenvalues, trace, and determinant. This is physically understandable since the photonic band structrure is a bulk property of a PhC, which depends only on the eigenvalues of the transfer matrix by means of the compatibility equation (A.47) and is independent of the particular choice of a basis, i.e., of a unit cell. Bloch's theorem clearly holds with this choice of unit cell as well, namely,

$$\mathbf{M}_\sigma \begin{pmatrix} E_\sigma^+ \\ E_\sigma^- \end{pmatrix} = \mathbf{\Phi}_\sigma^{-1}\mathbf{M}_\Lambda\mathbf{\Phi}_\sigma \begin{pmatrix} E_\sigma^+ \\ E_\sigma^- \end{pmatrix} = \mathrm{e}^{\mathrm{i}q\Lambda} \begin{pmatrix} E_\sigma^+ \\ E_\sigma^- \end{pmatrix}, \tag{A.50}$$

where, by comparison with (A.46),

$$\begin{pmatrix} E_\sigma^+ \\ E_\sigma^- \end{pmatrix} = \mathbf{\Phi}_\sigma^{-1} \begin{pmatrix} E_0^+ \\ E_0^- \end{pmatrix} = \begin{pmatrix} \mathrm{e}^{-\mathrm{i}w_2\sigma d_2}E_0^+ \\ \mathrm{e}^{\mathrm{i}w_2\sigma d_2}E_0^- \end{pmatrix}. \tag{A.51}$$

This choice of a unit cell is suited to describing a truncated periodic multilayer, for it naturally takes into account the presence of a truncation layer of thickness σd_2. The external homogeneous dielectric media has refractive index n_{ext}. As discussed in Chapter 1, the addition of such termination on top of the periodic structure gives rise to Bloch surface waves (BSW). Because of TIR from the external medium, the BSW dispersion relation can be determined by applying the continuity of the tangential field components at the truncation interface in the absence of incident field from the external medium:

$$\begin{pmatrix} 0 \\ E_{\mathrm{ext}}^- \end{pmatrix} = \mathbf{I}_{2,\mathrm{ext}} \begin{pmatrix} E_\sigma^+ \\ E_\sigma^- \end{pmatrix} = \frac{1}{t_{\mathrm{ext},2}} \begin{pmatrix} 1 & r_{\mathrm{ext},2} \\ r_{\mathrm{ext},2} & 1 \end{pmatrix} \begin{pmatrix} E_\sigma^+ \\ E_\sigma^- \end{pmatrix} \tag{A.52}$$

From Eq. (A.52), we obtain $E_\sigma^+ + r_{\mathrm{ext},2}E_\sigma^- = 0$ or, by recalling that $r_{\mathrm{ext},2} = -r_{2,\mathrm{ext}}$,

$$r_{2,\mathrm{ext}} = \frac{E_\sigma^+}{E_\sigma^-} = \frac{E_0^+}{E_0^-}\mathrm{e}^{-2\mathrm{i}w_2\sigma d_2}, \tag{A.53}$$

where we used Eq. (A.51). Bloch's theorem (A.46) entails $E_0^- = E_0^+(\mathrm{e}^{\mathrm{i}q\Lambda} - m_{11})/m_{12}$, where m_{11} and m_{12} are the (polarization-dependent) matrix elements of $\mathbf{M}_\Lambda$ and can be found by expanding $\mathbf{M}_\Lambda$ in the form of (A.48). The Bloch wavevector q has nonzero imaginary part on account of the field exponential decay in the PhC. Thus, Eq. (A.53) reads

$$r_{2,\mathrm{ext}} = \frac{m_{12}}{\mathrm{e}^{\mathrm{i}q\Lambda} - m_{11}} \mathrm{e}^{-2\mathrm{i}w_2\sigma d_2}. \tag{A.54}$$

We can now specify the reflection coefficient $r_{2,\mathrm{ext}}$ by means of Fresnel's relations (A.9) and (A.10):

$$r_{2,\mathrm{ext}} = \frac{pw_2 - w_{\mathrm{ext}}}{pw_2 + w_{\mathrm{ext}}} = \frac{pw_2 - \mathrm{i}q_{\mathrm{ext}}}{pw_2 + \mathrm{i}q_{\mathrm{ext}}}, \tag{A.55}$$

where the transverse wavevector component in the external medium is purely imaginary owing to the evanescent nature of the field, i.e., $w_{\mathrm{ext}} = \mathrm{i}q_{\mathrm{ext}}$, with $q_{\mathrm{ext}} \in \mathbb{R}$. The parameter $p = 1$ for s polarization and $p = n_{\mathrm{ext}}^2/n_2^2$ for p polarization. By equating (A.54) and (A.55), we can determine the truncation factor σ:

$$\sigma = \frac{\mathrm{i}}{2w_2 d_2} \ln\left(\frac{e^{\mathrm{i}q\Lambda} - m_{11}}{m_{12}} \frac{pw_2 - \mathrm{i}q_{\mathrm{ext}}}{pw_2 + \mathrm{i}q_{\mathrm{ext}}} \right) \tag{A.56}$$

Once the Bloch wavevector q is chosen such that its imaginary part is maximized, the truncation layer width can be calculated by evaluating the parameter σ according to Eq. (A.56).

A.9. Finite-difference time-domain method

The finite-difference time-domain (FDTD) method is a widely known numerical technique that discretizes the electromagnetic fields in both space and time to solve Maxwell's equations. In particular, assuming nonmagnetic, linear media free of sources, the curl Maxwell's equations in (A.1) can be written as

$$\frac{\partial \mathbf{E}}{\partial t} = \frac{1}{\varepsilon} \nabla \times \mathbf{H}, \qquad \frac{\partial \mathbf{H}}{\partial t} = -\frac{1}{\mu_0} \nabla \times \mathbf{E}, \tag{A.57}$$

where we made use of the constitutive relations (A.2). The FDTD method as first introduced by Yee in 1966 employs a second-order central-difference approximation in both space and time, with $\mathbf{E}$ and $\mathbf{H}$ displayed on a staggered grid [175]. In order to briefly introduce Yee's discretization, we consider the simple 1D case ($\partial/\partial z \neq 0$) using only E_x, H_y. Eqs. (A.57) become

$$\frac{\partial E_x}{\partial t} = -\frac{1}{\varepsilon} \frac{\partial H_y}{\partial z}, \qquad \frac{\partial H_y}{\partial t} = -\frac{1}{\mu_0} \frac{\partial E_x}{\partial z}. \tag{A.58}$$

We introduce the following notation

$$(E_x)_i^n = E_x(i\Delta z, n\Delta t), \qquad (H_y)_i^n = H_y(i\Delta z, n\Delta t). \tag{A.59}$$

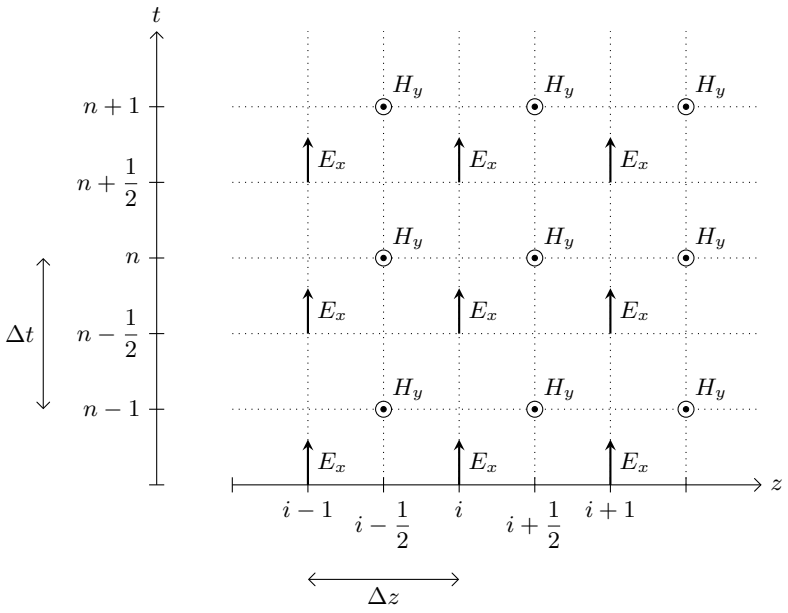

FIGURE A.11. Visual illustratuon of the space-time interdependence of E_x and H_y at different grid points in 1D Yee's cell. Adapted from [174].

Here, Δz and Δt are the space and time sampling intervals, respectively, with n and i being the space and time steps. In Yee's algorithm, E_x and H_y are interleaved in the space and time grid at intervals $\Delta z/2$ and $\Delta t/2$. For instance, at time $t = 0$, values of H_y are placed at $x = (i+1/2)\Delta x$; at time $t = \Delta t/2$, values of E_x are placed at $x = i\Delta z$, and so on. This is illustrated in Fig. A.11.

Taking the central-difference approximations for both space and time derivatives in (A.58) gives

$$\frac{(E_x)_i^{n+1/2} - (E_x)_i^{n-1/2}}{\Delta t} = -\frac{1}{\varepsilon_i}\frac{(H_y)_{i+1/2}^n - (H_y)_{i-1/2}^n}{\Delta z}, \tag{A.60}$$

$$\frac{(H_y)_{i+1/2}^{n+1} - (H_y)_{i+1/2}^n}{\Delta t} = -\frac{1}{\mu_0}\frac{(E_x)_{i+1}^{n+1/2} - (E_x)_i^{n+1/2}}{\Delta z}. \tag{A.61}$$

Assuming that the values of the field components for n and $n-1/2$ have already been stored, the only unknown components remain those for $n + 1/2$:

$$(E_x)_i^{n+1/2} = (E_x)_i^{n-1/2} - \frac{1}{\varepsilon_i}\frac{(H_y)_{i+1/2}^n - (H_y)_{i-1/2}^n}{\Delta z/\Delta t}, \tag{A.62}$$

$$(H_y)_{i+1/2}^{n+1} = (H_y)_{i+1/2}^n - \frac{1}{\mu_0}\frac{(E_x)_{i+1}^{n+1/2} - (E_x)_i^{n+1/2}}{\Delta z/\Delta t}. \tag{A.63}$$

Hence, these equations update the fields by moving them one half time-step forward. It can be seen that the value of a field at a given node in the grid is determined by three previous values: one from the same field at a previous single time-step, and two

from two neighboring opposite fields at a previous half time-step. To ensure numerical stability, Courant's condition should be satisfied: $\Delta z/\Delta x \geq c/n_{\min}$, where $n_{\min}$ is the lowest refractive index of any dielectric element in the computational domain.

This "leap-frog" scheme can be extended to 2D and 3D cases, and guarantees Yee's algorithm its second-order accuracy. We notice that finite-sized simulations require the challenging implementation of absorbing boundary conditions to suppress the spurious reflections at the boundaries back into the simulation domain. One possible solution to this issue is using perfectly matched layers (PMLs), i.e., thin nonphysical layers that enclose the boundaries and anisotropically absorb the outgoing waves, thus enabling the simulation of free-field conditions. For more details, the reader is referred to [176].

For the present work, we use a commercial FDTD software, Ansys/Lumerical FDTD Solutions, which provides the users with Python-based scripting capability, post-processing features (e.g., Q factor analysis), and advanced optimization routines.

List of publications

Peer-reviewed journals

- T. Perani and M. Liscidini. "Long-range Bloch surfaces waves in photonic crystal ridges". In: *Opt. Lett.* 45.23 (2020), pp. 6534–6537. DOI: 10.1364/OL.412625
- T. Perani, D. Aurelio, and M. Liscidini. "Bloch-surface-wave photonic crystal nanobeam cavity". In: *Opt. Lett.* 44.21 (2019), pp. 5133–5136. DOI: 10.1364/OL.44.005133

Conference proceedings

- T. Perani and M. Liscidini. "Hybrid confinement of visible light in a nanophotonic resonators". In: *EPJ Web of Conferences* 255, 04003 (2021). DOI: 10.1051/epjconf/202125504003
- D. Aurelio, T. Perani, and M. Liscidini. "Light confinement in resonators based on Bloch surface waves". In: *2018 20th International Conference on Transparent Optical Networks (ICTON)* (2018), pp. 1–3. DOI: 10.1109/ICTON.2018.8473963

Conferences, workshops and schools

- T. Perani and M. Liscidini. "Hybrid confinement of visible light in a nanophotonic resonator". *2021 European Optical Society Annual Meeting (EOSAM)* (2021). Rome, Italy (contributed talk).
- T. Perani and M. Liscidini. "Bloch-surface-wave nanobeam cavity". *2020 Conference on Lasers and Electro-Optics (CLEO)* (2020). San Jose, USA (poster).
- T. Perani and M. Liscidini. "Bloch-surface-wave photonic crystal nanobeam cavity". *Quantum devices for non-classical light generation and manipulation Graduate Summer School* (2019). Erice, Italy (poster).

Bibliography

[1] J. D. Jackson. *Classical Electrodynamics*. 3rd ed. John Wiley & Sons, 1999.

[2] A. Yariv and P. Yeh. *Photonics: Optical Electronics in Modern Communications*. 6th ed. The Oxford Series in Electrical and Computer Engineering. Oxford University Press, 2006.

[3] M. C. Teich B. E. A. Saleh. *Fundamentals of Photonics Fundamentals of Photonics*. Wiley Series in Pure and Applied Optics. Wiley, 2002.

[4] A. Yariv and P. Yeh. *Optical Waves in Crystals: Propagation and Control of Laser Radiation*. Wiley Series in Pure and Applied Optics. Wiley, 2002.

[5] J. W. Strutt (Lord Rayleigh). "On the maintenance of vibrations by forces of double frequency, and on the propagation of waves through a medium endowed with a periodic structure". In: *Philos. Mag.* 24.147 (1887), pp. 145–159. DOI: 10.1080/14786448708628074.

[6] E. Yablonovitch. "Inhibited Spontaneous Emission in Solid-State Physics and Electronics". In: *Phys. Rev. Lett.* 58 (20 1987), pp. 2059–2062. DOI: 10.1103/PhysRevLett.58.2059.

[7] S. John. "Strong localization of photons in certain disordered dielectric superlattices". In: *Phys. Rev. Lett.* 58 (23 1987), pp. 2486–2489. DOI: 10.1103/PhysRevLett.58.2486.

[8] J. D. Joannopoulos et al. *Photonic Crystals: Molding the Flow of Light*. 2nd ed. Princeton University Press, 2008.

[9] S. Yoshioka and S. Kinoshita. "Effect of Macroscopic Structure in Iridescent Color of the Peacock Feathers". In: *Forma* 17 (2002), pp. 169–181.

[10] E. Gaillou et al. "Common gem opal: An investigation of micro- to nanostructure". In: *Am. Mineral.* 93.11-12 (2008), pp. 1865–1873. DOI: doi:10.2138/am.2008.2518.

[11] M. Notomi. "Manipulating light with strongly modulated photonic crystals". In: *Rep. Prog. Phys.* 73.9 (2010), p. 096501. DOI: 10.1088/0034-4885/73/9/096501.

[12] D. N. Chigrin et al. "Observation of total omnidirectional reflection from a one-dimensional dielectric lattice". In: *Appl. Phys. A* 68.1 (1999), pp. 25–28. DOI: 10.1007/s003390050849.

[13] J. M. Bendickson, J. P. Dowling, and M. Scalora. "Analytic expressions for the electromagnetic mode density in finite, one-dimensional, photonic band-gap structures". In: *Phys. Rev. E* 53 (4), pp. 4107–4121. DOI: 10.1103/PhysRevE.53.4107.

[14] M. Scalora et al. "Pulsed second-harmonic generation in nonlinear, one-dimensional, periodic structures". In: *Phys. Rev. A* 56 (4 1997), pp. 3166–3174. DOI: 10.1103/PhysRevA.56.3166.

[15] D. Aurelio and M. Liscidini. "Electromagnetic field enhancement in Bloch surface waves". In: *Phys. Rev. B* 96 (4 July 2017), p. 045308. DOI: 10.1103/PhysRevB.96.045308.

[16] R. Dubey et al. "Experimental investigation of the propagation properties of Bloch surface waves on dielectric multilayer platform". In: *J. Eur. Opt. Soc.-Rapid* 13.1 (2017), p. 5. DOI: 10.1186/s41476-016-0029-1.

[17] J. A. Jr. Polo and A. Lakhtakia. "Surface electromagnetic waves: a review". In: *Laser Photonics Rev.* 5.2 (2011), pp. 234–246. DOI: https://doi.org/10.1002/lpor.200900050.

[18] V. J. Sorger et al. "Toward integrated plasmonic circuits". In: *MRS Bull.* 37.8 (2012), pp. 728–738. DOI: 10.1557/mrs.2012.170.

[19] A. Sinibaldi et al. "Direct comparison of the performance of Bloch surface wave and surface plasmon polariton sensors". In: *Sensor Actuat. B* 174 (2012), pp. 292–298. DOI: https://doi.org/10.1016/j.snb.2012.07.015.

[20] P. Yeh, A. Yariv, and C.-S. Hong. "Electromagnetic propagation in periodic stratified media. I. General theory∗". In: *J. Opt. Soc. Am.* 67.4 (1977), pp. 423–438. DOI: 10.1364/JOSA.67.000423.

[21] P. Yeh, A. Yariv, and A. Y. Cho. "Optical surface waves in periodic layered media". In: *Appl. Phys. Lett.* 32.2 (1978), pp. 104–105. DOI: 10.1063/1.89953.

[22] R. D. Meade et al. "Electromagnetic Bloch waves at the surface of a photonic crystal". In: *Phys. Rev. B* 44 (19 1991), pp. 10961–10964. DOI: 10.1103/PhysRevB.44.10961.

[23] W. M. Robertson et al. "Observation of surface photons on periodic dielectric arrays". In: *Opt. Lett.* 18.7 (1993), pp. 528–530. DOI: 10.1364/OL.18.000528.

[24] W. M. Robertson and M. S. May. "Surface electromagnetic wave excitation on one-dimensional photonic band-gap arrays". In: *Appl. Phys. Lett.* 74.13 (1999), pp. 1800–1802. DOI: 10.1063/1.123090.

[25] W. M. Robertson. "Experimental measurement of the effect of termination on surface electromagnetic waves in one-dimensional photonic bandgap arrays". In: *J. Light. Technol.* 17.11 (1999), pp. 2013–2017. DOI: 10.1109/50.802988.

[26] F. Giorgis et al. “Experimental determination of the sensitivity of Bloch Surface Waves based sensors”. In: *Opt. Express* 18.8 (2010), pp. 8087–8093. DOI: 10.1364/OE.18.008087.

[27] F. Michelotti et al. “Fast optical vapour sensing by Bloch surface waves on porous silicon membranes”. In: *Phys. Chem. Chem. Phys.* 12 (2 2010), pp. 502–506. DOI: 10.1039/B914280K.

[28] M. Ballarini et al. “Bloch surface waves-controlled emission of organic dyes grafted on a one-dimensional photonic crystal”. In: *Appl. Phys. Lett.* 99.4 (2011), p. 043302. DOI: 10.1063/1.3616144.

[29] K. Toma et al. “Bloch surface wave-enhanced fluorescence biosensor”. In: *Biosens. Bioelectron.* 43 (2013), pp. 108–114. DOI: https://doi.org/10.1016/j.bios.2012.12.001.

[30] V. Paeder et al. “Detection of protein aggregation with a Bloch surface wave based sensor”. In: *Sensor Actuat. B* 157.1 (2011), pp. 260–264. DOI: https://doi.org/10.1016/j.snb.2011.03.060.

[31] A. Farmer et al. “Biosensing using surface electromagnetic waves in photonic band gap multilayers”. In: *Sensor Actuat. B* 173 (2012), pp. 79–84. DOI: https://doi.org/10.1016/j.snb.2012.06.015.

[32] P. Rivolo et al. “Real time secondary antibody detection by means of silicon-based multilayers sustaining Bloch surface waves”. In: *Sensor Actuat. B* 161.1 (2012), pp. 1046–1052. DOI: https://doi.org/10.1016/j.snb.2011.12.006.

[33] G. A. Rodriguez et al. “A size selective porous silicon grating-coupled Bloch surface and sub-surface wave biosensor”. In: *Biosens. Bioelectron.* 53 (2014), pp. 486–493. DOI: https://doi.org/10.1016/j.bios.2013.10.028.

[34] A. Sinibaldi et al. “A full ellipsometric approach to optical sensing with Bloch surface waves on photonic crystals”. In: *Opt. Express* 21.20 (2013), pp. 23331–23344. DOI: 10.1364/OE.21.023331.

[35] Y. Li et al. “Phase-sensitive Bloch surface wave sensor based on variable angle spectroscopic ellipsometry”. In: *Opt. Express* 22.18 (2014), pp. 21403–21410. DOI: 10.1364/OE.22.021403.

[36] W. Kong et al. “High-sensitivity sensing based on intensity-interrogated Bloch surface wave sensors”. In: *Sensor Actuat. B* 193 (2014), pp. 467–471. DOI: https://doi.org/10.1016/j.snb.2013.11.101.

[37] A. Sinibaldi et al. “Combining label-free and fluorescence operation of Bloch surface wave optical sensors”. In: *Opt. Lett.* 39.10 (2014), pp. 2947–2950. DOI: 10.1364/OL.39.002947.

[38] A. Sinibaldi et al. “Bloch Surface Waves Biosensors for High Sensitivity Detection of Soluble ERBB2 in a Complex Biological Environment”. In: *Biosensors* 7.3 (2017). DOI: 10.3390/bios7030033.

[39] M. Liscidini and J. E. Sipe. "Enhancement of diffraction for biosensing applications via Bloch surface waves". In: *Appl. Phys. Lett.* 91.25 (2007), p. 253125. DOI: 10.1063/1.2826545.

[40] M. Liscidini and J. E. Sipe. "Analysis of Bloch-surface-wave assisted diffraction-based biosensors". In: *J. Opt. Soc. Am. B* 26.2 (2009), pp. 279–289. DOI: 10.1364/JOSAB.26.000279.

[41] M. Liscidini et al. "Demonstration of diffraction enhancement via Bloch surface waves in a-SiN:H multilayers". In: *Appl. Phys. Lett.* 94.4 (2009), p. 043117. DOI: 10.1063/1.3076101.

[42] A. Delfan, M. Liscidini, and J E. Sipe. "Surface enhanced Raman scattering in the presence of multilayer dielectric structures". In: *J. Opt. Soc. Am. B* 29.8 (2012), pp. 1863–1874. DOI: 10.1364/JOSAB.29.001863.

[43] S. Pirotta et al. "Surface-Enhanced Raman Scattering in Purely Dielectric Structures via Bloch Surface Waves". In: *J. Phys. Chem. C* 117.13 (2013), pp. 6821–6825. DOI: 10.1021/jp400223f.

[44] E. Descrovi et al. "Guided Bloch Surface Waves on Ultrathin Polymeric Ridges". In: *Nano Lett.* 10.6 (2010), pp. 2087–2091. DOI: 10.1021/nl100481q.

[45] X. Wu et al. "Phase-sensitive near field Investigation of Bloch surface wave propagation in curved waveguides". In: *J. Eur. Opt. Soc.-Rapid* 9 (2014).

[46] L. Yu et al. "Manipulating Bloch surface waves in 2D: a platform concept-based flat lens". In: *Light Sci. Appl.* 3.1 (2014), e124–e124. DOI: 10.1038/lsa.2014.5.

[47] A. Angelini et al. "In-plane 2D focusing of surface waves by ultrathin refractive structures". In: *Opt. Lett.* 39.22 (2014), pp. 6391–6394. DOI: 10.1364/OL.39.006391.

[48] R. Dubey et al. "Near-field characterization of a Bloch-surface-wave-based 2D disk resonator". In: *Opt. Lett.* 41.21 (2016), pp. 4867–4870. DOI: 10.1364/OL.41.004867.

[49] G. A. Rodriguez et al. "Bloch surface wave ring resonator based on porous silicon". In: *Appl. Phys. Lett.* 115.1 (2019), p. 011101. DOI: 10.1063/1.5093435.

[50] T. Kovalevich et al. "Polarization controlled directional propagation of Bloch surface wave". In: *Opt. Express* 25.5 (2017), pp. 5710–5715. DOI: 10.1364/OE.25.005710.

[51] K. R. Safronov et al. "Multimode Interference of Bloch Surface Electromagnetic Waves". In: *ACS Nano* 14.8 (2020), pp. 10428–10437. DOI: 10.1021/acsnano.0c04301.

[52] K. A. Abrashitova et al. "Bloch Surface Wave Photonic Device Fabricated by Femtosecond Laser Polymerisation Technique". In: *Appl. Sci.* 8.1 (2018). DOI: 10.3390/app8010063.

[53] S. Y. Siew et al. “Review of Silicon Photonics Technology and Platform Development”. In: *J. Light. Technol.* 39.13 (2021), pp. 4374–4389. DOI: 10.1109/JLT.2021.3066203.

[54] T. Sharma et al. “Review of Recent Progress on Silicon Nitride-Based Photonic Integrated Circuits”. In: *IEEE Access* 8 (2020), pp. 195436–195446. DOI: 10.1109/ACCESS.2020.3032186.

[55] Y. Qi and Y. Li. “Integrated lithium niobate photonics”. In: *Nanophotonics* 9.6 (2020), pp. 1287–1320. DOI: doi:10.1515/nanoph-2020-0013.

[56] M. Smit, K. Williams, and J. van der Tol. “Past, present, and future of InP-based photonic integration”. In: *APL Photonics* 4.5 (2019), p. 050901. DOI: 10.1063/1.5087862.

[57] Mounier E. and Malinge J.-L. *Silicon Photonics and Photonic Integrated Circuits 2019: Market and Technology Report*. Tech. rep. Yole Développement, 2019.

[58] C. Doerr. “Silicon photonic integration in telecommunications”. In: *Front. Phys.* 3 (2015). DOI: 10.3389/fphy.2015.00037.

[59] Q. Wilmart et al. “A Complete Si Photonics Platform Embedding Ultra-Low Loss Waveguides for O- and C-Band”. In: *J. Light. Technol.* 39.2 (2021), pp. 532–538. DOI: 10.1109/JLT.2020.3030123.

[60] J. Wang et al. “Gallium arsenide (GaAs) quantum photonic waveguide circuits”. In: *Opt. Commun.* 327 (2014). Special Issue on Nonlinear Quantum Photonics, pp. 49–55. DOI: https://doi.org/10.1016/j.optcom.2014.02.040.

[61] Y. Sugimoto et al. “Low propagation loss of 0.76 dB/mm in GaAs-based single-line-defect two-dimensional photonic crystal slab waveguides up to 1 cm in length”. In: *Opt. Express* 12.6 (2004), pp. 1090–1096. DOI: 10.1364/OPEX.12.001090.

[62] D. D’Agostino et al. “Low-loss passive waveguides in a generic InP foundry process via local diffusion of zinc”. In: *Opt. Express* 23.19 (2015), pp. 25143–25157. DOI: 10.1364/OE.23.025143.

[63] J. Guan et al. “Hybrid laser written waveguides in fused silica for low loss and polarization independence”. In: *Opt. Express* 25.5 (2017), pp. 4845–4859. DOI: 10.1364/OE.25.004845.

[64] D. Duchesne et al. “Efficient self-phase modulation in low loss, high index doped silica glass integrated waveguides”. In: *Opt. Express* 17.3 (2009), pp. 1865–1870. DOI: 10.1364/OE.17.001865.

[65] M. Zhang et al. “Monolithic ultra-high-Q lithium niobate microring resonator”. In: *Optica* 4.12 (2017), pp. 1536–1537. DOI: 10.1364/OPTICA.4.001536.

[66] B. Desiatov et al. “Ultra-low-loss integrated visible photonics using thin-film lithium niobate”. In: *Optica* 6.3 (2019), pp. 380–384. DOI: 10.1364/OPTICA.6.000380.

[67] A. Z. Subramanian et al. “Low-Loss Singlemode PECVD Silicon Nitride Photonic Wire Waveguides for 532–900 nm Wavelength Window Fabricated Within a CMOS Pilot Line”. In: *IEEE Photonics J.* 5.6 (2013), pp. 2202809–2202809. DOI: 10.1109/JPHOT.2013.2292698.

[68] J. F. Bauters et al. “Ultra-low-loss high-aspect-ratio Si3N4 waveguides”. In: *Opt. Express* 19.4 (2011), pp. 3163–3174. DOI: 10.1364/OE.19.003163.

[69] W. M. Pätzold, A. Demircan, and U. Morgner. “Low-loss curved waveguides in polymers written with a femtosecond laser”. In: *Opt. Express* 25.1 (2017), pp. 263–270. DOI: 10.1364/OE.25.000263.

[70] H. Ma, A. K.-Y. Jen, and L. R. Dalton. “Polymer-Based Optical Waveguides: Materials, Processing, and Devices”. In: *Adv. Mater.* 14.19 (2002), pp. 1339–1365. DOI: https://doi.org/10.1002/1521-4095(20021002)14:19<1339::AID-ADMA1339>3.0.CO;2-O.

[71] T. Nikolajsen et al. “Polymer-based surface-plasmon-polariton stripe waveguides at telecommunication wavelengths”. In: *Appl. Phys. Lett.* 82.5 (2003), pp. 668–670. DOI: 10.1063/1.1542944.

[72] M.-J. Li and T. Hayashi. “Advances in low-loss, large-area, and multicore fibers”. In: *Optical Fiber Telecommunications VII*. Academic Press, 2020, pp. 3–50. DOI: https://doi.org/10.1016/B978-0-12-816502-7.00001-4.

[73] I. D. Rukhlenko, M. Premaratne, and G. P. Agrawal. “Effective mode area and its optimization in silicon-nanocrystal waveguides”. In: *Opt. Lett.* 37.12 (2012), pp. 2295–2297. DOI: 10.1364/OL.37.002295.

[74] K. J. Vahala. “Optical microcavities”. In: *Nature* 424.6950 (2003), pp. 839–846. DOI: 10.1038/nature01939.

[75] C. Ciminelli et al. “High performance InP ring resonator for new generation monolithically integrated optical gyroscopes”. In: *Opt. Express* 21.1 (2013), pp. 556–564. DOI: 10.1364/OE.21.000556.

[76] A. Biberman et al. “Ultralow-loss silicon ring resonators”. In: *Opt. Lett.* 37.20 (2012), pp. 4236–4238. DOI: 10.1364/OL.37.004236.

[77] L. Zhang et al. “Ultrahigh-Q silicon racetrack resonators”. In: *Photon. Res.* 8.5 (2020), pp. 684–689. DOI: 10.1364/PRJ.387816.

[78] Y.-X. Yin et al. “High-Q-Factor Silica-Based Racetrack Microring Resonators”. In: *Photonics* 8.2 (2021). DOI: 10.3390/photonics8020043.

[79] X. Ji et al. “Ultra-low-loss on-chip resonators with sub-milliwatt parametric oscillation threshold”. In: *Optica* 4.6 (2017), pp. 619–624. DOI: 10.1364/OPTICA.4.000619.

[80] M. W. Puckett et al. “422 Million intrinsic quality factor planar integrated all-waveguide resonator with sub-MHz linewidth”. In: *Nat. Commun.* 12.1 (2021), p. 934. DOI: 10.1038/s41467-021-21205-4.

[81] X. Tu et al. “Ultrahigh Q Polymer Microring Resonators for Biosensing Applications”. In: *IEEE Photonics J.* 11.2 (2019), pp. 1–10. DOI: 10.1109/JPHOT.2019.2899666.

[82] C. Horvath et al. “Polymer Hybrid Plasmonic Waveguides and Microring Resonators”. In: *IEEE Photon. Technol. Lett.* 23.17 (2011), pp. 1267–1269. DOI: 10.1109/LPT.2011.2159784.

[83] W. Bogaerts et al. “Silicon microring resonators”. In: *Laser Photonics Rev.* 6.1 (2012), pp. 47–73. DOI: https://doi.org/10.1002/lpor.201100017.

[84] W. Bogaerts et al. “Silicon-on-Insulator Spectral Filters Fabricated With CMOS Technology”. In: *IEEE J. Sel. Top. Quantum Electron.* 16 (2010), pp. 33–44.

[85] Q. Xu et al. “Micrometre-scale silicon electro-optic modulator”. In: *Nature* 435.7040 (2005), pp. 325–327. DOI: 10.1038/nature03569.

[86] K. De Vos et al. “Silicon-on-Insulator microring resonator for sensitive and label-free biosensing”. In: *Opt. Express* 15.12 (2007), pp. 7610–7615. DOI: 10.1364/OE.15.007610.

[87] M. Ferrera et al. “Low power four wave mixing in an integrated, micro-ring resonator with Q = 1.2 million”. In: *Opt. Express* 17.16 (2009), pp. 14098–14103. DOI: 10.1364/OE.17.014098.

[88] D. Grassani et al. “Micrometer-scale integrated silicon source of time-energy entangled photons”. In: *Optica* 2.2 (Feb. 2015), pp. 88–94. DOI: 10.1364/OPTICA.2.000088.

[89] M. Minkov and V. Savona. “Automated optimization of photonic crystal slab cavities”. In: *Sci. Rep.* 4.1 (2014), p. 5124. DOI: 10.1038/srep05124.

[90] Y. Lai et al. “Genetically designed L3 photonic crystal nanocavities with measured quality factor exceeding one million”. In: *Appl. Phys. Lett.* 104.24 (2014), p. 241101. DOI: 10.1063/1.4882860.

[91] S. Song B.-S.and Noda, T. Asano, and Y. Akahane. “Ultra-high-Q photonic double-heterostructure nanocavity”. In: *Nat. Mater.* 4.3 (2005), pp. 207–210. DOI: 10.1038/nmat1320.

[92] E. Kuramochi et al. “Ultrahigh-Q photonic crystal nanocavities realized by the local width modulation of a line defect”. In: *Appl. Phys. Lett.* 88.4 (2006), p. 041112. DOI: 10.1063/1.2167801.

[93] H. Sekoguchi et al. “Photonic crystal nanocavity with a Q-factor of 9 million”. In: *Opt. Express* 22.1 (2014), pp. 916–924. DOI: 10.1364/OE.22.000916.

[94] P. Velha et al. “Ultra-High Q/V Fabry-Perot microcavity on SOI substrate”. In: *Opt. Express* 15.24 (2007), pp. 16090–16096. DOI: 10.1364/OE.15.016090.

[95] E. Kuramochi et al. "Ultrahigh-Q one-dimensional photonic crystal nanocavities with modulated mode-gap barriers on SiO2 claddings and on air claddings". In: *Opt. Express* 18.15 (2010), pp. 15859–15869. DOI: 10.1364/OE.18.015859.

[96] S. Hu et al. "Experimental realization of deep-subwavelength confinement in dielectric optical resonators". In: *Sci. Adv.* 4.8 (2018), eaat2355. DOI: 10.1126/sciadv.aat2355.

[97] K. Yao and Y. Shi. "High-Q width modulated photonic crystal stack mode-gap cavity and its application to refractive index sensing". In: *Opt. Express* 20.24 (2012), pp. 27039–27044. DOI: 10.1364/OE.20.027039.

[98] Judson D. Ryckman and S. M. Weiss. "Low mode volume slotted photonic crystal single nanobeam cavity". In: *Appl. Phys. Lett.* 101.7 (2012), p. 071104. DOI: 10.1063/1.4742749.

[99] P. Xu et al. "Slotted photonic crystal nanobeam cavity with parabolic modulated width stack for refractive index sensing". In: *Opt. Express* 21.22 (2013), pp. 26908–26913. DOI: 10.1364/OE.21.026908.

[100] Y. Gong and J. Vučković. "Photonic crystal cavities in silicon dioxide". In: *Appl. Phys. Lett.* 96.3 (2010), p. 031107. DOI: 10.1063/1.3297877.

[101] Q. Quan et al. "High-Q, low index-contrast polymeric photonic crystal nanobeam cavities". In: *Opt. Express* 19.22 (2011), pp. 22191–22197. DOI: 10.1364/OE.19.022191.

[102] G. Crosnier et al. "High Q factor InP photonic crystal nanobeam cavities on silicon wire waveguides". In: *Opt. Lett.* 41.3 (2016), pp. 579–582. DOI: 10.1364/OL.41.000579.

[103] G. A. Rodriguez et al. "Photonic crystal nanobeam biosensors based on porous silicon". In: *Opt. Express* 27.7 (2019), pp. 9536–9549. DOI: 10.1364/OE.27.009536.

[104] M. Khan et al. "Fabrication and characterization of high-quality-factor silicon nitride nanobeam cavities". In: *Opt. Lett.* 36.3 (2011), pp. 421–423. DOI: 10.1364/OL.36.000421.

[105] J. Zhan et al. "High-Q nanobeam cavities on a silicon nitride platform enabled by slow light". In: *APL Photonics* 5.6 (2020), p. 066101. DOI: 10.1063/5.0007279.

[106] J. S. Foresi et al. "Photonic-bandgap microcavities in optical waveguides". In: *Nature* 390.6656 (1997), pp. 143–145. DOI: 10.1038/36514.

[107] Y. Akahane et al. "High-Q photonic nanocavity in a two-dimensional photonic crystal". In: *Nature* 425.6961 (2003), pp. 944–947. DOI: 10.1038/nature02063.

[108] P. Lalanne and J. P. Hugonin. "Bloch-wave engineering for high-Q, small-V microcavities". In: *IEEE J. Quantum Electron.* 39.11 (2003), pp. 1430–1438. DOI: 10.1109/JQE.2003.818283.

[109] J. T. Robinson et al. "Ultrasmall Mode Volumes in Dielectric Optical Microcavities". In: *Phys. Rev. Lett.* 95 (14 2005), p. 143901. DOI: 10.1103/PhysRevLett.95.143901.

[110] S. Hu and S. M. Weiss. "Design of Photonic Crystal Cavities for Extreme Light Concentration". In: *ACS Photonics* 3.9 (2016), pp. 1647–1653. DOI: 10.1021/acsphotonics.6b00219.

[111] P. B. Deotare et al. "Photonic Crystal Nanobeam Cavities for Tunable Filter and Router Applications". In: *IEEE J. Sel. Top. Quantum Electron.* 19 (2013), pp. 3600210–3600210.

[112] E. Li et al. "Ultracompact Silicon-Conductive Oxide Nanocavity Modulator with 0.02 Lambda-Cubic Active Volume". In: *Nano Lett.* 18.2 (2018), pp. 1075–1081. DOI: 10.1021/acs.nanolett.7b04588.

[113] L.-D. Haret et al. "Extremely low power optical bistability in silicon demonstrated using 1D photonic crystal nanocavity". In: *Opt. Express* 17.23 (2009), pp. 21108–21117. DOI: 10.1364/OE.17.021108.

[114] Y. Zhang et al. "Photonic crystal nanobeam lasers". In: *Appl. Phys. Lett.* 97.5 (2010), p. 051104. DOI: 10.1063/1.3475397.

[115] B.-H. Ahn et al. "One-dimensional parabolic-beam photonic crystal laser". In: *Opt. Express* 18.6 (2010), pp. 5654–5660. DOI: 10.1364/OE.18.005654.

[116] D. Yang et al. "Design of simultaneous high-Q and high-sensitivity photonic crystal refractive index sensors". In: *J. Opt. Soc. Am. B* 30.8 (2013), pp. 2027–2031. DOI: 10.1364/JOSAB.30.002027.

[117] D. Yang et al. "High sensitivity and high Q-factor nanoslotted parallel quadrabeam photonic crystal cavity for real-time and label-free sensing". In: *Appl. Phys. Lett.* 105.6 (2014), p. 063118. DOI: 10.1063/1.4867254.

[118] M. W. McCutcheon and M. Lončar. "Design of a silicon nitride photonic crystal nanocavity with a Quality factor of one million for coupling to a diamond nanocrystal". In: *Opt. Express* 16.23 (2008), pp. 19136–19145. DOI: 10.1364/OE.16.019136.

[119] V. R. Almeida, R. R. Panepucci, and M. Lipson. "Nanotaper for compact mode conversion". In: *Opt. Lett.* 28.15 (2003), pp. 1302–1304. DOI: 10.1364/OL.28.001302.

[120] T. Shoji et al. "Low loss mode size converter from 0.3 µsquare Si wire waveguides to singlemode fibres". In: *Electronics Letters* 38 (2002), pp. 1669–1670. DOI: 10.1049/el:20021185.

[121] B. Ben Bakir et al. "Low-Loss ($<$ 1 dB) and Polarization-Insensitive Edge Fiber Couplers Fabricated on 200-mm Silicon-on-Insulator Wafers". In: *IEEE Photon. Technol. Lett.* 22.11 (2010), pp. 739–741. DOI: 10.1109/LPT.2010.2044992.

[122] T. Yoshida et al. “Vertically Curved Si Waveguide Coupler with Low Loss and Flat Wavelength Window”. In: *J. Light. Technol.* 34.7 (2016), pp. 1567–1571. DOI: 10.1109/JLT.2015.2506732.

[123] H. Gehring et al. “Low-loss fiber-to-chip couplers with ultrawide optical bandwidth”. In: *APL Photonics* 4.1 (2019), p. 010801. DOI: 10.1063/1.5064401.

[124] F. Van Laere et al. “Compact Focusing Grating Couplers for Silicon-on-Insulator Integrated Circuits”. In: *IEEE Photon. Technol. Lett.* 19.23 (2007), pp. 1919–1921. DOI: 10.1109/LPT.2007.908762.

[125] D. Vermeulen et al. “High-efficiency fiber-to-chip grating couplers realized using an advanced CMOS-compatible Silicon-On-Insulator platform”. In: *Opt. Express* 18.17 (2010), pp. 18278–18283. DOI: 10.1364/OE.18.018278.

[126] Y. Ding et al. “Fully etched apodized grating coupler on the SOI platform with –0.58 dB coupling efficiency”. In: *Opt. Lett.* 39.18 (2014), pp. 5348–5350. DOI: 10.1364/OL.39.005348.

[127] S. Romero-Garcia et al. “Visible wavelength silicon nitride focusing grating coupler with AlCu/TiN reflector”. In: *Opt. Lett.* 38.14 (2013), pp. 2521–2523. DOI: 10.1364/OL.38.002521.

[128] S. K. Selvaraja et al. “Highly efficient grating coupler between optical fiber and silicon photonic circuit”. In: *CLEO/IQEC*. OSA, 2009, CTuC6. DOI: 10.1364/CLEO.2009.CTuC6.

[129] W. D. Sacher et al. “Wide bandwidth and high coupling efficiency Si3N4-on-SOI dual-level grating coupler”. In: *Opt. Express* 22.9 (2014), pp. 10938–10947. DOI: 10.1364/OE.22.010938.

[130] R. Marchetti et al. “High-efficiency grating-couplers: demonstration of a new design strategy”. In: *Sci. Rep.* 7.1 (2017), p. 16670. DOI: 10.1038/s41598-017-16505-z.

[131] E. Lomonte, F. Lenzini, and W. H. P. Pernice. “Efficient self-imaging grating couplers on a lithium-niobate-on-insulator platform at near-visible and telecom wavelengths”. In: *Opt. Express* 29.13 (2021), pp. 20205–20216. DOI: 10.1364/OE.428138.

[132] M. Ayata et al. “Compact, ultra-broadband plasmonic grating couplers”. In: *Opt. Express* 27.21 (2019), pp. 29719–29729. DOI: 10.1364/OE.27.029719.

[133] Riccardo Marchetti et al. “Coupling strategies for silicon photonics integrated chips (Invited)”. In: *Photon. Res.* 7.2 (2019), pp. 201–239. DOI: 10.1364/PRJ.7.000201.

[134] M. Liscidini. “Surface guided modes in photonic crystal ridges: the good, the bad, and the ugly”. In: *J. Opt. Soc. Am. B* 29.8 (2012), pp. 2103–2109. DOI: 10.1364/JOSAB.29.002103.

[135] N. Pala and M. Karabiyik. "Electron Beam Lithography (EBL)". In: *Encyclopedia of Nanotechnology*. Ed. by B. Bhushan. Springer Netherlands, 2016, pp. 1033–1057. DOI: 10.1007/978-94-017-9780-1_344.

[136] R. Agrawal and C. Wang. "Laser Beam Machining". In: *Encyclopedia of Nanotechnology*. Ed. by B. Bhushan. Springer Netherlands, 2016, pp. 1739–1753. DOI: 10.1007/978-94-017-9780-1_101020.

[137] D. Shan et al. "Polymeric biomaterials for biophotonic applications". In: *Bioact. Mater.* 3.4 (2018), pp. 434–445. DOI: https://doi.org/10.1016/j.bioactmat.2018.07.001.

[138] S. P. Davtyan et al. "Polymer/QDs Nanocomposites for Waveguiding Applications". In: *J. Nanomater.* (2012), p. 960201. DOI: 10.1155/2012/960201.

[139] A. W. Schell et al. "Three-dimensional quantum photonic elements based on single nitrogen vacancy-centres in laser-written microstructures". In: *Sci. Rep.* 3.1 (2013), p. 1577. DOI: 10.1038/srep01577.

[140] Q. Shi et al. "Wiring up pre-characterized single-photon emitters by laser lithography". In: *Sci. Rep.* 6.1 (2016), p. 31135. DOI: 10.1038/srep31135.

[141] A. Landowski et al. "Coherent remote control of quantum emitters embedded in polymer waveguides". In: *APL Photonics* 5.1 (2020), p. 016101. DOI: 10.1063/1.5124618.

[142] M. Colautti et al. "A 3D Polymeric Platform for Photonic Quantum Technologies". In: *Adv. Quantum Technol.* 3.7 (2020), p. 2000004. DOI: https://doi.org/10.1002/qute.202000004.

[143] P.N. Prasad. "Polymers for photonics". In: *J. Nonlinear Opt. Phys. Mater.* 03.04 (1994), pp. 531–541. DOI: 10.1142/S0218199194000316.

[144] R. Dubey et al. "Ultra-thin Bloch-surface-wave-based reflector at telecommunication wavelength". In: *Photon. Res.* 5.5 (2017), pp. 494–499. DOI: 10.1364/PRJ.5.000494.

[145] R. Wang et al. "Bloch surface waves confined in one dimension with a single polymeric nanofibre". In: *Nat. Commun.* 8.1 (2017), p. 14330. DOI: 10.1038/ncomms14330.

[146] T. Sfez et al. "Bloch surface waves in ultrathin waveguides: near-field investigation of mode polarization and propagation". In: *J. Opt. Soc. Am. B* 27.8 (2010), pp. 1617–1625. DOI: 10.1364/JOSAB.27.001617.

[147] B. Vosoughi Lahijani et al. "Centimeter-Scale Propagation of Optical Surface Waves at Visible Wavelengths". In: *Adv. Opt. Mater.* (2022), p. 2102854. DOI: https://doi.org/10.1002/adom.202102854.

[148] M. Menotti and M. Liscidini. "Optical resonators based on Bloch surface waves". In: *J. Opt. Soc. Am. B* 32.3 (2015), pp. 431–438. DOI: 10.1364/JOSAB.32.000431.

[149] C. L. Xu et al. "Full-vectorial mode calculations by finite difference method". In: *IEE Proceedings. Optoelectronics* 141 (5 1994), pp. 281–286. DOI: 10.1049/ip-opt:19941419.

[150] J. B. Driscoll et al. "Large longitudinal electric fields (Ez) in silicon nanowire waveguides". In: *Opt. Express* 17.4 (2009), pp. 2797–2804. DOI: 10.1364/OE.17.002797.

[151] B. Vosoughi Lahijani et al. "Bloch Surface Waves Fabry- Pérot Nanocavity". In: *J. Phys. Conf. Ser.* 1092 (2018), p. 012163. DOI: 10.1088/1742-6596/1092/1/012163.

[152] U. Stella et al. "Enhanced Directional Light Emission Assisted by Resonant Bloch Surface Waves in Circular Cavities". In: *ACS Photonics* 6.8 (2019), pp. 2073–2082. DOI: 10.1021/acsphotonics.9b00570.

[153] K. Srinivasan and O. Painter. "Momentum space design of high-Q photonic crystal optical cavities". In: *Opt. Express* 10.15 (2002), pp. 670–684. DOI: 10.1364/OE.10.000670.

[154] D. Englund, I. Fushman, and J. Vučković. "General recipe for designing photonic crystal cavities". In: *Opt. Express* 13.16 (2005), pp. 5961–5975. DOI: 10.1364/OPEX.13.005961.

[155] Q. Quan and M. Lončar. "Deterministic design of wavelength scale, ultra-high Q photonic crystal nanobeam cavities". In: *Opt. Express* 19.19 (2011), pp. 18529–18542. DOI: 10.1364/OE.19.018529.

[156] K. R. Safronov et al. "Miniature Otto Prism Coupler for Integrated Photonics". In: *Laser Photonics Rev.* (2022), p. 2100542. DOI: https://doi.org/10.1002/lpor.202100542.

[157] X.-B. Kang et al. "Guided Bloch surface wave resonance for biosensor designs". In: *J. Opt. Soc. Am. A* 33.5 (2016), pp. 997–1003. DOI: 10.1364/JOSAA.33.000997.

[158] M. Scaravilli et al. "Grating-coupling-based excitation of Bloch surface waves for lab-on-fiber optrodes". In: *Opt. Express* 24.24 (2016), pp. 27771–27784. DOI: 10.1364/OE.24.027771.

[159] M. Scaravilli et al. "Excitation of Bloch Surface Waves on an Optical Fiber Tip". In: *Adv. Opt. Mater.* 6.19 (2018), p. 1800477. DOI: https://doi.org/10.1002/adom.201800477.

[160] L. Cheng et al. "Grating Couplers on Silicon Photonics: Design Principles, Emerging Trends and Practical Issues". In: *Micromachines* 11.7 (2020). DOI: 10.3390/mi11070666.

[161] D. Taillaert, P. Bienstman, and R. Baets. "Compact efficient broadband grating coupler for silicon-on-insulator waveguides". In: *Opt. Lett.* 29.23 (2004), pp. 2749–2751. DOI: 10.1364/OL.29.002749.

[162] J. Jiang, M. Chen, and J.A. Fan. "Deep neural networks for the evaluation and design of photonic devices". In: *Nat. Rev. Mater.* (2020). DOI: 10.1038/s41578-020-00260-1.

[163] S. Molesky et al. "Inverse design in nanophotonics". In: *Nat. Photonics* 12.11 (2018), pp. 659–670. DOI: 10.1038/s41566-018-0246-9.

[164] W. Ma et al. "Deep learning for the design of photonic structures". In: *Nat. Photonics* 15.2 (2021), pp. 77–90. DOI: 10.1038/s41566-020-0685-y.

[165] J. S. Jensen and O. Sigmund. "Topology optimization for nano-photonics". In: *Laser Photonics Rev.* 5.2 (2011), pp. 308–321. DOI: https://doi.org/10.1002/lpor.201000014.

[166] C. M. Lalau-Keraly et al. "Adjoint shape optimization applied to electromagnetic design". In: *Opt. Express* 21.18 (2013), pp. 21693–21701. DOI: 10.1364/OE.21.021693.

[167] L. Sanchis et al. "Integrated optical devices design by genetic algorithm". In: *Appl. Phys. Lett.* 84.22 (2004), pp. 4460–4462. DOI: 10.1063/1.1738931.

[168] Y. Zhang et al. "A compact and low loss Y-junction for submicron silicon waveguide". In: *Opt. Express* 21.1 (2013), pp. 1310–1316. DOI: 10.1364/OE.21.001310.

[169] J. Lu and J. Vučković. "Nanophotonic computational design". In: *Opt. Express* 21.11 (2013), pp. 13351–13367. DOI: 10.1364/OE.21.013351.

[170] A. Y. Piggott et al. "Inverse design and demonstration of a compact and broadband on-chip wavelength demultiplexer". In: *Nat. Photonics* 9.6 (2015), pp. 374–377. DOI: 10.1038/nphoton.2015.69.

[171] M. Minkov et al. "Inverse Design of Photonic Crystals through Automatic Differentiation". In: *ACS Photonics* 7.7 (2020), pp. 1729–1741. DOI: 10.1021/acsphotonics.0c00327.

[172] Z. Liu et al. "Generative Model for the Inverse Design of Metasurfaces". In: *Nano Lett.* 18.10 (2018), pp. 6570–6576. DOI: 10.1021/acs.nanolett.8b03171.

[173] R. L. Haupt and D. H. Werner. "Anatomy of a Genetic Algorithm". In: *Genetic Algorithms in Electromagnetics*. John Wiley & Sons, 2007. Chap. 2, pp. 29–43. DOI: https://doi.org/10.1002/9780470106280.ch2.

[174] U. S. Inan and R. A. Marshall. *Numerical Electromagnetics: The FDTD Method*. Cambridge University Press, 2011. DOI: 10.1017/CBO9780511921353.

[175] K. Yee. "Numerical solution of initial boundary value problems involving Maxwell's equations in isotropic media". In: *IEEE Trans. Antennas Propag.* 14.3 (1966), pp. 302–307. DOI: 10.1109/TAP.1966.1138693.

[176] A. Taflove and S.C. Hagness. *Computational Electrodynamics: The Finite-Difference Time-Domain Method*. Artech House, 2005.